4-1-2010

Locomotion of circular robots with diametrically translating legs: Design, analysis, and fabrication

Eric R. Steffan

Recommended Citation

Steffan, Eric R., "Locomotion of circular robots with diametrically translating legs: Design, analysis, and fabrication" (2010). Thesis. Rochester Institute of Technology. Accessed from

Locomotion of Circular Robots with Diametrically Translating Legs: Design, Analysis, and Fabrication

by

Eric R. Steffan

A Thesis Submitted in Partial Fulfillment of the Requirements for the Degree of
Master of Science in Mechanical Engineering

Advised by
Dr. Tuhin Das, Assistant Professor, Mechanical Engineering
Department of Mechanical Engineering
Kate Gleason College of Engineering
Rochester Institute of Technology
Rochester, New York
April 2010

Approved By:

Dr. Tuhin Das,
Assistant Professor, Mechanical Engineering
Advisor

Dr. Kathleen Lamkin-Kennard,
Assistant Professor, Mechanical Engineering

Dr. Agamemnon Crassidis,
Associate Professor, Mechanical Engineering

Dr. Wayne Walter,
Professor, Mechanical Engineering

Dr. Edward Hensel,
Department Representative, Mechanical Engineering

Thesis Release Permission Form

Rochester Institute of Technology

Kate Gleason College of Engineering

I, Eric R. Steffan, hereby grant permission to the Wallace Memorial Library to reproduce my thesis in whole or part.

Eric R. Steffan

Eric R. Steffan

4/28/2010

Date

Dedication

I dedicate this thesis to my parents for their loving support, both emotionally and financially over the course of my life. Thanks for always encouraging my hobbies and supporting my choices in life. Dad, thanks for teaching me through example what it means to have direction while keeping an open mind, and Mom, thanks for continually putting others above your own interests. I wouldn't be where I am today without each of you.

Acknowledgments

Thanks firstly to my advisor Dr. Tuhin Das for providing abundant energy, excitement, and wisdom. Thanks to Dr. Kathleen Lamkin-Kennard for her knowledge of cellular locomotion, Dr. Agamemnon Crassidis for his knowledge of systems and control theory, and Dr. Wayne Walter for his knowledge of robotics implementation. Also, thanks to former RIT graduate student Dave Gomez for his support and knowledge of signal processing, my uncle Joe Feyes for coming up with the name of our robot, and finally, a special thanks to my brother Peter Steffan for offering hours of his time and expertise in creating an animation of the first prototype, using Maya software. The chief purpose of the animation was to demonstrate our design concept at the 2009 ASME Dynamic Systems and Control Conference in Hollywood, California. Lastly, I acknowledge the generous support for fabrication of the prototype, provided through a Faculty Education & Development (FEAD) Grant in 2008-2009 by the office of the Dean of Engineering.

Abstract

This work develops an analytical basis for designing the locomotion of mobile robots with a circular core and equispaced diametral legs which actuate linearly. Two elementary regimes of motion are first developed using the intrinsic geometry of the mechanism, then combined for fluid motion. The first and primary gait has a path trajectory defined by its kinematic constraints. Dynamics are explored to assist actuator design and understand the mechanism's constraint forces. Simulation results are provided in support of the design concept and geometric optimization. The proposed robot, or Locomotive Amoebic Device (LAD), bears resemblance with certain cellular locomotion, and thus miniaturization is a possibility. A prototype of LAD is constructed which supports the design theory and simulation by executing the primary motion regime with appropriate speed and current settings. Future work is promising for extending the design to a spherical concept, generalizing the theory in terms of the number of legs, creating a variety of control schemes for maneuvers such as dampening phase transitions or pure rolling, equipping and justifying the design for applications such as Planetary Exploration or Medical Procedures, and potentially creating a millimeter scale version or smaller of spherical LAD. This thesis theorizes a unique mode of locomotion and proffers simulation and experimental support.

Contents

List of Figures

List of Tables

Nomenclature

Abbreviations

Term	**Meaning**
Ph.1	Phase I, motion regime with two points of contact with ground
Ph.2	Phase II, motion regime with one point of contact with ground
leg 1	Hind leg during Phase I
leg 2	Foreleg during Phase I, pivoting leg during Phase II
leg 3	Leg to replace leg 2 after one cycle of Phases I and II
C	Point C, the cores center
P	Point P, Origin, leg 1 contact with ground
Q	Point Q, leg 2 contact with ground
LAD	Locomotive Amoebic Device, a.k.a. the proposed robotic mechanism
NASA	National Aeronautics and Space Administration
DOF	Degree(s) of Freedom
COF	Coefficient of Friction
MOI	Moment of Inertia
PID	Proportional Integral Derivative
CLAW	Control Law
e	Error
u	Control Effort
K_p	Proportional Gain
K_i	Integral Gain
K_d	Derivative Gain
FFT	Fast Fourier Transform
TTL	Transistor-to-Transistor Logic

RC	Resistor Capacitor
GUI	Graphical User Interface
CR	Carriage Return
τ	Time constant $[sec]$
f_c	Cutoff frequency $[Hz]$
F_N	Nyquist frequency $[Hz]$
F_S	Sampling rate $[Hz]$
BOM	Bill of Materials
FHCS	Flat Head Cap Screw
BHCS	Button Head Cap Screw
FT	Fully threaded
LDPE	Low-Density Polyethylene
PD	Pitch Diameter
OD	Outer Diameter
ID	Inner Diameter
NEMA	National Electrical Manufacturers Association
LVDT	Linear Variable Differential Transformer
CAD	Computer Aided Drawing
CPU	Central Processing Unit
BNC	Bayonet Neil-Concelman
RCA	Radio Corporation of America
dSPACE	Digital Signal Processing and Control Engineering

Notation

Symbol	**Definition**
r	Radius of circular core $[m]$
r_i	Leg i extension, where $i = 1, 2, 3$ $[m]$
L	Total length of each leg $[m]$

N	Number of legs
θ	Angle between leg 1 and ground [deg]
β	Angle between leg 2 and ground [deg]
ϵ	Angle between each pair of legs [deg]
a	Distance between points of contact with ground - Phase I [m]
R	Radius of circle described by center C - Phase I [m]
$\mathcal{R}$	Turning radius [m]

$r_{1,0}$	Initial r_1 value - Phase I [m]
θ_0	Initial θ value - Phase I [m]
β_0	Initial β value - Phase I [m]
θ_{tip}	Final θ value - Phase I [m]
β_{tip}	Initial β value - Phase II [m]

M_d	Mass of core or disk [kg]
M_r	Mass of each leg or rod [kg]
M_{eq}	Mass of core equivalent, e.g. $M_d + M_r$ [kg]
I_c	Moment of inertia of core about C [$kg \cdot m^2$]
I_{eq}	Moment of inertia of core about C equivalent [$kg \cdot m^2$]
I_P, I_Q	Moment of inertia of mechanism about P and Q [$kg \cdot m^2$]
$I_{r,P}$, $I_{r,Q}$	Moment of inertia of legs about P and Q [$kg \cdot m^2$]
g	Earth’s gravitational constant [$kg \cdot m/sec^2$]

h	Height of cores center, C, a.k.a y_c [m]
h_0	Initial height of center C [m]
$y_{max,1}$	Maximum height of center C during Phase I [m]
$y_{max,2}$	Maximum height of center C during Phase II [m]
$q_{max,1}$	Maximum vertical departure of C from h_0 during Phase I [m]

$q_{max,2}$	Maximum vertical departure of C from h_0 during Phase II $[m]$

y_c	Position of C, vertical component $[m]$
z_c	Position of C, horizontal component $[m]$
$y_{r,1}$	Position of leg 1 centroid, vertical component $[m]$
$z_{r,1}$	Position of leg 1 centroid, horizontal component $[m]$
$y_{r,2}$	Position of leg 2 centroid, vertical component $[m]$
$z_{r,2}$	Position of leg 2 centroid, horizontal component $[m]$

v_C	Velocity of the cores center C $[m/sec]$
$v_{C,y}$	Vertical component of velocity of center C $[m/sec]$
$v_{C,z}$	Horizontal component of velocity of center C $[m/sec]$
v_{C1-}	Velocity of C immediately before transition to Phase II $[m/sec]$
v_{C1+}	Velocity of C immediately after transition to Phase II $[m/sec]$
v_{C2-}	Velocity of C immediately before transition to Phase I $[m/sec]$
v_{C2+}	Velocity of C immediately after transition to Phase I $[m/sec]$
$\dot{\beta}_{tip}$	Angular velocity about Q immediately after transition to Phase II $[rad/sec]$

F_{m1}	Actuation force for leg 1, Phase I $[N]$
F_{m2}	Actuation force for leg 2, Phase I $[N]$
F_B	Braking force for leg 2, Phase II
F_{t1}	Reaction force tangential to leg 1 $[N]$
F_{t2}	Reaction force tangential to leg 2 $[N]$
T_1	Reaction torque of leg 1 $[N \cdot m]$
T_2	Reaction torque of leg 2 $[N \cdot m]$
$R11$	Friction force of leg 1 with ground $[N]$
$R12$	Normal force of leg 1 with ground $[N]$
$R21$	Friction force of leg 2 with ground $[N]$

$R22$	Normal force of leg 2 with ground $[N]$

μ_1	Coefficient of friction, leg 1, Phase I
μ_2	Coefficient of friction, leg 2, Phase I
μ_3	Coefficient of friction, Phase II

Δt_1	Time to complete Phase I $[sec]$
Δt_2	Time to complete Phase II $[sec]$
$v_{C,ref}$	Reference or desired velocity of C
$v_{C,T}$	Target velocity of C before transition to Phase II, $\geq v_{C1-}$
λ	Constant determining $v_{C,ref}$ curve
$\dot{r}_{i,ref}$	Reference velocity for leg i, where $i = 1, 2, 3$ $[m/sec]$

ϕ_i	Leg i Motor angular displacement, where $i = 1, 2, 3$ $[rad]$
ω_i	Leg i Motor angular velocity $[rad/sec]$
τ_i	Leg i Motor pull-out torque $[N \cdot m]$
P_i	Leg i Motor output power $[W]$
$P_{req,i}$	Leg i Motor input power $[W]$
ρ	Pinion radius $[m]$
ζ	Actuator efficiency [%]
$\mathcal{N}$	Speed reducer ratio
η	Efficiency of speed reducer [%]

Subscript	**Definition**
avg	Average
$approx$	Approximation
T	Target

Chapter 1

Introduction

Mobile Robotics is a vast area of research that has experienced rapid development in recent years. In the majority of robotic designs, mechanisms for self-propulsion have been inspired by various forms of locomotion that are observed in nature. Nonetheless, this work originates a mechanism with a mechanical simplicity not found in nature. Yet, advantageously, the mechanism resembles the motion of a certain class of cellular organisms. This thesis develops an analytical basis for the locomotion of a class of robotic rolling mechanisms with linearly actuated legs. Simulation and experimentation demonstrates the fundamental principles of motion discussed in the analysis.

1.1 Motivation

The concept originates from earlier research conducted by Das et al. [9], [1] where the author's advisor developed and analyzed internal propulsion mechanisms for circular and spherical robots. A diagram of Spherobot, the mass unbalance rolling robot mentioned above is contained in Figure 1.1. This thesis explores the class of circular and spherical rolling robots that rely on an external propulsion mechanism of translating legs. One hope is that since the proposed mechanism uses external propulsion as opposed to the more complicated internal propulsion mechanisms, its geometry aids in the path trajectory or upper level control, and it resembles a certain class of cellular organisms, that it is conducive to miniaturization. Another promising feature of the mechanism is its inherent, postural robustness akin to spherical robots, that is, its configuration can be recovered easily, even after a disturbance of large force such as a gale.

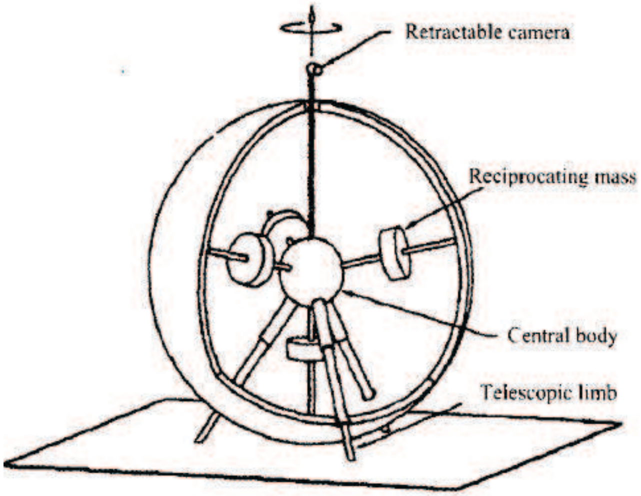

Figure 1.1: Das et al. Spherobot - mass unbalance concept [1]

The robotic mechanism can be conceived as a spherical core with retractable legs oriented radially over the surface of the sphere. It is maneuvered by controlling the relative protrusion of the legs. A planar version of the mechanism is depicted in Figure 2.1. This thesis considers rectilinear motion of a circular core with radial legs. A salient feature of the mechanism is its overall shape morphing ability, giving it an amoeba-like persona. Leg protrusion and retraction can be controlled to cause motive reaction forces while simultaneously providing a favorable mass unbalance aiding the locomotion. The mechanism is named LAD, or Locomotive Amoebic Device.

As mentioned briefly above, the design resembles *cellular locomotion of neutrophils*, or a type of white blood cell, as shown schematically in Figure 1.2. Neutrophils have a simple yet effective mechanism for propulsion, using expanding and contracting tentacles to propel themselves forward in the presence of shear flow, [2], [10], and [11]. Neutrophils rely on chemical bonds between tentacles and body tissue walls rather than friction between the ground and feet.

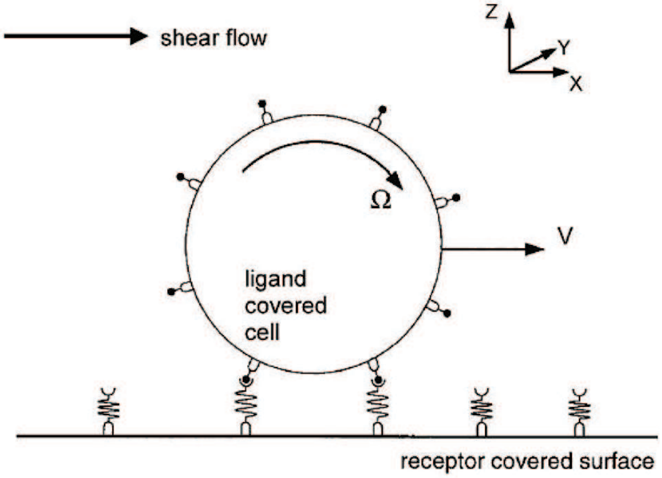

Figure 1.2: Neutrophil motion [2]

The similarity between neutrophil and LAD not only demonstrates the potential feasibility of the proposed concept of motion on a microscopic scale, but also motivates the author to explore the underlying principles of neutrophil's cellular locomotion, searching for ways to improve LAD's design. This is an example of Biomimetics, of which the basic ideas are illustrated in [12]. For example, neutrophil uses its surroundings to provide it with energy, i.e. shear flow, and the equivalent of that in this thesis' design could be using wind to aid in rolling, or using solar energy from the sun by having solar panels on feet bottoms. Observations of this type are essential to achieve a high degree of miniaturization, since power is perhaps the chief obstacle to microrobotics, [13]. As objects become smaller the surface area to volume ratio increases dramatically, and it is the case that batteries store energy per unit volume. Therefore, to siphon energy from the environment is an appealing avenue to investigate with regards to microrobotics. Another challenge to miniaturization is precision in manufacturing, discussed in [14]. Examples of micro robots are found in [15].

Practically speaking, if LAD is inexpensive, small, able to scale relatively rough terrain, and robust, hundreds of them could potentially be distributed on martian terrain for data sampling. Alternatively, if LAD has long legs it could potentially traverse rough terrain. A survey of mobile robots for planetary exploration is conducted in 1996 by [16], and consists primarily of wheeled vehicles or walking robots. An example of a biologically inspired mechanism for planetary exploration is a Hexapod inspired by the cockroach, which claims to have maneuverability through rough terrain, and is found in [17]. Perhaps the exploring mechanism most similar to the proposed design concept is a Tumbleweed rolling robot from [3], which is currently being investigated by NASA for surveying vast landscapes. The mechanism, shown in Figure 1.3, relies on wind for locomotion and deploys various cameras, tunneling mechanisms, and sensors for collecting data.

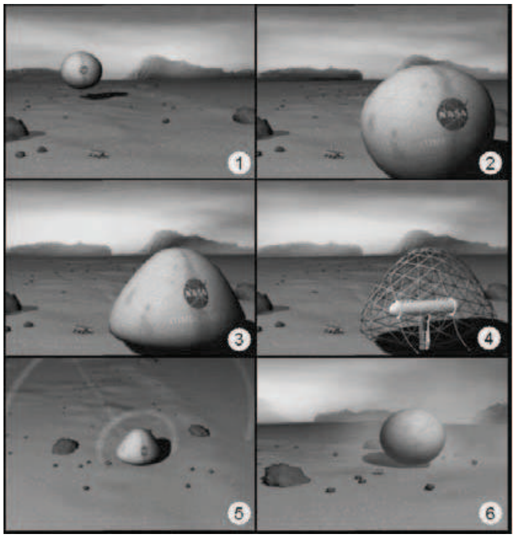

Figure 1.3: NASA/JPL Tumbleweed Polar Rover [3]

As a long term hope, if LAD is miniaturized to a great degree, and its simplicity affords equipping for medical procedures, it may assist or accomplish in vivo operations such as releasing chemicals or collecting images and data. Similar to the neutrophil, LAD would attempt to utilize fluid flow to aid locomotion. A prototype of the *In vivo* wheeled robot designed to assist laparoscopy surgery is found in [18] and a review of laparoscopy robotics is in [19], and an inch worm type robot for a gastro-intestinal intervention system is shown in Figure 1.4 and discussed in [4].

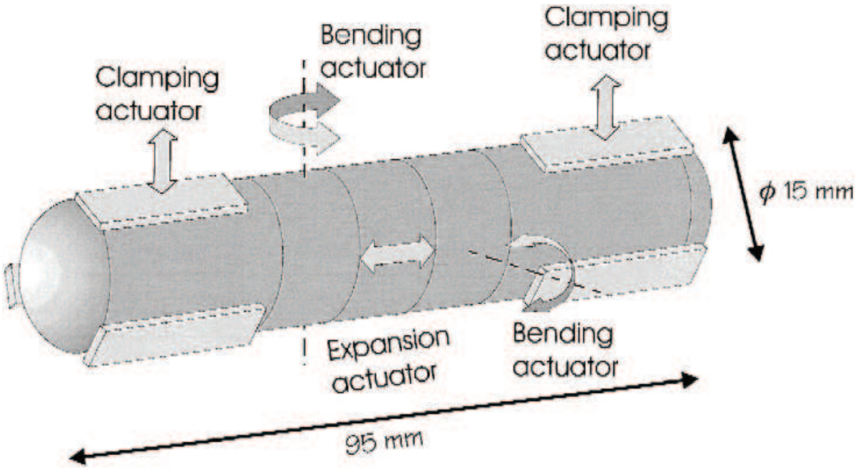

Figure 1.4: Inchworm-type robot for inspection of the colon [4]

In sum, the author explores a unique class of circular robots with diametrically translating legs. The design concept is begot from Das' Spherobot. LAD's traits such as simplicity, postural robustness, and similarities with neutrophil, allow the potential for both miniaturization and biomimetics, or the reverse engineering of living organisms. Another motivating factor of LAD's simplicity is the versatility that it begets, discussed in the next section, which will potentially lead to applications in Planetary Exploration and Medical Procedures.

1.1.1 Versatility of Concept

The simplicity of LAD allows a large degree of versatility in design. Characteristics such as the leg length, L, and the number of legs, N, can change the functionality of the robot. As L increases, the capacity to travel rough terrain increases, and as N increases, the potential to utilize mass-unbalance and reduce energy costs increases, however, the complexity does also.

There is potential for LAD to use its environment for energy: by decreasing its mass and increasing the surface area of the feet bottoms it can become a tumbler, using the wind to propel itself, akin to the design by NASA in the third last paragraph of Section 1.1 above.

To scale large objects the overall scale of LAD can increase along with L, and modes of operation similar to pole-vaulting may be applied, which is accomplished by Virginia Tech's IMPASS from Subsection 1.3.2. To enter small spaces the overall scale of LAD can decrease by using principles from the operation of neutrophil, and potential for burrowing exists if a leg is substituted for a drill and LAD is equipped with explosives.

Alternative modes of travel can be conceived, such as pure rolling, which is possible if the robot has telescopic legs that retract to transform LAD into a ball. Functions can be added by replacing legs with devices, such as a spear, drill, laser, or by replacing the feet with sensors or solar panels.

Thus, LAD's simplicity allows versatility in its designs. There is potential for LAD to miniaturize, enlarge, and utilize its environment for energy. Finally, simplicity is incredibly helpful for a robot to be equipped with the necessary tools to complete a worthy task, such as space exploration or medical procedures.

1.2 Generic Description of Rolling and Undulating Robots

It is a challenge to place LAD in a category of Robotics since it pseudo walks, rolls, and undulates, and it has potential to be a microbot, mimic nature, or fulfill various applications. Thus, the generic fields pseudo represented by LAD are Walking Robotics, Rolling Robotics, Undulatory Robotics, Microrobotics, and Biomimetics; with the strongest correlation to LAD being Rolling Robotics, followed by Undulatory Robotics.

Rolling Robots' locomotion is best explained and reviewed by paper [5], as this paper covers both rolling mechanisms found in nature and state of the art rolling robot designs. In nature, there is the tumbleweed, Namid wheeling spider, Mother-of-pearl caterpillar, Stomatopod shrimp, and in Robotics, there is Rollo from Figure 1.5 below, Spherical Mobile Robot, Sphericle, Spherobot from Figure 1.1 above, August, Deformable robot, Kickbot, Gravitational wheeled robot, Gyrover, Roball, and Rotundus. All of these designs are representative of different locomotion principles for internal propulsion mechanisms, primarily for spherical robots, but some have not yet progressed from the cylindrical stage.

An in depth design of an internal propulsion spherical mobile robot, BHQ-1, based on a rotating, swinging mass principle, is found in [20].

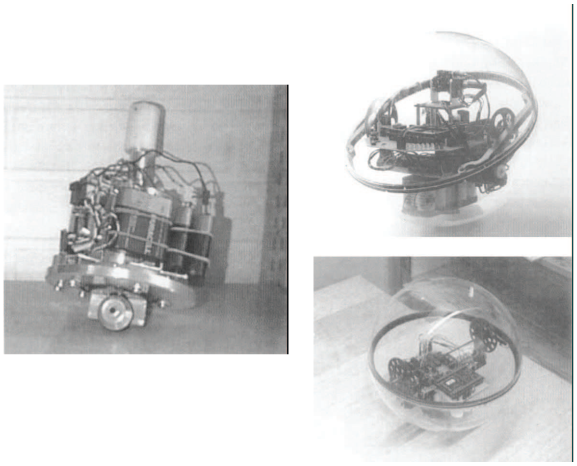

Figure 1.5: Helsinki Tech's Rollo - sprung central member concept [5]

Note that the picture on the left is the initial Rollo prototype, and on the right is the third prototype; it has replaced its original sprung central member concept, and it has a diameter of 0.24 m, mass of 3 kg, speed of 0.5 m/s, and peak current consumption of 0.8A.

Undulatory Robots are essentially those which change their body shape to produce a motion path. They include snakes, which move their bodies rhythmically as a motion gait, or amoebas, which literally change the shape of their outer skin to produce motion and can also be classified as Shape-shifters. The geometric mechanics of undulatory locomotion are presented in [21], which includes a model derived from the geometry of Snakeboard, which mimics a serpentine gait. Another geometric approach is found in [22] for eel-like motion akin to three, five, and ten link snakes. Similarly, LAD's intrinsic geometry is used to predict the motion path of the robot, and the undulation of the invisible outer skin occurs as legs are coordinated to translate for efficient motion to occur. Another classic example of undulatory motion is the nematode C. elegans, a 1mm long roundworm, whose motor control model is found in [23]. [24] is a paper on undulation via Whole Skin Locomotion, inspired by amoebae.

1.3 Varieties of Rolling Robots with Linearly Actuated Legs or Wheels with Legs

Designs with certain conceptual similarities to LAD are found in the literature. Most of the following varieties of rolling robots incorporate linearly actuated legs, similar to the proposed design. In comparison to the designs below, however, the proposed mechanism generates rectilinear locomotion exclusively through linear actuation of the legs. Also, the mechanism functions independently using one circular core instead of coaxial wheel pairs adopted in some designs below.

1.3.1 Retractable Legs

The authors of [25] discuss a hexapod insect-like mechanism with retractable legs. In this design, apart from the axial motion, each leg is also allowed to swing.

1.3.2 'Whegs'

In [26] the authors design walking robots with six compliant legs. Each leg is designed as a combination of three equispaced spring-loaded telescopic spokes forming a wheel, called 'Wheg', where the discontinuities are used to gain footholds. In this design, each 'Wheg' has rotational actuation about the center, in addition to the leg compliance. A miniature version of a 'Wheg' vehicle with adhesive feet for wall climbing is in [27].

Similarly, The Intelligent Mobility Platform with Active Spoke System (IMPASS), is a mechanism consisting of two actuated-spoke wheels connected through a common axle. [28] describes the spoke wheels to be connected with a central hub in [29]. A master's thesis [6] describes the implementation of said robot. In addition to the radial spoke actuation, rotational torque is provided to the axle through a hub motor. An extra point of contact with ground is provided by a tail support.

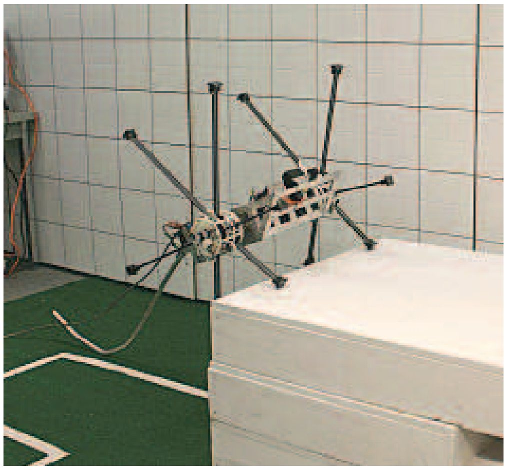

Figure 1.6: Virginia Tech's IMPASS - linearly actuated spoke wheels [6]

Lastly, in [30], the authors discuss a rimless wheel with radially expanding legs, intended to be used on the three-wheel vehicle discussed in [31], or similar vehicles. The wheel consists of three spokes simultaneously actuated by a bevel gear in conjunction with ball screw and pinion assemblies. Radial extension is intended to catapult the vehicle over obstacles by expanding when a single spoke is in contact with the ground. The wheels can also be rotated via a central hub, allowing two degrees of freedom in the motion of the wheel.

1.3.3 Tumblers

A rolling robot in [7], with independently actuated legs, tumbles in any direction. This design, shown in Figure 1.7, is similar to the proposed mechanism, however, the approach is experimental in nature and induces slip, whereas this thesis designs a complete analysis and provides gaits differing from the Tumbling Robot which utilize the geometry in a unique way with no slip.

Another robot capable of tumbling is a Platonic Beast with 4 legs using a rolling gait in [8]. This design, shown in Figure 1.8, relies on multiple linked legs, which are not linearly actuated, to accomplish the gait. The intrinsic geometry is not used to provide a motion path. It is a more complicated design than LAD and thus less conducive to miniaturization or versatility, however, it has the capacity to perform more complex gaits such as carrying an object.

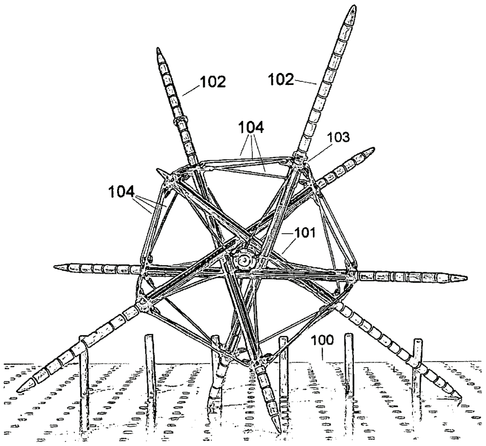

Figure 1.7: A.G.Hlyanka et al. Multiple Leg Tumbling Robot [7]

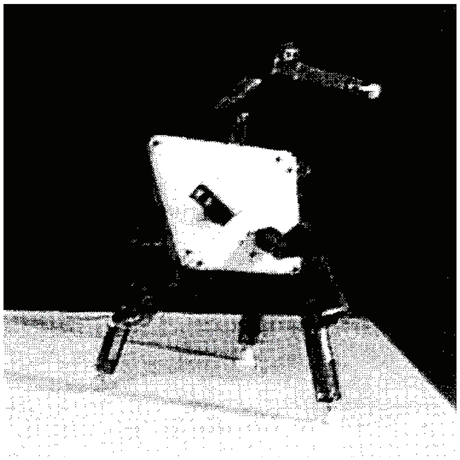

Figure 1.8: Platonic Beast - 4 limbs each with 3 joints [8]

1.4 Objectives

This work introduces a unique method of designing rolling robots with linearly translating legs, specifically from an analytical vantage point. For instance, the proposed locomotion is designed with two distinct phases, each of which has a motion path describable by mathematics. In Phase I, mechanical energy is supplied into the system through controlled actuation of the legs. The momentum gained in the process is then used to complete Phase II which simply utilizes energy conservation. A pair of Phase I and II motion regimes are repeated to generate the overall locomotion. The analytical development is carried out with three equispaced, linearly actuated legs, positioned around a circular core. The choice of three legs is prompted by the use of three linearly actuated unbalance masses in the locomotion of Das et al.'s rolling disk in [9], however, the concept is applicable to an arbitrary number (potentially ≥ 2) of equispaced diametral legs. Optimization of the design is considered where appropriate for a 2D version.

The author supports the analysis, which includes kinematics and dynamics, with both simulated and experimental results. A prototype of the planar version of LAD is constructed, Phase I is achieved, and methods for further control of the device are currently being explored. A long term hope is to realize applications in Planetary Exploration, potentially for Medical Procedures such as in vivo operations, or even in an area that is yet to be discovered.

Chapter 2

System Description

The mechanism LAD, or Locomotive Amoebic Device, is conceptualized as a structure whose overall shape resembles an amoeba, yet its motion regime in detail resembles a neutrophil, or a certain class of white blood cells, as shown in Section 1.1. The robotic mechanism concept is demonstrated in Figure 2.1 below:

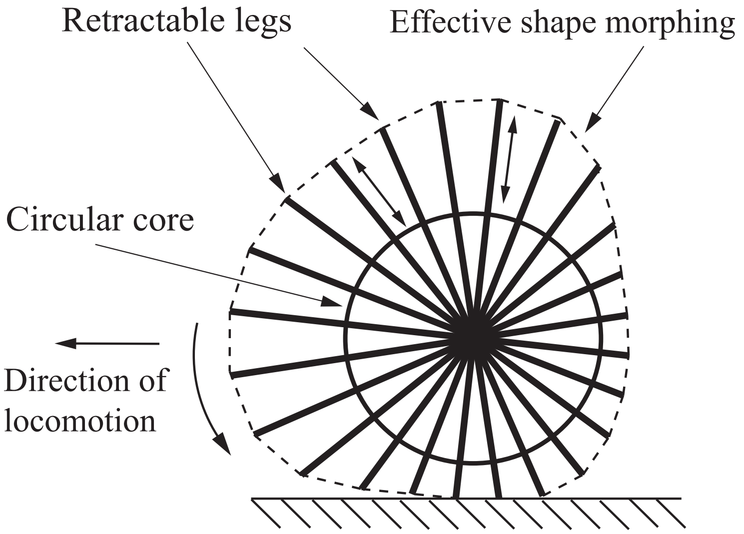

Figure 2.1: Robotic mechanism concept

The mechanism consists of a circular core with N equispaced retractable legs. Each leg is along a diametral line of the circular core and can translate axially. The mechanism generates locomotion by controlling the radial motion of each leg. It is important to note that the design concept, as it stands, has only one DOF per leg, that is, the angles between the legs are constant and equal. To approach the design concept from this perspective is to rely on the intrinsic geometry of the structure for motion, as opposed to complicating the system with additional degrees of freedom to force a desired motion path. A unique aspect of the design is the effective shape morphing capability achieved by the robot, as shown by the dotted line in Figure 2.1. This happens due to the continuous change in the relative positions of the legs and is achieved in spite of the absence of a flexible outer covering or skin with an internal morphing mechanism. Two apparent advantages of this characteristic are: 1) the shifting of LAD's center of mass, which can be designed to aid the overall rolling motion of the robot, and 2) the potential to traverse uneven or rough terrain. A natural concern, however, is fouling of the legs. In a practical implementation this issue can be addressed by offsetting the legs in the lateral direction or by constructing each leg with two parallel bars. By choosing a different spacing between the bars of each leg, the legs will pass through one another without being offset and hence the latter approach would maintain a more balanced posture in the lateral direction.

While Figure 2.1 represents the general concept, it is important to analyze the mechanism and design feasible modes of locomotion. Hence, in this thesis, the author studies the specific case of three legs. The choice is motivated by Das et al.'s earlier research [9] where three unbalanced masses were used to generate rectilinear locomotion of a self-propelling rolling disk. A schematic diagram of the robot and its relevant coordinates is given in Figure 2.2(a).

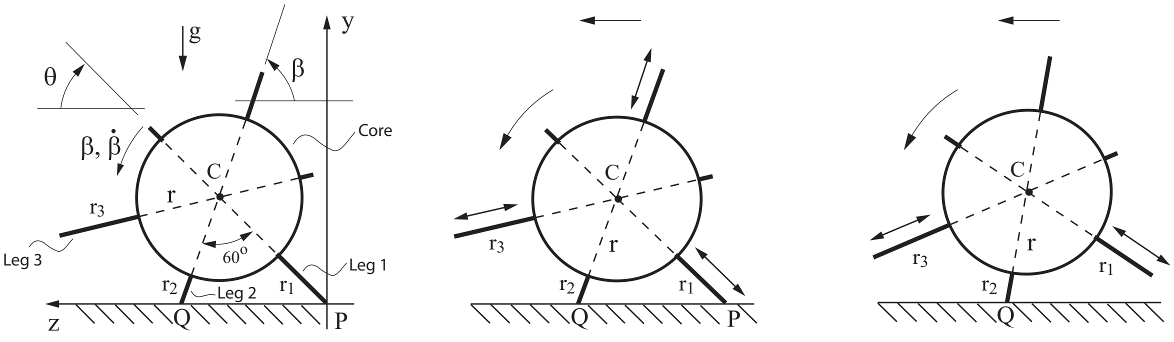

a) Diagram with generalized coordinates

b) Phase - I

c) Phase - II

Figure 2.2: Diagram of the robotic mechanism

Another parameter affecting the mode of locomotion is the number of contact points the legs make with the ground. Clearly, with one point of contact, the mechanism will behave as an inverted pendulum. When two points are in contact with the ground the effect is described in Chapter 3. Three or more points of contact with the ground produces more stable motion, however, on a level surface it over constrains the system and induces slipping. Virginia Tech's robot IMPASS, [28], fluctuates primarily between one and two point contact, similar to the proposed design, yet it relies on the presence of another spoke-wheel and a central hub which is providing rotation of the wheel cores. On the contrary, LAD has the capacity to function as an independent spoke-wheel, with only three degrees of freedom or one per leg, which lends itself to the motion path being defined in mathematical terms for one and two point contact motion regimes.

Chapter 3

Motion Analysis

In order to generate motion with a single spoke-wheel, the most advantageous approach is to define the motion analytically, to maintain control and flexibility over the controls design. For the purposes of this thesis, the number of legs is constrained to three, and the points of contact with the ground to either one or two. Another assumption is level ground, and the focus is on linear motion.

3.1 Motion Regime Philosophy

There are multiple ways to produce linear motion with the above constraints. One such way is to have a two point contact motion regime repeated. With this approach the path of the robot's center will be defined by the linear translation of the legs in contact with the ground. Due to constraints which are discussed in Section 3.2 and with greater detail in Appendix A, and also verified experimentally, the path trajectory of the center will be a circular arc from the top half of a given circle. Instead of repeating this two point contact regime, another option is to alternate between two point and one point contact. It is clear that the mechanism must begin with two points of contact for stability; thus, the motion consists of a two point contact regime, followed by a one point. This pattern is repeated to offer an alternate linear motion scheme. Motion regimes are summarized below in Table 3.1:

Table 3.1: Motion regimes summarized

Linear Motion Along a Level Surface with No Slip		
Item	Motion Regime	Plausible Combinations
1	One point contact	2-1-2-1-...-2-1-2
2	Two point contact	2-2-2-2-...-2-2-2
3	Three point contact	≥3 requires Uneven surface and/or Slip

For two primary reasons the author designs the locomotion of the robot as an alternating sequence between two and one point contact versus the repetition of a two point contact regime: 1) a larger horizontal distance is covered before the robot must re-initialize, and 2) the energy expended over a given distance is smaller. Qualitative reasoning asserts that the addition of a second motion regime, which relies solely on momentum, increases the horizontal distance covered before the motion repeats, and reduces the energy cost for motion. Until firm quantitative comparisons are made between the two motion schemes, the alternative scheme of repeating the two point contact regime must be held in consideration. The two phases are as follows:

- **Phase I, or Ph.1 (Two point contact):** The robot uses two contact points on the ground to propel its center along a circular arc from the top half of a given circle, Figure 2.2(b) above.
- **Phase II, or Ph.2 (One point contact):** The robot rolls about a fixed point of contact with the ground, Figure 2.2(c) above.

3.2 Kinematics of Phase One

The motion in Phase I relies upon the kinematics obtained from the intrinsic geometry of the structure. From Figure 2.2(b), with P and Q as the two fixed points of contact and the geometric constraint $\angle PCQ = \angle PC'Q = 60°$, the center C can only traverse a unique circular arc path. This can be proven and is also given by Euclid's Inscribed Angle Theorem, as described in Figure 3.1. Euclid's theorem is proved in [32], and is explained in Appendix A. A relationship between r_1 and θ is established via the Law of Sines and using the fact that $\beta = 120° - \theta$:

$$r_1 + r = 2R\sin(120° - \theta) \tag{3.1}$$

This equation is the fundamental constraint of the proposed motion regime, and acts as a governing force for no slip control as discussed in Section 6.2. Note that r, the radius of the core, is a constant, and a and R, radius of the circle with center O, are invariant during Phase I due to the fixed contact points P and Q. The following relations are deduced from Figure 3.1 with basic trigonometry and Eqn.(3.1):

$$a = \sqrt{3}R = \frac{\sqrt{3}(r + r_{1,0})}{2\sin(120° - \theta_0)} \tag{3.2}$$

where $r_{1,0}$ and θ_0 are the values of r_1 and θ at the initiation of Phase I. Differentiating Eqn.(3.1) with respect to time yields velocity and acceleration constraint equations

$$\begin{aligned} \dot{r}_1 &= -2R\dot{\theta}\cos(120° - \theta) \\ \ddot{r}_1 &= -2R\left[\ddot{\theta}\cos(120° - \theta) + \dot{\theta}^2\sin(120° - \theta)\right] \end{aligned} \tag{3.3}$$

Phase I motion can be implemented through linear actuators to generate controlled relative motion between the circular core and each leg.

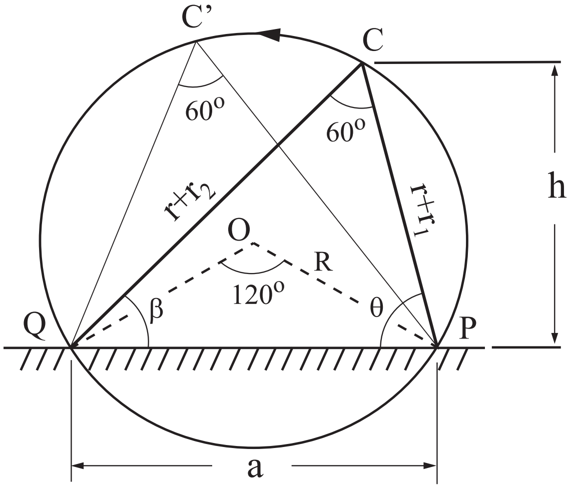

Figure 3.1: Circular trajectory of center during Phase I

From Figure 3.1 using basic trigonometry two expressions for h are derived as follows

$$h = (r + r_2)\sin\beta = (r + r_1)\sin\theta \tag{3.4}$$

Solving Eqn.(3.4) for r_2 yields

$$r_2 = \frac{\sin(\theta)}{\sin(120^\circ - \theta)}(r + r_1) - r \tag{3.5}$$

By differentiating Eqn.(3.5), combining with Eqns.(3.1) and (3.3), and using the trigonometric relations $\sin 2x = 2\sin x \cos x$ and $\sin x \cos y = 1/2[\sin(x-y) + \sin(x+y)]$, a velocity constraint for r_2 is obtained in the following form:

$$\dot{r}_2 = -\left[\frac{\left(2\sin(2\pi/3 - 2\theta) + \sqrt{3}\right)}{2\sin(4\pi/3 - 2\theta)}\right]\dot{r}_1 \tag{3.6}$$

3.3 System Model of Phase Two

The motion in Phase II is a rotational motion as shown in Figure 2.2(c). The robot relies on its momentum to tip over the single point of contact. The center C again traverses a circular path during this phase. While the motion during one point contact can be designed in multiple ways, in this specific design there is no relative motion between the circular core and the supporting leg. Thus, the robot tips over Q as a rigid body and purely by virtue of its momentum. The rigid body mode can be implemented through a braking force applied by the leg 2 linear actuator. During Phase II the robot therefore behaves as an inverted pendulum, with an initial configuration of that shown in Figure 3.2 below.

Assuming the height h of the cores center to be equivalent at the start of each phase, that is, h_0, then several of the parameters in Figure 3.2 are known by deduction: $r_2 = r_{1,0} = constant$, and $\beta = \theta_0$. For more clarity, view Figure 3.3 in Section 3.4.

3.3.1 Lagrange Equation

Assumptions: No slip, Legs are rigid and massless, Neglect wind resistance

Using Figure 3.2, Kinetic, Potential, and Lagrangian terms are defined:

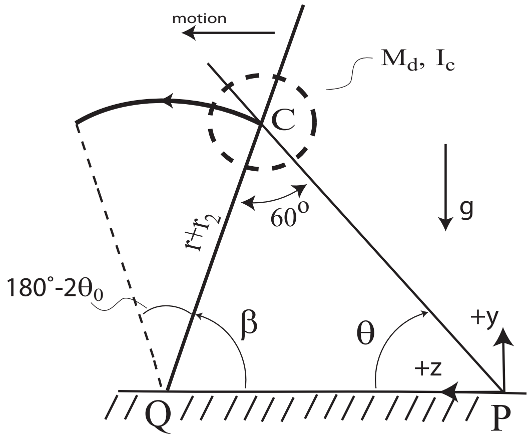

Figure 3.2: Phase II motion diagram - initial configuration

$$T = 1/2 I_Q \dot{\beta}^2$$

$$V = M_d g (r + r_{1,0}) \sin\beta$$

$$L = T - V = 1/2 I_Q \dot{\beta}^2 - M_d g (r + r_{1,0}) \sin\beta$$

With the Lagrange formula as follows, since effectively the only state variable is β

$$\frac{d}{dt}\left(\frac{\partial L}{\partial \dot{\beta}}\right) - \frac{\partial L}{\partial \beta} = 0$$

yields

$$\begin{aligned} I_Q \ddot{\beta} + M_d g (r + r_{1,0}) \cos\beta = 0 \\ \beta(0) = \beta_{tip} = \theta_0 \\ \dot{\beta}(0) = \dot{\beta}_{tip} \end{aligned} \tag{3.7}$$

where β is the angle between leg 2 and the ground, r is the core radius, $r_{1,0}$ is the initial length of leg one at the beginning of Ph.1, M_d is the mass of the core, I_Q is the moment of inertia of the core about point Q, and I_c is the polar moment of inertia of the core about point C. And $I_Q = I_c + M_d(r + r_{1,0})^2$ from the Parallel Axis Theorem, and by assuming the core is a solid cylinder, $I_c = 1/2 M_d r^2$.

3.3.2 Solution of Inverted Pendulum Equation

Obtaining a solution for the Phase II system model provides yet more control over Ph.2. Let

$$\alpha = I_Q = I_c + M_d(r + r_{1,0})^2 \tag{3.8}$$

$$\zeta = M_d g(r + r_{1,0}) \tag{3.9}$$

From Eqn.(3.7)

$$\begin{aligned}
\alpha \frac{d^2\beta}{dt^2} + \zeta \cos\beta &= 0 \\
\frac{d\beta}{dt}\frac{d^2\beta}{dt^2} &= -\frac{\zeta}{\alpha}\cos\beta \frac{d\beta}{dt} \\
\frac{d}{dt}\left(1/2\left(\frac{d\beta}{dt}\right)^2\right) &= \frac{d}{dt}\left(-\frac{\zeta}{\alpha}\sin\beta\right) \\
1/2\left(\frac{d\beta}{dt}\right)^2 &= -\frac{\zeta}{\alpha}\sin\beta + C \qquad (3.10) \\
\beta(0) = \theta_0 & \\
\dot{\beta}(0) = \dot{\beta}_{tip} &
\end{aligned}$$

at $t = 0$:

$$1/2\dot{\beta}_{tip}^2 = -\frac{\zeta}{\alpha}\sin\theta_0 + C$$

$$C = 1/2\dot{\beta}_{tip}^2 + \frac{\zeta}{\alpha}\sin\theta_0 \tag{3.11}$$

From Eqn.(3.10)

$$\frac{d\beta}{dt} = \sqrt{C - \frac{2\zeta}{\alpha}\sin\beta}$$

Integrating from β_{tip} to β

$$\int_{\theta_0}^{\beta} \frac{d\tau}{\sqrt{C - \frac{2\zeta}{\alpha}\sin\tau}} = t \tag{3.12}$$

where t is the time elapsed from the start of Phase II to β, C is defined by Eqn.(3.11), and α and ζ are defined by Eqns.(3.8) and (3.9).

3.4 Combined Gait

The combined gait of the robot is generated by a repeating sequence of Phase I and Phase II motions. Such a repeating sequence can be designed in multiple ways. The author considers the particular design shown in Figure 3.3 where the resulting motion of the robot's center is shown by the bold line.

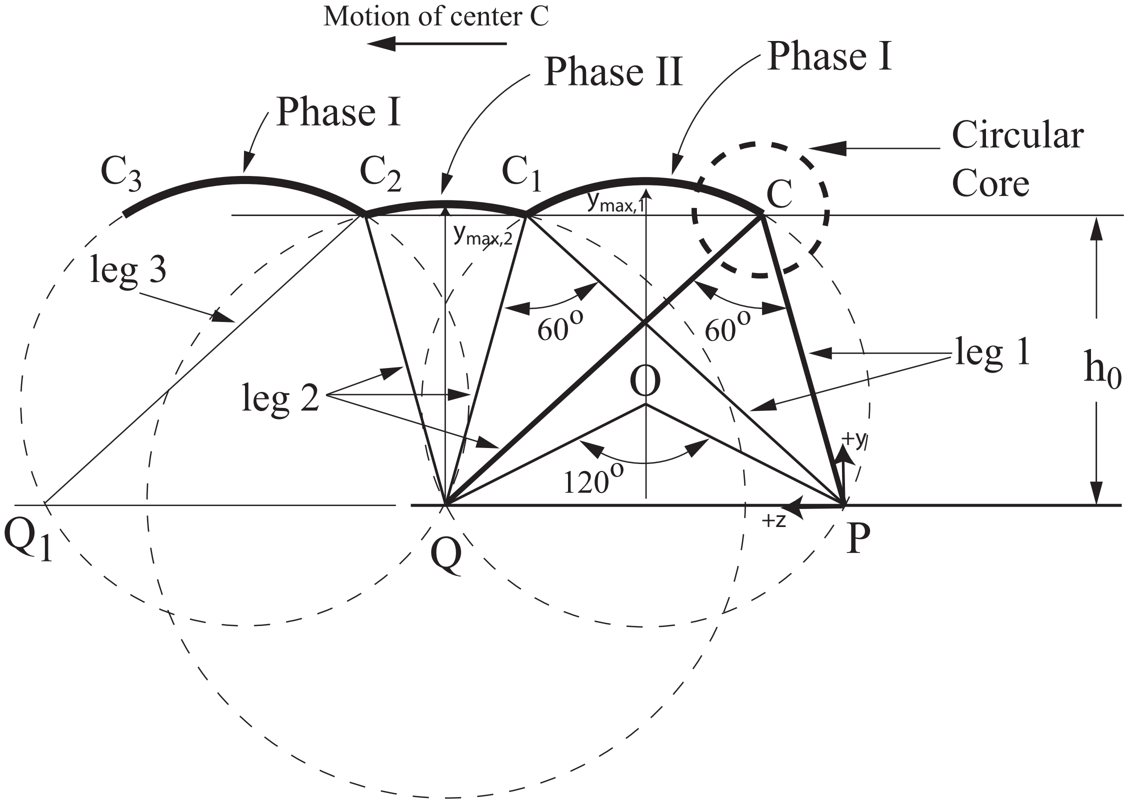

Figure 3.3: Combined gait

In Figure 3.3 the start and end of both phases occur at a constant vertical distance h_0 from the ground, as shown in Figure 3.3. This assumption admits not only the sequencing of Phases I and II with a continuous trajectory but also allows repetition of this sequence to generate a continuous motion. The motions $C - C_1$ and $C_1 - C_2$ correspond to Phase I and Phase II motions respectively. Note that since C, C_1, C_2 are at height h_0 from the ground, CC_2QP forms a parallelogram. Therefore, C_2 provides identical initial conditions as C for Phase I motion. However, at C_2, leg 2 replaces the former position of leg 1 at C, and leg 3 replaces leg 2, observed in Figure 3.3.

Note from Figures 3.3 and 3.1 that the location of the center C in Phase I is $(y_c, z_c) = ((r + r_1)\sin\theta, (r + r_1)\cos\theta)$, which implies the following:

$$v_C = \sqrt{\dot{z}_c^2 + \dot{y}_c^2} = \sqrt{\dot{r}_1^2 + (r + r_1)^2\dot{\theta}^2} \tag{3.13}$$

While the velocity of the center in Phase II is clearly

$$v_C = (r + r_{1,0})\dot{\beta} \tag{3.14}$$

Note also that from the parallelogram CC_2QP, the total horizontal distance traveled during Phases I and II is simply a, defined previously as the horizontal gap between contact points with the ground in Phase I. This allows the average horizontal velocity to be defined as follows:

$$v_{C,z,avg} = \frac{a}{\Delta t_1 + \Delta t_2} \tag{3.15}$$

Lastly, note that the trajectory of the robot is completely defined by the values of the following variables at the beginning of Phase I, $\angle CPQ = \theta_0$, $CP = r + r_{1,0}$. It is observed that for feasible trajectories, $r_{1,0} \geq 0$ and $60^\circ \leq \theta_0 \leq 90^\circ$. The values $\theta_0 = 60^\circ$ and $\theta_0 = 90^\circ$ correspond to terminal scenarios where the motion is exclusively Phase II or Phase I, respectively. While the latter scenario seems feasible in a practical implementation, the former is not, since a finite Phase I regime is required to input mechanical energy into the robot.

3.5 Phase Transitions

As noted earlier, while Phase I consists of controlled linear actuation, phase II motion relies completely on momentum. At the transition from Phase I to II, the relative motions of both legs 1 and 2 with respect to the circular core are stopped through a braking action. This causes the robot to tip over about the point Q in a rigid body mode. Thus, at the beginning of Phase II, the robot must have sufficient kinetic energy to undertake the intermediate height gain. It is important to note that at this transition, the abrupt braking of leg 2 will cause an *impulsive drop* in the velocity of center C. This is shown in Figure 3.4. The velocity of the center changes from v_{C1-} to v_{C1+}.

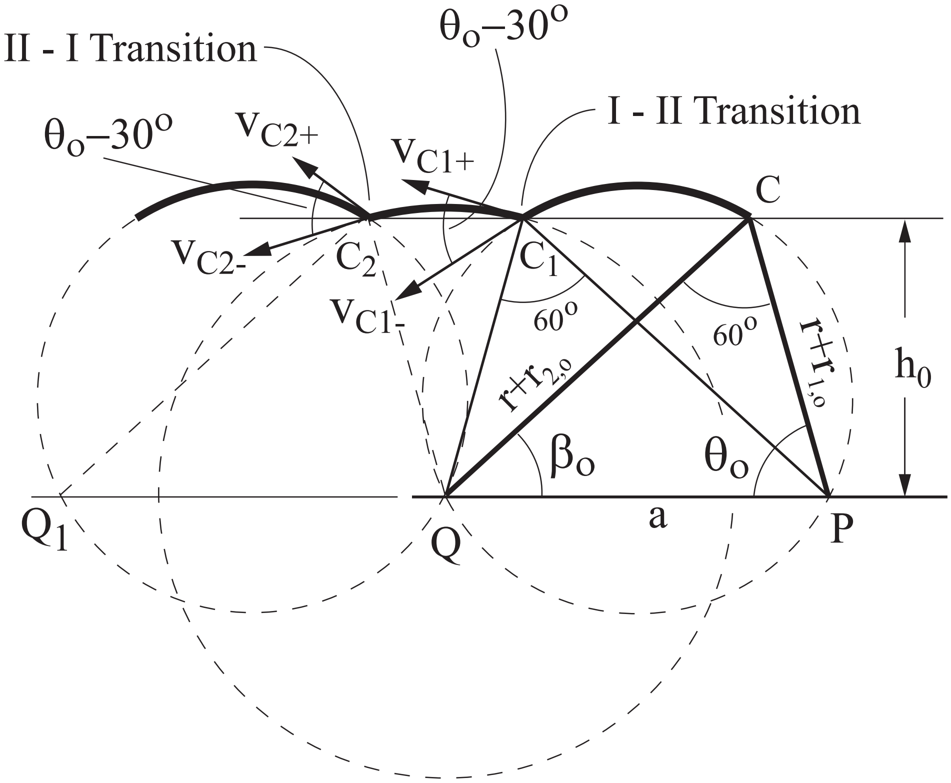

Figure 3.4: Impulsive effects during phase transitions

Similarly, at the transition of Phase II to I, the velocity of center changes impulsively from v_{C2-} to v_{C2+}. At this later transition, the robot enters the Phase I regime where energy is again pumped into the system in a controlled manner through the linear actuators. From conservation of mechanical energy during Phase II, $v_{C2-} = v_{C1+}$. Also, from the geometry of the combined gait, and Euclid's Inscribed Angle Theorem, which is described in Appendix A

$$v_{C1+} = \cos(\theta_0 - 30°)v_{C1-} \quad \text{and} \quad v_{C2+} = \cos(\theta_0 - 30°)v_{C2-} \tag{3.16}$$

From energy conservation, Eqn.(3.16), and the relationship $v_{C1+} = (r + r_{1,0})\dot{\beta}_{tip}$, it follows that Phase II is feasible if

$$0.5I_c\dot{\beta}_{tip}^2 + 0.5M_d v_{C1+}^2 M_d g(r + r_{1,0})\sin\theta_0 \geq M_d g(r + r_{1,0})$$

$$v_{C1-} \geq \frac{1}{\cos(\theta_0 - 30^\circ)}\sqrt{\frac{2(r + r_{1,0})^3(1 - \sin\theta_0)M_d g}{M_d(r + r_{1,0})^2 + I_c}} \tag{3.17}$$

where $\dot{\beta}_{tip}$ is the angular velocity of LAD about point Q at the start of Phase II. In the above equation, the legs are assumed to be rigid and massless.

Chapter 4

Motion Optimization

4.1 Goals and Schemes

The combined gait can be optimized in several ways based on geometric or energy schemes. Parameters that may be suitable for optimization include $\theta_0, r_{1,0}, a,$ and θ_{tip}. Optimization goals include maximizing smoothness of travel, minimizing vertical travel, and minimizing energy consumption. The authors present a geometric optimization of θ_0 to maximize smoothness of the piecewise circular trajectory of the robot, and another geometric scheme to obtain the θ_0 which minimizes vertical travel of the cores center. An energy based optimization of θ_{tip} to minimize energy consumption is also discussed briefly.

4.2 Geometry Based

4.2.1 Optimal Smoothness

In Figure 3.3, the points C, C_1, C_2, C_3, etc., all lie on a horizontal line, which is at a height h_0 from the ground. Define maximizing smoothness as minimizing the maximum vertical departure of C from h_0 during phases I and II, i.e., $\min\left(\max\left(\{q_{max,1}, q_{max,2}\}\right)\right)\ \forall\ r_{1,0} \geq 0$ and $60^\circ \leq \theta_0 \leq 90^\circ$. $q_{max,1}$ and $q_{max,2}$ are defined as

$$q_{max,1} = y_{max,1} - h_0, \quad q_{max,2} = y_{max,2} - h_0 \tag{4.1}$$

where, $y_{max,1}$ and $y_{max,2}$ are the maximum heights gained by the center C during phases I and II respectively. From Figures 3.3 and 3.4 and Eqn.(3.2), it's determined that

$$\begin{aligned} y_{max,1} &= R + R\sin 30^\circ = 1.5R = 3(r + r_{1,0})/\left(4\sin(120^\circ - \theta_0)\right) \\ y_{max,2} &= r + r_{1,0} \end{aligned} \tag{4.2}$$

From Eqns.(4.1) and (4.2)

$$q_{max,1} = q_{max,2} \;\Rightarrow\; \theta_0 = 71.41^\circ \tag{4.3}$$

Note from Figure 3.4 that,

$$h_0 = (r + r_{1,0})\sin\theta_0 \tag{4.4}$$

Hence expressing $q_{max,1}$ and $q_{max,2}$ as

$$\begin{aligned} q_{max,1} = y_{max,1} - h_0 &= 1.5R - 2R\sin(120^\circ - \theta_0)\sin\theta_0 \\ q_{max,2} = y_{max,2} - h_0 &= 2R\sin(120^\circ - \theta_0)\left[1 - \sin\theta_0\right] \end{aligned} \tag{4.5}$$

taking the derivative of $q_{max,1}$ and $q_{max,2}$ with respect to θ_0 and using Eqn.(3.2), it's observed that for $60^\circ \leq \theta_0 \leq 90^\circ$

$$\begin{aligned} \tfrac{\partial q_{max,1}}{\partial \theta_0} &= -2R\sin(120^\circ - 2\theta_0) \\ &\quad + \left(1.5 - 2\sin(120^\circ - \theta_0)\sin\theta_0\right)\tfrac{R}{\tan(120^\circ - \theta_0)} > 0 \end{aligned} \tag{4.6}$$

and

$$\frac{\partial q_{max,2}}{\partial \theta_0} = -\cos\theta_0\,(r + r_{1,0}) < 0 \tag{4.7}$$

This demonstrates that $q_{max,1}$ is an increasing function and $q_{max,2}$ is a decreasing function of θ_0 in the interval $60^\circ \leq \theta_0 \leq 90^\circ$. Therefore, $\min\left(\max\left(\{q_{max,1}, q_{max,2}\}\right)\right)$ occurs at $\theta_0 = 71.41^\circ$ and is independent of the choice of $r_{1,0}$. Note that as $r_{1,0}$ increases, however, it is observed via simulation that $q_{max,1}$ and $q_{max,2}$ also increase slightly.

4.2.2 Minimum Vertical Travel

The second scheme involves minimizing the total vertical departure of C from h_0, i.e., $\min\left(q_{max,1} + q_{max,2}\right)$.

Defining D as $D = q_{max,1} + q_{max,2}$, and using Eqn.(4.5), the following is obtained:

$$D = 1.5R + 2R\sin(120^\circ - \theta_0)\,[1 - 2\sin\theta_0] \tag{4.8}$$

Using Eqn.(3.2) and taking the derivative of D with respect to θ_0 obtains:

$$\begin{aligned} \tfrac{\partial D}{\partial \theta_0} &= 4\cos\theta_0 \tan(120^\circ - \theta_0)\sin(120^\circ - \theta_0) - 1.5 = 0 \\ \Rightarrow\ \theta_0 &= 68.08^\circ \end{aligned} \tag{4.9}$$

Therefore, $\min\left(q_{max,1} + q_{max,2}\right)$ occurs at $\theta_0 = 68.08^\circ$ and is independent of the choice of $r_{1,0}$.

4.3 Energy Based

4.3.1 Minimize Energy Consumption

The energy based scheme is built on the principal of minimizing the energy consumption for the completion of one cycle of both phases, i.e. min$\{$Phase I energy required + Phase II energy required + Energy losses in between phases$\}$. To minimize, the parameter θ_{tip} is optimized. The major drawback is that the previous assumption of $h = h_0$ for all phase transitions is obliterated. It would require an additional robustness in the control scheme for the robot to constantly choose new optimal initial conditions. For this reason, the author does not thoroughly investigate this optimization scheme until the overall concept of alternating between Phases I and II is proved ideal.

Chapter 5

Dynamic Analysis

After analyzing the kinematics of LAD in Chapters 3 and 4, the dynamics of both Phases I and II is studied. The motion in Phase I is governed by the constraint equations given in Eqns.(3.1) and (3.3). The dynamic equations during this phase will nevertheless be useful for estimation of linear actuation forces, and required friction coefficients, which could be used as a design tool. For Phase II, although there exists a dynamic EOM for point C, it is still useful to study the dynamics more thoroughly to obtain the required braking force during the free fall.

5.1 Lagrange Equation

A dynamic model was derived here via the Lagrange Equation, erroneously neglecting the kinematic constraints, only to find that the differential equations for the r_1 and θ states were inconsistent with the second derivative of the kinematic constraint Eqn.(3.1). Since Phase I contains differential constraints between the state variables, it is necessary to incorporate them in a more general form of the Euler-Lagrange Equation found in [33] and [21]:

$$\frac{d}{dt}\left(\frac{\partial L}{\partial \dot{q}^i}\right) - \frac{\partial L}{\partial q^i} + \lambda_j \omega_i^j - \tau_i = 0 \tag{5.1}$$

where non-holonomic constraints take the form $\omega^j(q)\dot{q} = 0, j = 1, ..., n_c$ where n_c is the number of constraints, λ_j are the Lagrange multipliers associated with the constraints, and τ_i are the generalized external forces acting on the system.

This approach is both interminable and may not provide all of the desired forces. For a specific application, however, having dynamic equations of motion for point C without any intermediate variables could prove useful in optimizing the controls. An alternative to deriving this may be performing an experimental FFT on the appropriate data and approximate the dynamic equations of motion for point C statistically, and perhaps even more accurately since it will account for all of the subtle real-world nonlinearities.

5.2 Newtonian Approach Assuming Rigid Bodies

5.2.1 Phase One

The author derives the dynamic equations using a Newtonian approach, with relevant free body diagrams for Phase I shown in Figure 5.1. In the past the core was assumed to be a point, and this proved insufficient to obtain accurate motor forces of legs 1 and 2; hence, we assume the core and legs to be rigid bodies as follows:

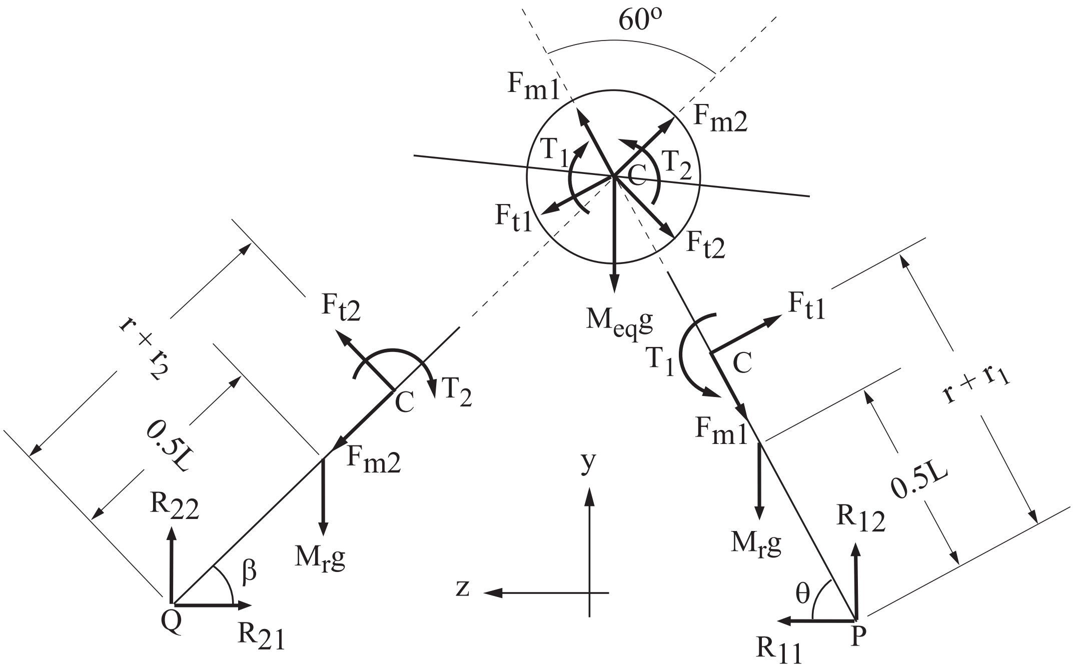

Figure 5.1: Applied and constraint forces - Phase I

In Figure 5.1, F_{m1} and F_{m2} represent the linear actuation forces demonstrated previously in Figure 2.2b, F_{t1} and F_{t2} represent the reaction forces tangential to the rotation of the legs, and T_1 and T_2 represent the reaction torques. To arrive at this force model the author compares the core-leg system to that of a cantilever beam system, where the core is analogous to the wall and the legs are analogous to loaded beams. The key difference being that in LAD the beams can translate in and out of the wall influencing the values of the axial forces accordingly. The rest of the forces in Figure 5.1 are self-explanatory, i.e. $M_{eq}g$, M_rg, R_{11}, R_{12}, R_{21}, and R_{22}. The dynamic equations of motion for the circular core, leg 1 (i.e. PC), and leg 2 (i.e. QC), from Newton's Laws of Motion are

$$\begin{aligned}
M_{eq}\ddot{y}_c &= F_{m1}\sin\theta + F_{m2}\sin\beta - F_{t1}\cos\theta - F_{t2}\cos\beta - M_{eq}g \\
M_{eq}\ddot{z}_c &= F_{m1}\cos\theta - F_{m2}\cos\beta + F_{t1}\sin\theta - F_{t2}\sin\beta \\
I_{eq}\ddot{\theta} &= T_1 - T_2
\end{aligned} \tag{5.2}$$

$$\begin{aligned}
M_r\ddot{y}_{r,1} &= -F_{m1}\sin\theta + F_{t1}\cos\theta + R_{12} - M_rg \\
M_r\ddot{z}_{r,1} &= -F_{m1}\cos\theta - F_{t1}\sin\theta + R_{11} \\
I_{r,P}\ddot{\theta} &= F_{t1}(r + r_1) - T_1 - (M_rgL/2)\cos\theta
\end{aligned} \tag{5.3}$$

and

$$\begin{aligned}
M_r\ddot{y}_{r,2} &= -F_{m2}\sin\beta + F_{t2}\cos\beta + R_{22} - M_rg \\
M_r\ddot{z}_{r,2} &= F_{m2}\cos\beta + F_{t2}\sin\beta - R_{21} \\
I_{r,Q}\ddot{\beta} &= F_{t2}(r + r_2) - T_2 - (M_rgL/2)\cos\beta
\end{aligned} \tag{5.4}$$

where M_{eq} is the mass of the core and leg 3 combined as shown in Figure 2.2a, i.e. $M_{eq} = M_d + M_r$, $I_{eq} = 1/2M_{eq}r^2$, and assuming the legs to be rods of length L, $I_{r,P} = I_{r,Q} = 1/3M_rL^2$.

The coordinates of the center of the core and the midpoints of legs 1 and 2 are (y_c, z_c), $(y_{r,1}, z_{r,1})$ and $(y_{r,2}, z_{r,2})$ respectively. The following relationships are established from geometry with point P as the origin:

$$\beta = 120^\circ - \theta \;\Rightarrow\; \dot{\beta} = -\dot{\theta} \;\Rightarrow\; \ddot{\beta} = -\ddot{\theta}$$

$$\begin{aligned}
\ddot{y}_c &= \ddot{r}_1 \sin\theta + 2\dot{r}_1\dot{\theta}\cos\theta + (r + r_1)\left[\cos\theta\ddot{\theta} - \sin\theta\dot{\theta}^2\right] \\
\ddot{z}_c &= \ddot{r}_1 \cos\theta - 2\dot{r}_1\dot{\theta}\sin\theta - (r + r_1)\left[\sin\theta\ddot{\theta} + \cos\theta\dot{\theta}^2\right] \\
\ddot{y}_{r,1} &= (L/2)\cos\theta\ddot{\theta} - (L/2)\sin\theta\dot{\theta}^2 \\
\ddot{z}_{r,1} &= -(L/2)\sin\theta\ddot{\theta} - (L/2)\cos\theta\dot{\theta}^2 \\
\ddot{y}_{r,2} &= (L/2)\cos\beta\ddot{\beta} - (L/2)\sin\beta\dot{\beta}^2 \\
\ddot{z}_{r,2} &= (L/2)\sin\beta\ddot{\beta} + (L/2)\cos\beta\dot{\beta}^2
\end{aligned} \tag{5.5}$$

Assuming the legs have no inertia, then $M_r = I_{r,P} = I_{r,Q} = 0 \;\Rightarrow\; M_{eq} = M_d$ and $I_{eq} = I_c$. Note that there are 10 unknown forces and only 9 equations, hence their solution is indeterminate. A method for solving them is discussed in Section 5.3.

5.2.2 Phase Two

As in Phase I, it is important to determine the constraint forces to estimate the required coefficients of friction and the necessary actuator force to maintain the rigid body configuration. In Phase II the robot undergoes pure rotation about point Q. LAD's design has no relative motion between the core and leg 2 and thus the motion occurs in a rigid body mode. Similar to Phase I, in the past the core was assumed to be a point, but by assuming rigid bodies the author obtains a more accurate motor force of leg 2. The free body diagrams are identical to that of Phase I in Figure 5.1, except in viewing leg 1 as though it is part of the cores body, thus, the equations of motion, by eliminating leg 1 terms in Eqn.(5.2), can be represented as follows

$$\begin{aligned}
M_{eq}\ddot{y}_c &= F_{m2}\sin\beta - F_{t2}\cos\beta - M_{eq}g \\
M_{eq}\ddot{z}_c &= -F_{m2}\cos\beta - F_{t2}\sin\beta \\
I_{eq}\ddot{\beta} &= T_2
\end{aligned} \tag{5.6}$$

and the equations for the pivoting leg are identical to those for leg 2 in Phase I, i.e. (5.4). The value for M_{eq} in Phase II can be approximated as $M_{eq} = M_d + 2M_r$, and if leg 1 retracts toward the core then the disk assumption is still reasonable and $I_{eq} = 1/2M_{eq}r^2$.

In Phase II, from origin P, $y_c = (r + r_{1,0}) \sin\beta$ and $z_c = a - (r + r_{1,0}) \cos\beta$, yielding

$$\begin{aligned} \ddot{y}_c &= (r + r_{1,0}) \left[\cos\beta\ddot{\beta} - \sin\beta\dot{\beta}^2\right] \\ \ddot{z}_c &= (r + r_{1,0}) \left[\sin\beta\ddot{\beta} + \cos\beta\dot{\beta}^2\right] \end{aligned} \tag{5.7}$$

and $\ddot{y}_{r,2}$, $\ddot{z}_{r,2}$ remain the same as in Phase I, i.e. Eqn.(5.5). Again, assuming no leg inertia the results are identical to that of Phase I. Note that there are 5 unknown forces and yet 6 equations, hence the system appears to be over constrained. A method for solving these equations is discussed in Section 5.4.

5.3 Solving Phase One Equations

The key idea for Phase I is that it is being controlled. The author actuates leg 1 with a desired reference speed trajectory, $\dot{r}_1$, discussed further in Sections 6.2 and 7.1, which in turn provides r_1 and $\ddot{r}_1$. The remaining kinematic variables θ, $\dot{\theta}$, and $\ddot{\theta}$ are obtained from the kinematic constraints from Eqns.(3.1) and (3.3).

The extra force variable is handled by creating an equation to minimize the norm of the actuator forces. In the end this provides the minimum force requirements for actuator design. Begin by rearranging and substituting Eqns.(5.2), (5.3), and (5.4) to obtain a relationship of F_{m1} and F_{m2} from the top equation in Eqn.(5.2), i.e. $M_{eq}\ddot{y}_C$, in the following form

$$F_{m2} = AF_{m1} + B \tag{5.8}$$

where A and B are functions of the known kinematic variables:

$$\begin{aligned} A &= \frac{0.5r - 0.5r_1 + r_2}{0.5r + r_1 - 0.5r_2} \\ B &= \frac{D + E + F + G}{0.5r + r_1 - 0.5r_2} \end{aligned} \tag{5.9}$$

and D, E, F, and G are defined as follows:

$$\begin{aligned} D &= \sqrt{3}/2\left[I_{eq}\ddot{\theta} + I_{r,P}\ddot{\theta} - I_{r,P}\ddot{\beta}\right] \\ E &= \sqrt{3}/4 M_r g L\left[\cos\theta - \cos\beta\right] \\ F &= M_{eq}(r+r_1)\left[g\sin\beta - \ddot{z}_c\cos\beta + \ddot{y}_c\sin\beta\right] \\ G &= -M_{eq}(r+r_2)\left[g\sin\theta + \ddot{z}_c\cos\theta + \ddot{y}_c\sin\theta\right] \end{aligned} \tag{5.10}$$

with r_2 expressed previously by Eqn.(3.5). The line Eqn.(5.8) can be represented by Figure 5.2 as follows

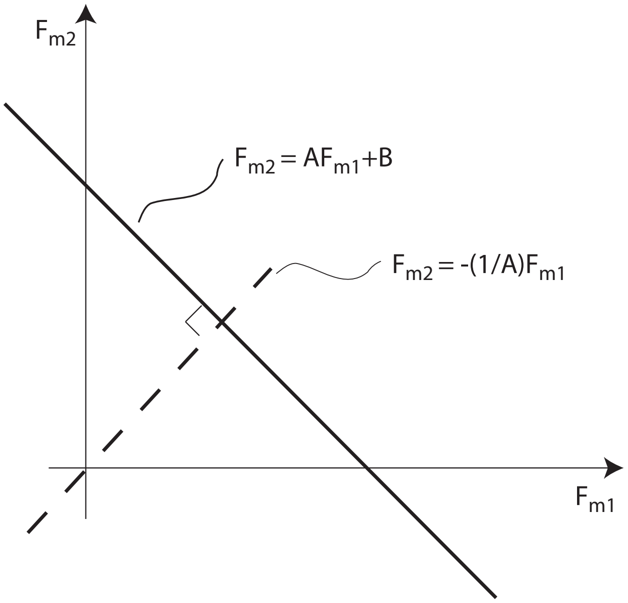

Figure 5.2: Minimization of actuator forces

The dashed line is created as a new equation, which intersects the line at the minimum possible distance from the origin, effectively minimizing the norm of the actuator forces $||F_m|| = \sqrt{F_{m1}^2 + F_{m2}^2}$. The dashed line is in fact perpendicular, which defines its slope as the negative reciprocal of the solid line's slope. Thus, the new dynamic equation of motion, which is in essence a constraint on the actuator forces, is as follows

$$F_{m2} = -(1/A)F_{m1} \tag{5.11}$$

The constraint equation allows the Phase I system of equations to be solved with matrices.

To obtain the actuator forces more directly, however, solve Eqns.(5.8) and (5.11) yielding

$$\begin{aligned} F_{m1} &= \tfrac{-AB}{A^2+1} \\ F_{m2} &= \tfrac{B}{A^2+1} \end{aligned} \tag{5.12}$$

where A and B are defined by Eqns.(5.9) and (5.10).

To calculate the necessary coefficients of friction to prevent slip for legs 1 and 2, the author assumes Coulomb friction:

$$\begin{aligned} \mu_1 &\geq R_{11}/R_{12} \\ \mu_2 &\geq R_{21}/R_{22} \end{aligned} \tag{5.13}$$

5.4 Solving Phase Two Equations

The key idea for Phase II is that since it is uncontrolled, the kinematic variable β becomes an unknown, balancing the Phase II system of equations.

It is important to observe, however, that the system model for Phase II can be derived without any intermediate variables, by rearranging and substituting Eqns.(5.6) and (5.4). Begin with the top equation, i.e. $M_{eq}\ddot{y}_c$, from Eqn.(5.6). The end result is that this equation takes a new form which is quite recognizable:

$$\left[I_{eq} + M_{eq}(r + r_{1,0})^2 + I_{r,P}\right]\ddot{\beta} + \left[M_{eq}g(r + r_{1,0}) + M_r gL/2\right]\cos\beta = 0 \tag{5.14}$$

where $M_{eq} = M_d + 2M_r$, $I_{eq} = 1/2M_{eq}r^2$, and $I_{r,P} = 1/3M_rL^2$. Assuming the legs to be massless changes the equation of motion for the core into the same form as the Lagrangian system model for Phase II, i.e. Eqn.(3.7), providing a pseudo-check for the rigid body Newtonian models. The remaining 5 equations/unknowns can be solved with matrices to obtain the required braking force, or $F_B = (F_{m2}$ during Ph.2).

To calculate the necessary coefficient of friction to prevent slip for leg 2, the author again assumes Coulomb friction:

$$\mu_3 \geq R_{21}/R_{22} \tag{5.15}$$

Chapter 6

Control Theory

6.1 Upper and Lower Level Controls Philosophy

The upper level controls of LAD ideally consist of establishing the initial conditions, producing the desired $v_{C,ref}$, $\dot{r}_{1,ref}$, and $\dot{r}_{2,ref}$, and performing maneuvers based on human interface or reactions to stimuli. To accomplish the upper level controls tasks the following variables must be sensed: r_1, $\dot{r_1}$, r_2, $\dot{r_2}$ r_3,$\dot{r_3}$, θ, and $\dot{\theta}$. It is possible that more variables will require sensing, especially for appropriate reactions to stimuli or disturbances. The lower level controls are simply to produce an actual $\dot{r}_1$ that minimizes rise time, time to peak, overshoot, settling time, and disturbances to the desired $\dot{r}_{1,ref}$, and for specific applications the design requirements are subject to change. Similarly, the author strives for an actual $\dot{r}_2$ that mimics $\dot{r}_{2,ref}$.

6.2 Upper Level Control Theory

6.2.1 No Slip

The author assumes no slip between the feet and the ground during Phase I. Another assumption is that ϵ, which is defined as the angle between each pair of legs, is exactly $60°$.

As mentioned in Eqn.(5.5):

$$\beta = 2\epsilon - \theta = 120^\circ - \theta \tag{6.1}$$

$$\dot{\beta} = -\dot{\theta} \tag{6.2}$$

$$\ddot{\beta} = -\ddot{\theta} \tag{6.3}$$

To have no slip is to say that the parameter a is a constant. Recall Eqn.(3.1), then combine it with the result $a = \sqrt{3}R$ from Eqn.(3.2), and the relationships discussed above as follows

$$(r + r_1) = a\left(\frac{\sin\beta}{\sin 60^\circ}\right) \tag{6.4}$$

Note that if a were an unknown variable, sensing a or $\dot{a}$ would be difficult, and this constraint equation and its derivatives would contain too many unknowns to be of any practical use, and the path trajectory of C is no longer defined as a circular arc with radius R. With a as a known constant, however, this equation, its derivatives from Eqn.(3.3), Eqns.(3.5) and (3.6) or (6.7) for r_2, and Eqn.(3.13) for v_C, represent the basis of the no slip upper level control scheme. The main advantage of the no slip scheme is that θ and $\dot{\theta}$ do not require sensing.

6.2.2 Slip

In this subsection the author does not assume no slip. Another way to perceive the concept of a is to derive it directly from Figure 3.1 using basic trigonometry as follows

$$a = (r + r_1)\cos\theta + (r + r_2)cos\beta \tag{6.5}$$

Take the derivative of a treating it as a time-dependent variable

$$\dot{a} = \dot{r}_1\cos\theta - (r + r_1)\sin\theta\dot{\theta} - (r + r_2)\cos\beta\dot{\beta} + \dot{r}_2\cos\beta$$

Recall from Eqn.(3.4) $h = (r + r_2)\sin\beta = (r + r_1)\sin\theta$, and Eqn.(6.2) and substitute them into above equation eliminating the two middle terms:

$$\dot{a} = \dot{r}_1\cos\theta + \dot{r}_2\cos\beta \tag{6.6}$$

By assuming no slip $\dot{a} = 0$ and the above equation can be written as

$$\dot{r}_2 = -\left(\frac{\cos\theta}{\cos\beta}\right)\dot{r}_1 \tag{6.7}$$

which is an alternate, more direct way to express $\dot{r}_2$ than Eqn.(3.6) above. To check this alternate expression the author first develops a relationship for r_2 derived similarly and analogous to Eqn.(3.1), and take a time derivative to obtain $\dot{r}_2$:

$$\begin{aligned} r_2 + r &= (2a/\sqrt{3})\sin\theta & (6.8)\\ \dot{r}_2 &= (2a/\sqrt{3})\dot{\theta}\cos\theta & (6.9)\end{aligned}$$

Now by substituting the expression for $\dot{r}_1$, i.e. Eqn.(3.3), into Eqn.(6.7) it is clear that an identical expression to Eqn.(6.9) is obtained, providing a check for Eqn.(6.7).

The difference between slip and no slip is made clear by perceiving the system LAD through the lens of variable a, and, what can potentially allow a slip control scheme is the following. With slip allowed, h will be time-dependent like a, but there are two expressions for h, which provide a relationship between r_1 and r_2 despite the changing path trajectory defined by R. Take the derivative of Eqn.(3.4):

$$\dot{r}_1\sin\theta + (r + r_1)\dot{\theta}\cos\theta = \dot{r}_2\sin\beta + (r + r_2)\dot{\beta}\cos\beta \tag{6.10}$$

and this expression equals $\dot{h}$. Eqns.(3.4) and (6.10) for h and $\dot{h}$, respectively, represent the fundamentals for the upper level control scheme allowing slip. Combining these fundamental equations obtains a constraint for allowing slip:

$$\dot{\theta} = \frac{\dot{r}_2\sin\beta - \dot{r}_1\sin\theta}{(r + r_1)\cos\theta + (r + r_2)\cos\beta} \tag{6.11}$$

For forward motion the author demands $\dot{\theta} < 0$. Observing that for $50^\circ \leq \beta \leq 70^\circ$ the denominator of the above equation is always positive, the constraint becomes

$$\dot{r}_2 < \left(\frac{\sin\theta}{\sin\beta}\right)\dot{r}_1 \tag{6.12}$$

note that implementing this constraint to achieve a control scheme which allows slip, if it is feasible, will require care since the path trajectory defined by R is no longer constant.

6.3 Reference Velocities

To complete the upper level control analysis, for this thesis, no slip is assumed. A logarithmic growth of v_C is desired as it approaches its target velocity, $v_{C,T}$ to achieve a smooth motion, as shown in Figure 6.1.

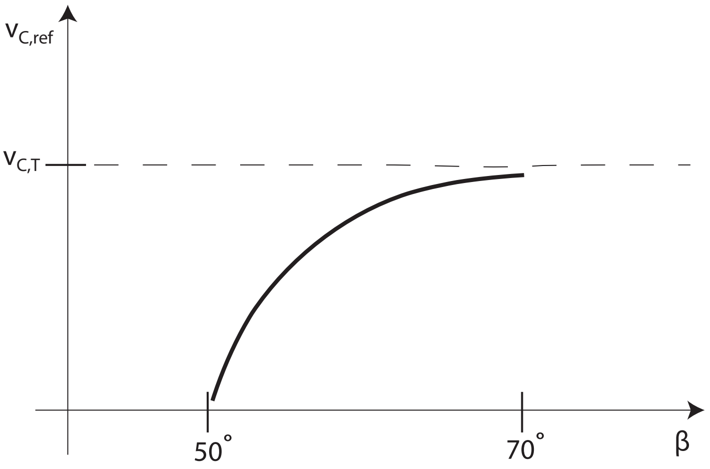

Figure 6.1: Desired reference velocity for C

Note the expression for this curve is

$$v_{C,ref} = v_{C,T} + (v_C(t=0) - v_{C,T})e^{-\lambda(\beta-\beta_0)} \tag{6.13}$$

where λ is a constant that can be tuned, and $v_{C,T}$ is the target velocity for the transition from Phase I to Phase II, which is expressed as v_{C1-} in Eqn.(3.17). $r_{1,ref}$ and $r_{2,ref}$ are obtained by combining the basis equations for upper level control at the end of the No Slip subsection of Section 6.2:

$$\dot{r}_{1,ref} = \sqrt{\frac{4R^2 v_{C,ref}^2 \cos^2\beta}{4R^2\cos^2\beta + (r+r_1)^2}} \tag{6.14}$$

$$\dot{r}_{2,ref} = -\left(\frac{\cos\theta}{\cos\beta}\right)\dot{r}_{1,ref} \tag{6.15}$$

Thus, the upper level controls, after implementation, achieve initial conditions and reference velocities for legs 1 and 2.

6.4 Lower Level PID Compensation

The following block diagram shows where the lower level controls fit into the overall picture, however, it may need modifications upon fully implementing the no slip control scheme:

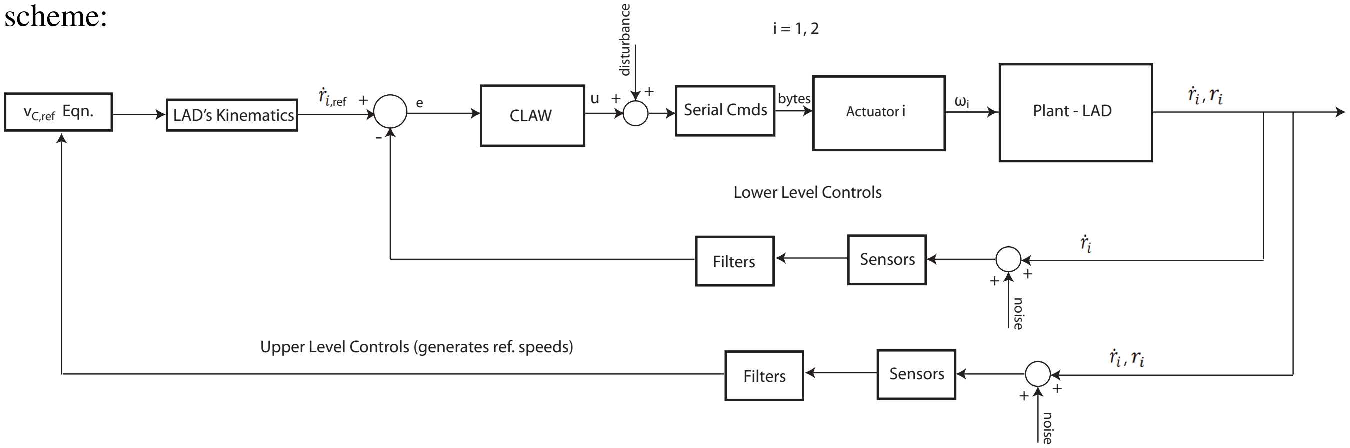

Figure 6.2: Controls block diagram

The CLAW in the diagram above may be represented as a PID compensator. PID compensation is as follows in the Laplace Domain

$$\left[\frac{K_d s^2 + K_p s + K_i}{s}\right] E(s) = U(s) \tag{6.16}$$

where K_p is the proportional gain, K_i is the integral gain, and K_d is the derivative gain, $E(s)$ is the error e in the Laplace Domain, and $U(s)$ is the control effort u in the Laplace Domain. u is defined above and e is as follows in the above block diagram

$$e_i = \dot{r}_{i,ref} - \dot{r}_i \tag{6.17}$$

where $i = 1, 2$ corresponding to leg i, and $\dot{r}_i$ includes noise and filtering.

6.5 Lower Level Nonlinear Control Theory

As the control theory and implementation is expanded, nonlinear control may prove necessary to meet the required precision for the speeds of legs 1 and 2, i.e. $\dot{r}_1$ and $\dot{r}_2$. Potential control laws include Sliding Mode and Adaptive Control.

Chapter 7

Simulation

7.1 Explanation of Model

To design the actuators and structural components for LAD, the author develops a Simulink model, which is shown in Appendix B, to provide estimations of F_{m1}, F_{m2}, F_B, and several other parameters discussed in Section 7.3. Simulation results also exist to demonstrate and justify the analysis presented in earlier sections, and gain a sense of the feasibility of LAD. For the simulation, the speed of leg 1 is assumed to equal $\dot{r}_{1,ref}$ and be constant for simplicity, i.e. $\dot{r}_1 = \dot{r}_{1,0} =$ constant. In the implementation, the stress in the system may reduce by driving leg 1 at a speed that resembles a more gradual, logarithmic curve. In the author's early simulations, F_{m1} is obtained by assuming $F_{m2} = 0$, and F_B is obtained by assuming the core is a point and neglecting leg inertia for Phase II. For latter simulations, rigid bodies are assumed, leg inertia is considered, and it is found that F_{m1} reduces considerably when F_{m2} provides support and F_B reduces when the point assumption is lifted. Subtle distinctions are made as results are shown below, however, Phase I is primarily comprised of kinematic constraint Eqns.(3.1), (3.3), supporting Eqns.(3.2), (3.13), (3.16), (3.5), and (6.7), and dynamic models Eqns.(5.2), (5.3), (5.4), and their supporting Eqns.(5.5) and (5.12). Phase II primarily consists of system model Eqn.(5.14), supporting Eqns.(3.14) and (3.16), and dynamic models Eqns.(5.6) and (5.4), and their supporting Eqns.(5.7) and $y_{r,2}$, $z_{r,2}$ from (5.5). Refer to Appendix B for a more detailed explanation of the model, and design and prototype parameters.

7.2 Results Demonstrating Theory and Feasibility

Two sets of simulation results are presented. In the first simulation, shown in Figures 7.1 and 7.3, $\theta_0 = 70°$ and $r_{1,0} = 0.15$m. The simulation is run with the following constants: $r = 0.15$m, $L = 0.6$m, $M_d = 5$kg, and $M_r = 0$. This leads to $\beta_0 = 50°$ and $h = 0.282$m. The author imposes $\dot{r}_{1,0} = 0.25$m/sec, and $\ddot{r}_1 = 0$ during Phase I. The initial conditions for Phase II are computed by the model considering the impulsive losses discussed in Section3.5. Switching from Phase I to II occurs when $\theta = \beta_0$. Thereafter, over the course of Phase II, β varies from θ_0 to $180° - \theta_0$. Transition from Phase II to I occurs when $\beta = 180° - \theta_0$. The motion trajectories and the switching sequence are shown in Figure 7.1 below.

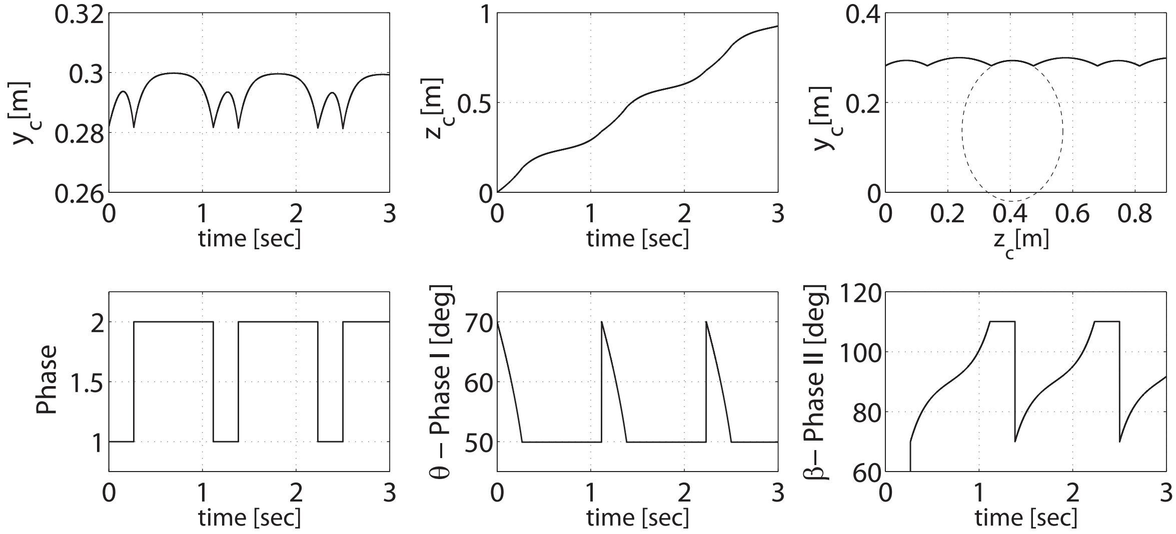

Figure 7.1: Simulation 1: motion trajectories

Note that, in the plots above, during Phase II θ is undefined, and in Phase I β is undefined. The motion trajectory of C, shown in the upper right plot, does indeed follow circular paths demonstrating the correctness of the theory in earlier sections which led to Figure 3.3. This is ensured by creating an oval in Adobe Illustrator, with a height to width ratio (7:5) equal to that of the rise to run ratio of the graph due to scaling, and overlaying it on the Phase I trajectory; without scaling effects the oval is indeed circular. Also, Phase II is already known to follow a circular path since LAD's EOM is identical to a rigid inverted pendulum during this phase. A visual of both phases at $\theta_0 = 70°$, with trajectories demonstrated clearly as circular is shown in Figure 7.2.

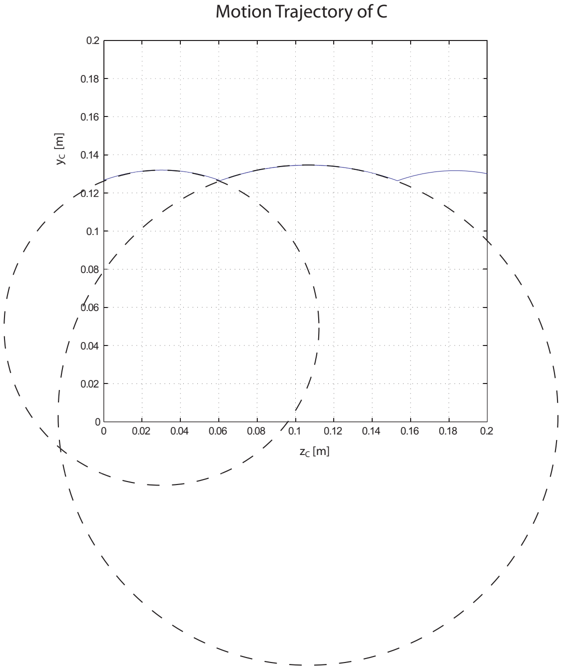

Figure 7.2: Path trajectory of C confirmed by simulation

The corresponding actuator forces and coefficients of friction in Phases I and II are shown in Figure 7.3. These computations are done using the equations discussed at the end of Section 7.1, and Eqns.(5.13) and (5.15) which rely on a Coulomb friction model. There is a particle assumption for the core here, thus neglecting its rotational inertia. This gives unique values for F_{m1} and F_{m2}, which are less than the weight of the core, and required coefficients of friction are found to be less than one. Since actuators can be found which lift the whole weight of the core, and coefficients of friction exist which are greater than one, i.e. aluminum on aluminum, these results show feasibility and justify progressing with more detailed design, testing, and implementation in Sections 7.3, 8.1, and 8.2. In Section 7.3 the author removes the assumptions for the two simulations in this section and computes the actuator forces by a technique discussed in Section 5.3.

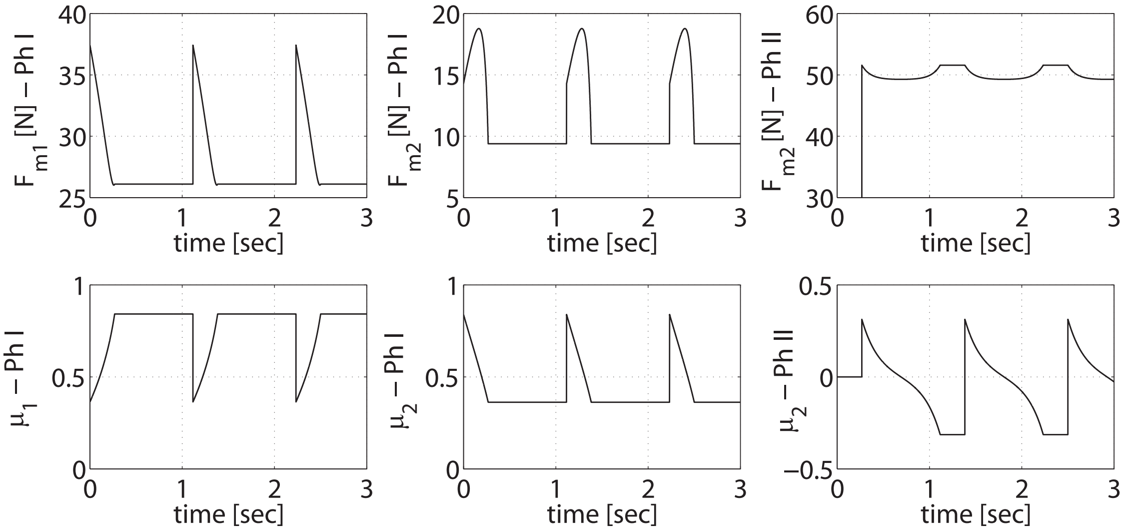

Figure 7.3: Simulation 1: actuator forces and friction coefficients

Note that the change in sign of μ_2 during Phase II, a.k.a. μ_3, is due to a reversal in the direction of friction force of leg 2 as the robot tips about point Q. Also note that F_{m2} during Ph.2, a.k.a. F_B, is significantly large and needs to be considered during actuator design, and may require an additional braking system.

In the second simulation, Figure 7.4, the author shows motion trajectories for $\theta_0 = 80°$. To demonstrate the extreme effects of changing θ_0, the values of $r_{1,0}$, $\dot{r}_{1,0}$, $\ddot{r}_1$ and the constants are left the same as in the first simulation. A noticeable difference between the two simulations is the relative prominence of Phase I and II. Phase II is more prominent in the former as the net tipping angle is $40°$ in the former and $20°$ in the latter. Phase I, however, involves a net rotation of $20°$ in the former and $40°$ in the latter simulation and hence is more prominent in the second simulation.

Comparing the motion trajectory of C in the upper right plots in both simulations, i.e. Figures 7.1 and 7.4, it is clear that for $\theta_0 = 80°$ there is significantly more vertical travel, which is demonstrating a correctness of the theory for optimizing θ_0 in Section 4.2. $\theta_0 = 80°$ does also travel more horizontal distance in the same amount of time due to a shorter Phase II, but for reasons discussed in Section 7.3 the author uses $\theta_0 = 70°$ for the design.

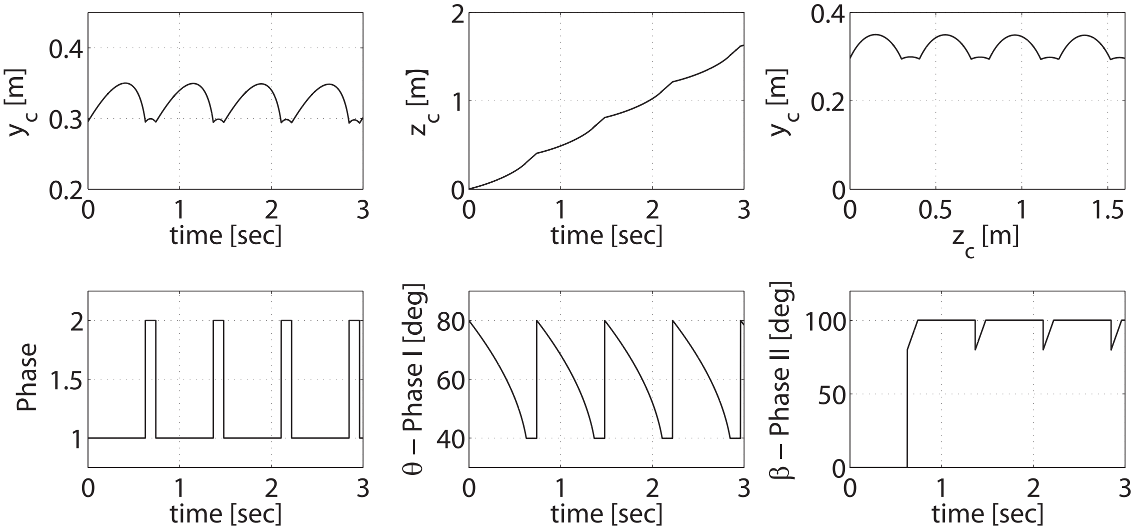

Figure 7.4: Simulation 2: motion trajectories

7.3 Results Aiding in Actuator Design

To forecast design parameters, simple guidelines are used. The simulation is run until a minimum value of $\dot{r}_{1,0}$ to complete Phase II is obtained with an accuracy of two decimal places, thus $\dot{r}_{1,0} = \dot{r}_1 = 0.18$m/sec for $\theta_0 = 70°$. The core radius for the first prototype is chosen to be as small as possible without requiring microfabrication, which, after much research and consideration, elaborated in Section 8.1, is 3 inches or $r = 0.076$m. The length of the legs is chosen to be double the core diameter or $L = 0.305$m to best illustrate the motion regimes without being overweight or cumbersome to manufacture. $r_{1,0} = 0.076$m is chosen to equal the core radius so leg 1 protrudes equally from both sides of the core, again, to illustrate the motion regimes, while avoiding potential fouling. There may be a future case where L and $r_{1,0}$ need optimizing in order to yield a large enough h to clear an obstacle for a specific application. M_d and M_r are chosen conservatively after examining weight specifications for motors on the 3 inch radius scale, and considering the addition of a counter weight for balance, which is detailed in Section 8.2, $M_d = 7$kg and $M_r = 1$kg.

While $\theta_0 = 70°$ is optimal for smooth, mostly horizontal travel, the author has not shown that it is optimal for minimum force and energy expenditure. A simple comparison is made to fully justify the choice of $\theta_0 = 70°$:

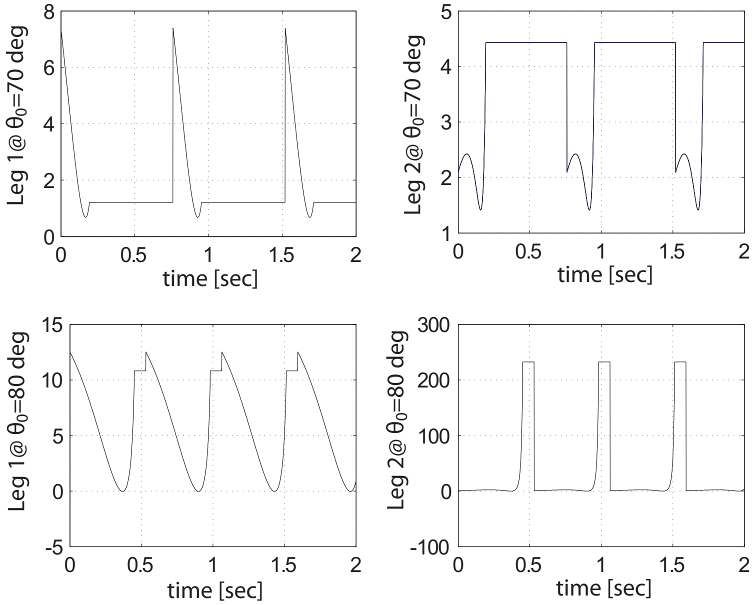

Figure 7.5: Plot: actuator power, Ph.1 [W]

The power calculations in the above figure, for each time step, are simply $(Power) = (Actuator\ Force) \times (Leg\ Speed)$ since the motor forces and leg velocities are always in the same direction. Note that the flat lines are during Phase II. Notice the huge amount of power at $\theta_0 = 80°$ for leg 2 right before the transition to Phase II. This is due to the sharp vertical drop of leg 2, hence the speed and force raise exponentially during this time; see Figure 7.6 for clarification. The area under the curve for $\theta_0 = 80°$ is much larger and thus more total energy is consumed. It is also fairly safe to assume that the energy lost in between phases will be larger for $\theta_0 = 80°$ due to the larger vertical velocity of C. Thus, for $\dot{r}_1 = 0.18$m/sec, $\theta_0 = 70°$ is clearly the correct choice for both smooth travel and minimal power requirements and energy consumption. However, it is important to note that for $\theta_0 = 80°$ roughly 25% more horizontal distance is covered in the same amount of time due to the shorter Phase II. Also, the minimum velocity requirement for leg 1 to complete Phase II is only $1/3$ of $\theta_0 = 70°$, which allows for much slower travel with lower power requirements than $\theta_0 = 70°$, although still not as energy efficient.

Not much has been said about $\theta_0 < 70°$ because it is not practical. Since Phase I is very short compared to Phase II, the minimum speed requirement increases significantly. For instance, when $\theta_0 = 65°$, the requirement is a short burst of $\dot{r}_1 = 0.26$m/sec. This leads to higher power requirements and even though the speed increases it still only covers about 75% of the horizontal distance of $\theta_0 = 70°$ in the same time span due to a longer Phase II. However, since Phase I is shorter it appears that the total energy consumption is slightly less than $\theta_0 = 70°$, but Phase I is characterized by a short, powerful burst whose extreme nature is prone to increasing the energy loss in between phases.

In summary, $\theta_0 = 70°$ is optimal for the standard travel of the first prototype mainly due to the lowest power requirements at faster horizontal travel, low energy consumption, and smooth nature which the author predicts will decrease energy loss during phase transitions.

Next, to design LAD's actuators the author takes into consideration the speed and force requirements of both legs 1 and 2 at $\theta_0 = 70°$ for Phase I, and the braking force required during Phase II. By simulation trial and error the speed requirement for leg 1 is found to peak at the end of Phase I at $\dot{r}_1 = 0.18$m/sec. Holding $\dot{r}_1$ constant at the speed requirement, the author plots $\dot{r}_2$ in Figure 7.6 below to gain insight. Note in Figure 7.6 that there is a

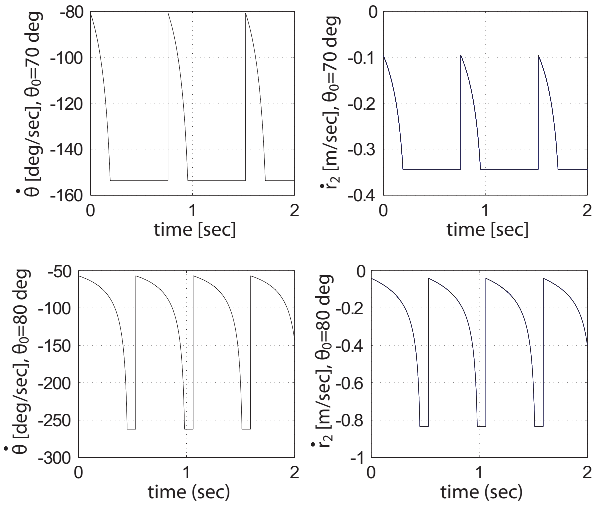

Figure 7.6: Plot: leg 2 vs. leg 1 speed, Ph.1

direct relationship between $\dot{\theta}$ and $\dot{r}_2$ since $\dot{r}_1$ is constant; as $\dot{\theta}$ increases rapidly in magnitude just before the phase transition, $\dot{r}_2$ does the same. For $\theta_0 = 80^\circ$, $\dot{r}_2 = -4.41\dot{r}_1$ as it peaks before the transition to Phase II, and similarly for $\theta_0 = 70^\circ$, $\dot{r}_2 = -1.88\dot{r}_1$ which is evidence that the choice of $\theta_0 = 70^\circ$ will have significantly smaller actuator speed requirements for leg 2. In Figure 7.7 below, with the above parameters the author plots the actuator forces, braking force, and corresponding required coefficients of friction. While

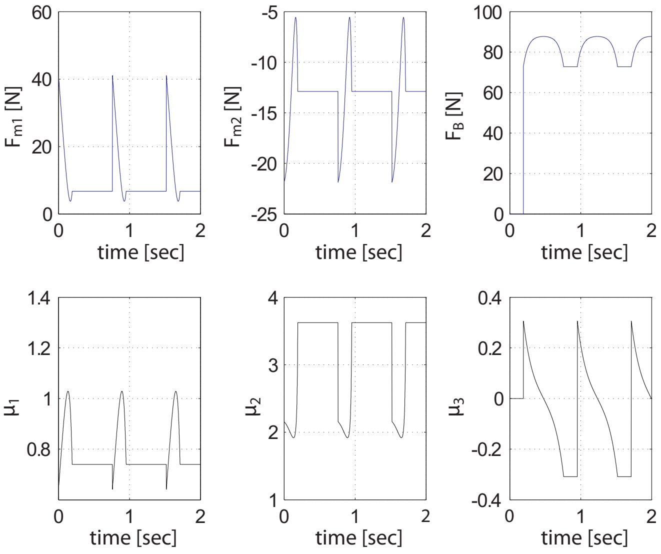

Figure 7.7: Plot: required actuator, brake force, and COF

the required actuator forces are fairly high, particularly the braking force, the actuator requirements are actually minimized. In the past, the author tried lowering these requirements even further by reducing the weight of the core, however, after an extensive motor search no light weight motors were found that could match the force and speed requirements at various lower core weights. More details on verifying feasibility of the design with the available technology selection at the macro scale are found in Section 8.1. Another potential problem are the large COFs. However, since the angle in between legs is fixed, to have slip there needs to be a change in the extension of legs 1, 2, or both. It is possible for the mechanical structure, i.e. $F_{t1}, F_{t2}, T_1,$ and T_2, a robust control scheme with prescribed leg movements, or both, to prevent movement other than that which positions C on the prescribed arc R. It may happen in some cases that both legs slide simultaneously, having the effect of LAD performing its motion regimes on a moving surface. If the mechanical and electrical constraints cannot keep slipping under control, then two other options exist: 1) design a control scheme which allows slipping, which is pursued in Subsection 6.2.2, or 2) only control the actuator for leg 1 and let leg 2 follow along via the mechanical constraint. It is clear from the diagram below that the second option reduces the required COFs for both legs, but the cost is a larger force requirement from the leg 1 actuator.

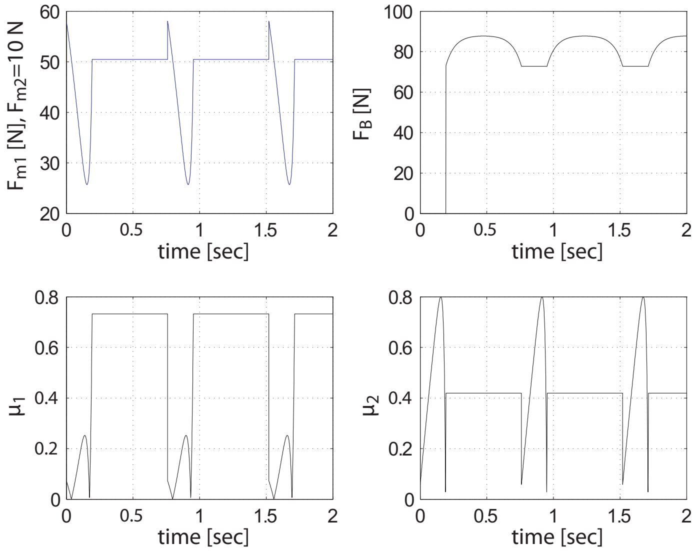

Figure 7.8: Plot: alternate requirements

For the Alternate Actuation Scheme shown in Figure 7.8, the author assumes the resisting friction of leg 2 to be $F_{m2} = 10$N as a worst case, and since the resulting F_{t2} peaks at about 30N as seen in Figure 7.9, the maximum COF between leg 2 and its actuator is around $F_{m2}/F_{t2} = 0.33$; to provide leg 2 with less friction than that is obtainable. Note that F_B remains the same as in Figure 7.7, indicating that the different actuator scheme does not effect Phase II. F_{m1} is approximately 20N higher, but the COFs drop significantly. Even if slipping occurs right before Phase II when the COFs are highest, it will only be brief.

The author's goal is to implement actuators with the lowest power requirements and

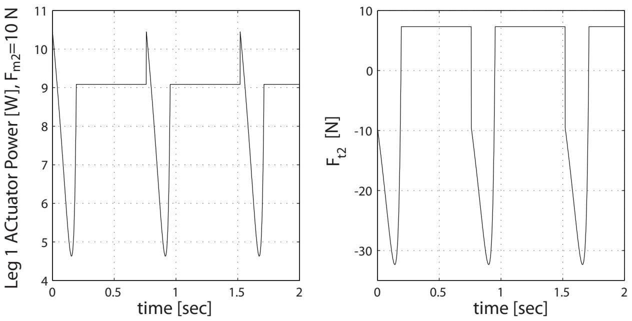

Figure 7.9: Plot: alternate leg 1 power and actuator 2 normal force

energy consumption. After comparing Figures 7.9 and 7.5, observe that actuating both legs is necessary to achieve the lowest power requirements. Therefore, the author strives to implement both leg 1 and leg 2 actuators to achieve the minimized forces found in Figure 7.7 with their corresponding leg speed requirements, while considering for the first prototype that the alternate actuation scheme in Figure 7.8 is easier to implement and has lower COF requirements. To lower power requirements and energy consumption more the author plans to relax the assumption of constant $\dot{r}_1$ and implement a control scheme that has a more gradual acceleration to the required speed.

Some forces resulting from the actuation of legs 1 and 2, that may be useful for selecting materials, are shown on the next page. These forces represent the friction forces and normal forces of both legs contact points with the ground, and the reaction torques and tangential forces between the core and legs 1 and 2. To visualize the forces in their positive directions see Figure 5.1. None of the data is of major concern as long as the leg rods have sufficient support. The author revisits the design concepts and constraints discussed in this section during the prototype design in Section 8.1. Simulation block diagrams and corresponding parameters which supplement the content in Chapter 7 are found in Appendix B.

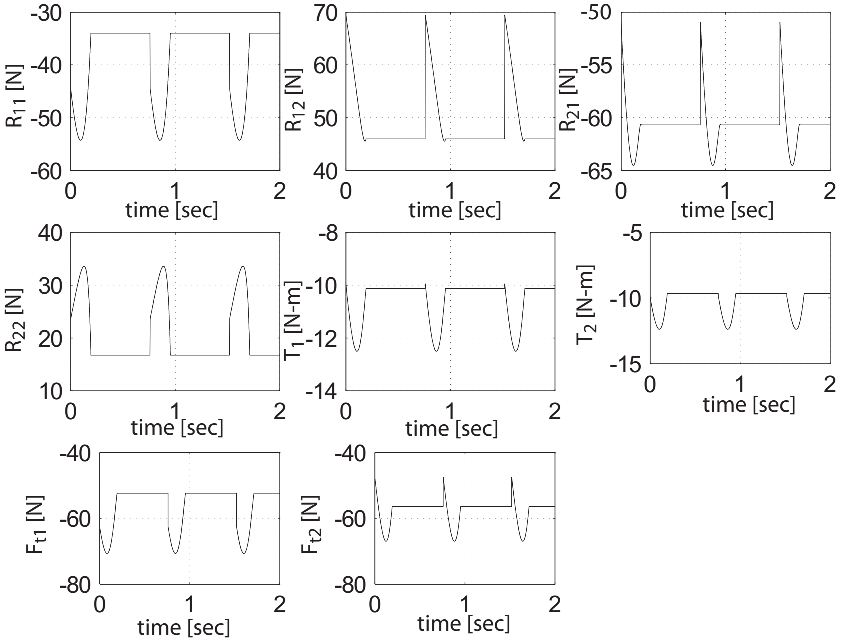

Figure 7.10: Plot: Phase I forces

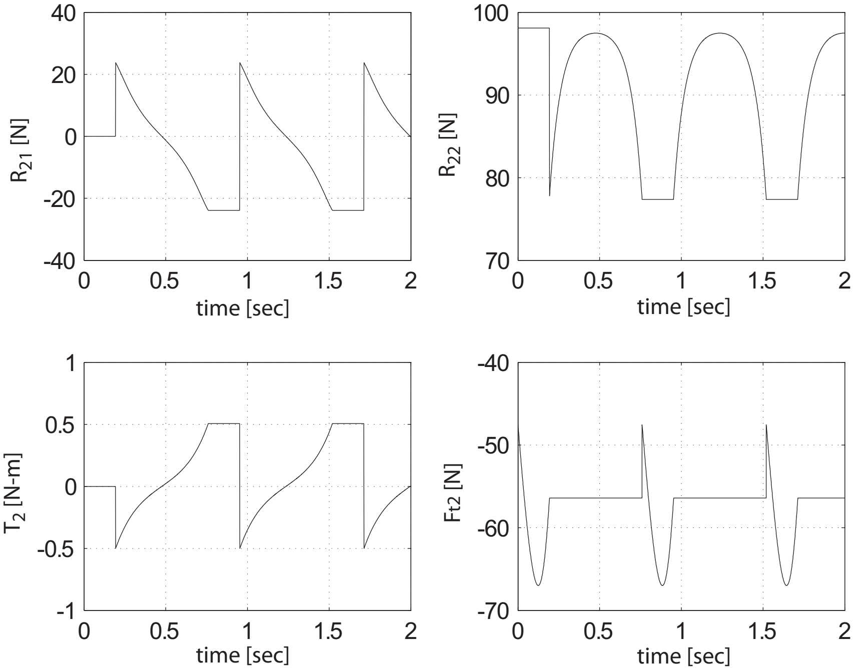

Figure 7.11: Plot: Phase II forces

Chapter 8

Experimentation

8.1 Actuator Selection and Testing

Actuator selection is a practical culmination of the theory and simulation discussed above. The first consideration for actuation of the legs was a relatively new technology, the Linear Motor. However, cost alone eliminates this option as the cheaper models are well over $1000 each and have unnecessarily high precision for the first prototype. To utilize a standard DC Rotary Motor the author implements a Rack and Pinion Assembly as a Drive Train, which is described in Section 8.2.

After examining a broad selection of DC Motor types, using a streamlined technology search discussed in Appendix E, the author chooses a Stepper Motor because of high torque requirements at low speeds with limited space, and the need for a high braking or holding torque during Phase II. Another desirable feature of the Stepper Motor is precise Open-Loop Control, making it a common choice for robotics applications. However, one drawback is the difficulty of implementing Closed Loop Control relative to motors such as DC Servo Motors, which is further discussed in Section 8.3. The first Stepper Motor considered for purchase was TPP34-793A50-1100-X from Electrocraft, which was selected for a core radius of $r = 6$in. In an effort to reduce size and weight, the author finds a smaller radius of $r = 3$in to be feasible with Stepper Motor 23H218D10B-D from Portescap, a branch of Danahar Motion focusing on miniature motors. A detailed explanation of the motor selection method and key results are found in Subsection 8.1.1. The criteria for motor selection are the torque-speed curve, braking or holding torque, size, weight, and cost. Since a braking mechanism and gearbox increase the size of motors significantly, a Stepper Motor is selected to have sufficient holding torque and moving torque for providing the actuator force and speed requirements at a compact size and low weight.

After testing the initial Portescap Stepper Motor selection on an experimental test bed, with test results recorded below, and executing the motor selection method with various new parameter choices, the author arrives at a final selection for the first prototype: *Portescap Stepper Motor 23H118D20B-D*. Test results of the final selection on the test bed in Figure 8.1 are found below in Subsection 8.1.2.

The author designs an experimental test bed to replicate the mechanics of the LAD prototype, taking into account the nonlinearities of the rack and pinion such as backlash and the $14.5°$ pressure angle. Its purpose is to verify torque-speed curve product claims, test performance in a scenario that mimics the actual dynamics of the prototype, and to calibrate sensors and design filters as discussed in Subsection 8.3.2. The test bed is essentially the prototype design for the Rack and Pinion Assembly in conjunction with a simple mass-pulley system, as seen in Figure 8.1 on the next page.

An explanation of the selection of a 1 in. pitch diameter pinion is found in Section 8.1.1, a detailed design of the Rack and Pinion Assembly is found in Section 8.2, and the Potentiometer selection is explained in Subsection 8.3.2. Methodologies for testing the steppers are found with their results in Subsection 8.1.2. Detailed explanations of the stepper and dSPACE protocol used during testing are found in Subsection 8.3.1.

8.1.1 Motor Selection Method

To identify an actuator that is feasible for the prototype, the author designs with parameters explained in Section 7.3, and the following are approximate worst case requirements from Figures 7.7 and 7.6: 50N at 0.18 m/sec, 25N at 0.34 m/sec, and 100N braking force. These requirements must be met for each actuator since the role of each leg changes as

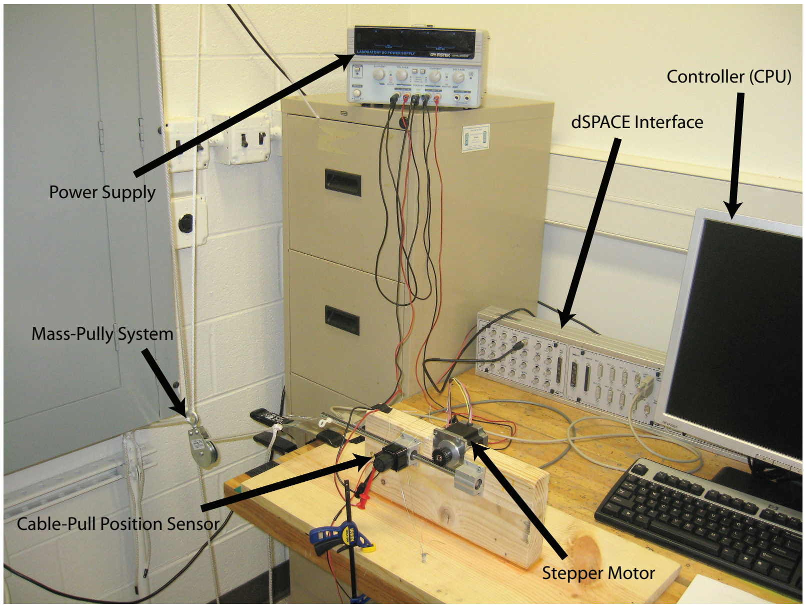

Figure 8.1: Experimental test bed setup

the robot moves forward. Note that these requirements can be lessened by executing the controls properly, specifically accelerating leg 1 more gradually to the required tipping speed. Also note, to accomplish the alternate actuation method shown in Figure 7.8, which consists of only actuating leg 1, the worst case force requirement is around 65N, approximately 33.33% larger than the 50N leg 1 requirement above. The basic actuator concept is visualized and communicated to vendors with the following sketch:

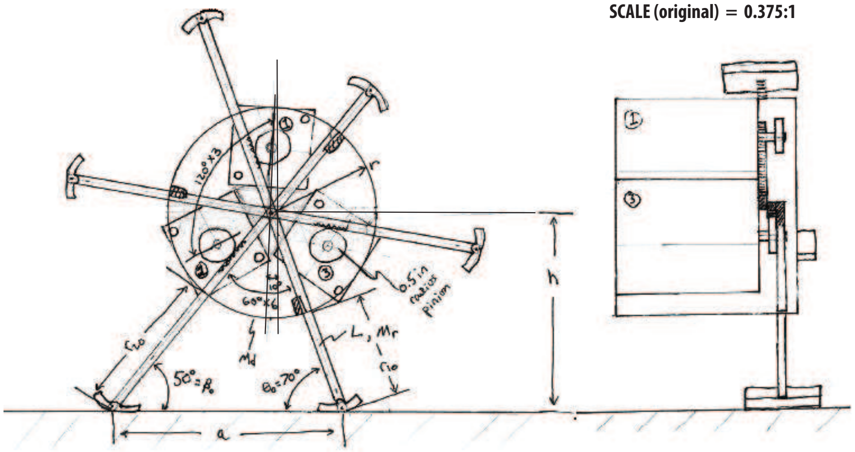

Figure 8.2: LAD actuator concept visual

Note that this visual is to scale, but the scale is 3:8 in the original hand drawing and not necessarily the above figure. The theory behind the actuator design begins with $(Power) = (Force) \cdot (Velocity) = (Torque) \cdot (Angular\ Velocity)$. The dot products are treated as multiplication since the vectors are in the same direction, and the concern is only with magnitudes for motor selection. For a rack and pinion assembly with a pinion radius of ρ, assuming ideal gear meshing and neglecting backlash and the pressure angle of $14.5°$:

$$\tau_i = F_{mi}\rho \tag{8.1}$$

$$\omega_i = \dot{r}_i/\rho \tag{8.2}$$

$$P_{req,i} = P_i/\zeta = F_{mi}\dot{r}_i/\zeta \tag{8.3}$$

where τ_i is the output torque of the motor associated with leg i, where $i = 1, 2$, ω_i is the angular speed, $P_{req,i}$ is the power required for motor i from the battery or power supply, P_i is the output power, and ζ is the efficiency of motor i. The above assumptions for these equations are offset by the slight overestimations of the actuator force requirements in the first paragraph, and to be conservative the author designs for an approximate factor of safety of 2. If power is transmitted through a speed reducer, with a reduction ratio of $\mathcal{N} : 1$, before reaching the rack and pinion, then the above formulae become

$$\tau_i = \frac{F_{mi}\rho}{\eta\mathcal{N}} \tag{8.4}$$

$$\omega_i = \dot{r}_i\mathcal{N}/\rho \tag{8.5}$$

$$P_{req,i} = \frac{P_i}{\zeta} = \frac{F_{mi}\dot{r}_i}{\eta\zeta} \tag{8.6}$$

where η is the efficiency of the speed reducer.

The author streamlines the selection process, making it possible to change any parameter, see its affect instantaneously, and make quick motor comparisons leading to educated decisions. The above equations are implemented in Matlab, and the resulting code is found in Appendix C. In this way the author decides to have a 0.5 in. radius pinion, i.e. $\rho = 0.0127$m, to achieve a balance between torque and speed that works well with steppers, and to bypass a speed reducer, thereby avoiding the waste of space and efficiency that would otherwise result.

The final results from the motor selection method are marked as red crosses in Figure 8.4 below. Using the 2.0A per phase curve it is clear that the factor of safety is approximately 2. The estimated holding torque required is 1.27N-m, which matches exactly to the typical passive holding torque on the data sheet from http://www.portescap.com/ of the stepper of choice. Holding torque can potentially increase, if needed, by using the active holding torque of the motor, discussed further in Subsection 8.1.2 below, or by switching the motor into over drive.

8.1.2 Test Results

Actuator testing is executed with 5lb, 10lb, and 20lb weights at various speeds. These weights, approximately 22.5N, 45N, and 90N, represent the desired maximum actuator force requirements, $F_{m2}, F_{m1},$ and F_B, respectively, from simulation results of Figure 7.7. With the alternative scheme of deactivating the leg 2 actuator, the F_{m1} requirement is approximately 60N, or 33.33% larger than the optimal requirement.

For the initial Portescap Stepper, 23H218D10B-D, the torque-speed curve from the data sheet provided by http://www.portescap.com/ is as follows:

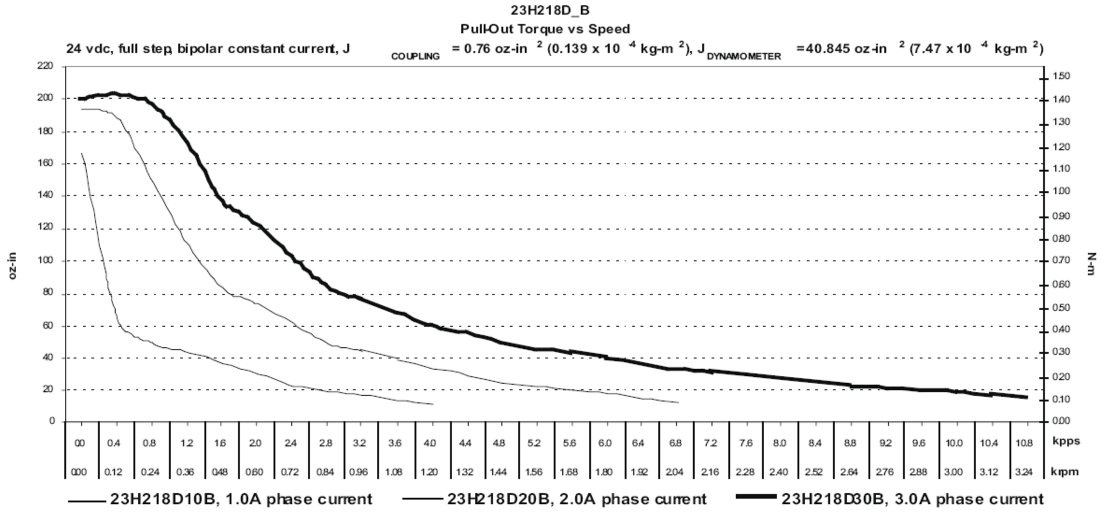

Figure 8.3: Portescap Stepper Torque-Speed Curve - 2 Stack [http://www.portescap.com/]

where the maximum holding torque while energizing both stepper phases is reported at 2.33N-m. The driver choice for this motor is an AllMotion Stepper Driver capable of up to 40V and 2.0A. This hybrid stepper has 1A/phase and contains two phases, allowing it $(2A) \times (40V) = 80W$. However, the curve above represents testing performed at 24V, and any voltage above this does not necessarily help the torque-speed performance but rather allows for smoother motion. This stepper is tested to see if it can raise and lower the 10lb weight in one continuous motion, at a speed of 0.18 m/sec. It accomplishes the task using 0.8A at 24V. Another test is suspending a 20lb weight, or approximately 90N, using active holding torque, i.e. running the motor at a constant speed of 0 (it is recommended to use only up to 50% of the maximum current while applying passive, or standard holding torque). The 2 Stack Portescap Stepper accomplishes this task using 1.65A. Therefore, it is suitable for the alternate actuation scheme from Figure 7.8 since during the 10lb test it had well over 33.33% of its amperage remaining. Two reasons why the author does not select this stepper are: 1) the 1 Stack is shorter in length, 2.115in versus 3.297in, and 2) the 1 Stack is lighter, 0.64kg versus 1.09kg. Note that the testing for this stepper is less developed and insightful than the final testing for the actual selection, since it is done with beta versions of the test bed described in Figure 8.1 above and test methods described in the paragraph below.

For the final Portescap Stepper selection, 23H118D20B-D, the torque-speed curve from the data sheet provided by http://www.portescap.com/ is shown in Figure 8.4 below. The max holding torque while energizing both stepper phases is reported at 1.27N-m. The final driver choice is an AllMotion Stepper Driver capable of up to 40V and 7.0A, but otherwise similar to the choice for the 2 Stack. This 1 Stack stepper is rated for 2A/phase and contains two phases, allowing it $(4A) \times (40V) = 160W$. It is essentially the same motor as the 2 Stack above besides the differences in amperage per phase, pull-out torque, and holding torque. The author tests the final motor choice for feasibility with three methods: 1) find the maximum speed of repeatedly and continuously raising then lowering a 5lb weight 4 in. vertical, 2) method one with a 10lb weight, and 3) suspend a 20lb weight indefinitely. The

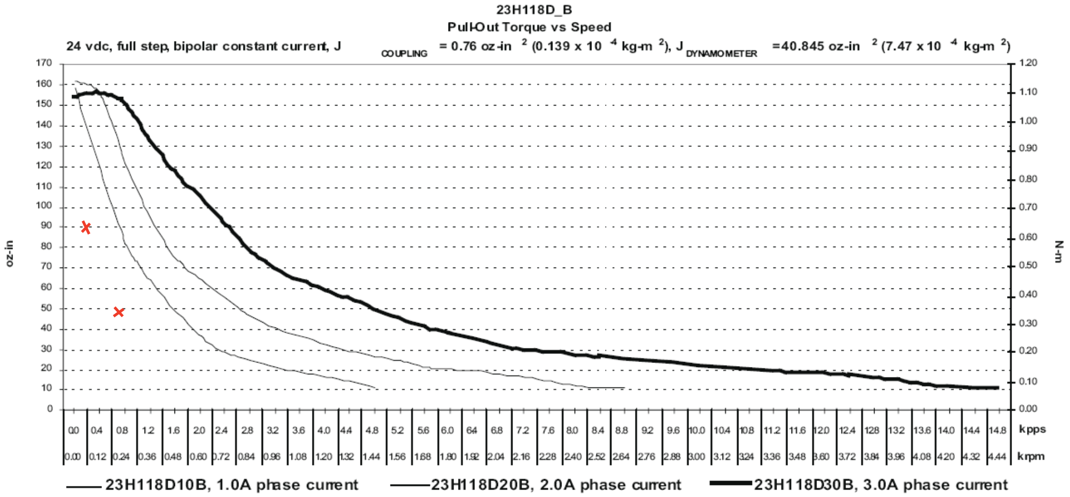

Figure 8.4: Portescap Stepper Torque-Speed Curve - 1 Stack [http://www.portescap.com/]

motor is programmed in Open Loop Mode using a DT Protocol Language, discussed in Subsection 8.3.1, to perform the required functions for testing. For the tests, 24V and only 50% of the available move current of the stepper is used, since in reality a factor of safety of 2 allows protection from disturbances and assures that the motors will not overheat too quickly. The figure below demonstrates performance of the stepper with the 5lb weight at the speed right before its functionality is compromised.

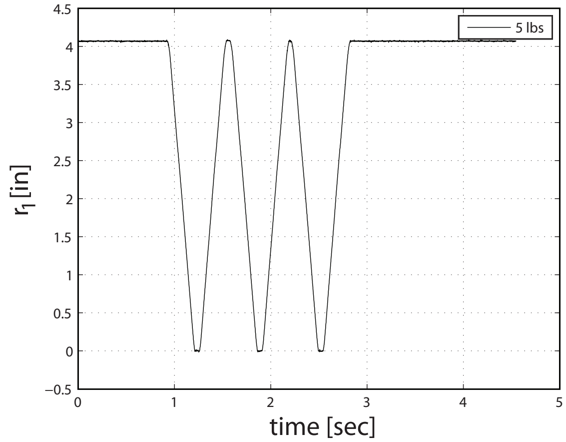

Figure 8.5: Position of rod during 5lb motor test

where distance r_1 is recorded by a cable-pull potentiometer as seen in Figure 8.1. The open loop speed is 0.39 ± 0.02 m/sec, however the sensed speed, from Figure 8.5 above, is 0.31 ± 0.02 m/sec. The stepper passes for leg 2 as the required speed is 0.34 m/sec from Eqn.(6.7). The sensed speed being slightly less is not a real concern, since the actual requirement will lessen due to the max force required occurring at a different time than the max speed required. The result for the 10lb weight test is as follows.

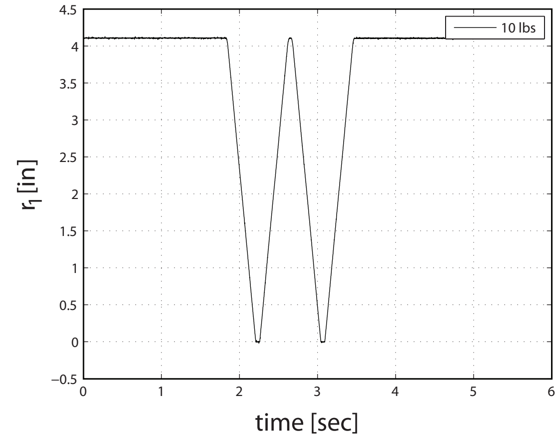

Figure 8.6: Position of rod during 10lb motor test

similar to the 5lb test, r_1 is the potentiometer sensor reading. The open loop speed is 0.28 ± 0.02 m/sec, however the sensed speed, from Figure 8.6, is 0.24 ± 0.02 m/sec. This passes for leg 1 since the required speed is 0.18 m/sec from Section 7.3.

To test the braking torque the author suspends the 20lb weight indefinitely, and to start a passive holding torque is used and the holding current is set to 50%, which is the recommended max. The stepper passes using 1.34A and 24V, and with active holding torque or using over drive it can potentially hold more weight if needed.

The stepper of choice is sufficient to handle worst case scenarios, the alternate actuator control scheme from Figure 7.8, and avoid overheating because it passes all three tests above with a factor of safety of 2. An example of a worst case scenario is the motors consuming significantly more current than necessary to move at their desired speeds, causing them to reach their current limit before they reach their true torque limit. If the speeds of the motors for legs 1 and 2 are controlled they will ideally consume only the amount of current necessary to produce the torque demanded from them, which is that from Figure 7.7. However, the only way to assure this is to control the actual current outputs, which will be pursued upon necessity.

8.2 Detailed Design and Construction of Prototype

The author's primary purpose in constructing a prototype is to demonstrate the feasibility and novelties of the motion regimes. Secondarily, it provides the visualization and test bed necessary to extend the concept into the spherical realm with capacity for motion in any direction, for programming maneuvers, miniaturizing or enlarging, or accomplishing tasks. The author chooses a core radius of $r = 3$in, and a leg length of $L = 12$in to provide the necessary middle ground for experimentation, concept visualization, and ease of manufacturing.

The fundamentals of the design, i.e. actuator selection, drive train concept, motion control concepts, and overall dimensions, have been laid out in Section 8.1 above. This section provides the remaining details necessary to build the prototype, and documents the construction itself. Principals are adhered to, within reason, as components and materials are selected: maximize drive train precision via adjustability (to ensure controllability and minimize friction), maintain balance and structural stability of LAD, minimize weight, minimize depth, and minimize cost.

8.2.1 Drawings

Mechanical design details are presented in the following drawings of parts and assemblies, given context in Subsection 8.2.2, and visualized with manufacturing methods discussed in Subsection 8.2.3 . A conceptual visual of LAD to scale is found in Figure 8.2. Hand drawings of the fundamental core internals are shown on the next two pages. The drawings are close to a 1:1 scale since the originals are life size.

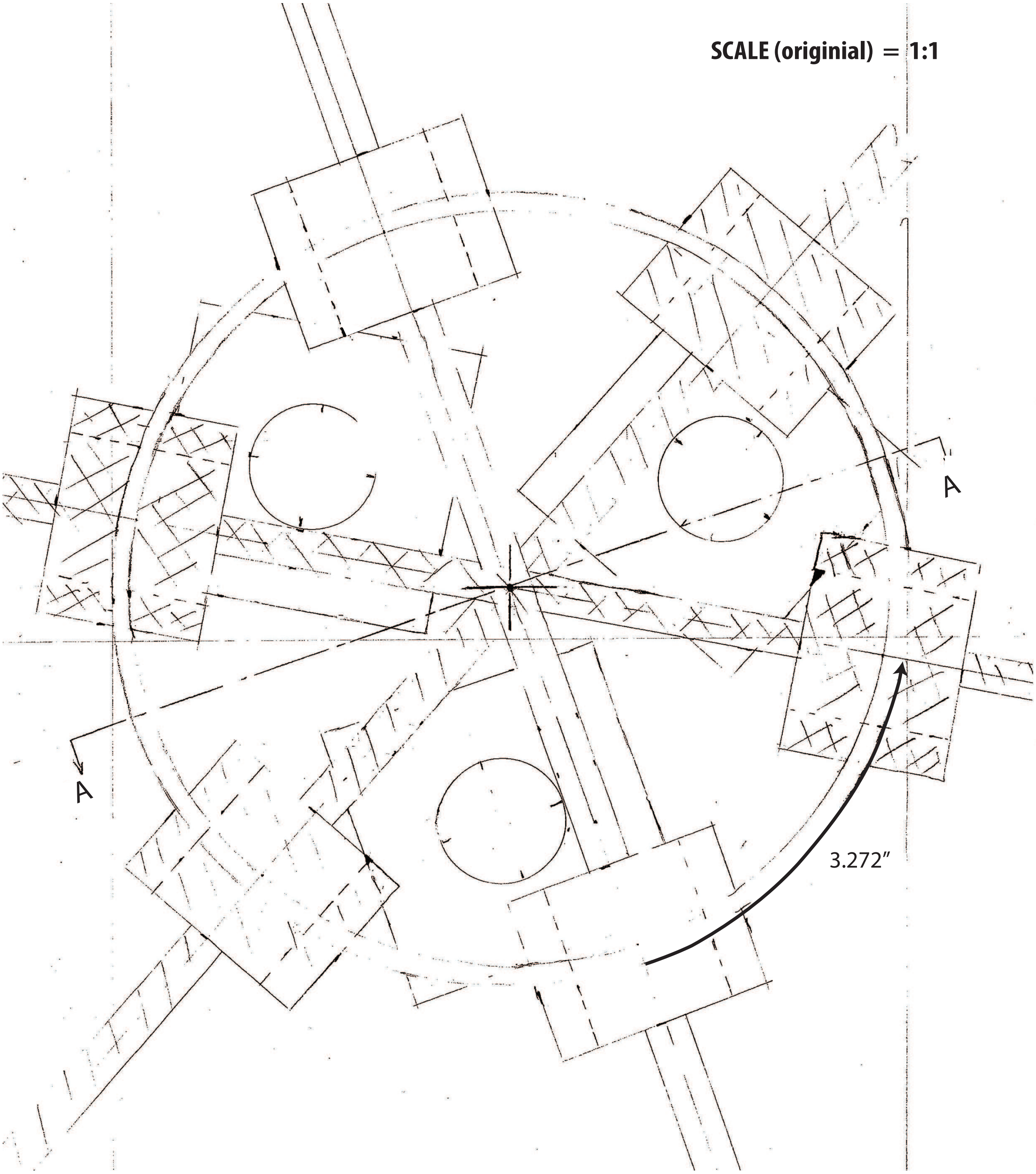

Figure 8.7: Assembly Dwg: Core - Internals Pg.1

SCALE (original) = 1:1

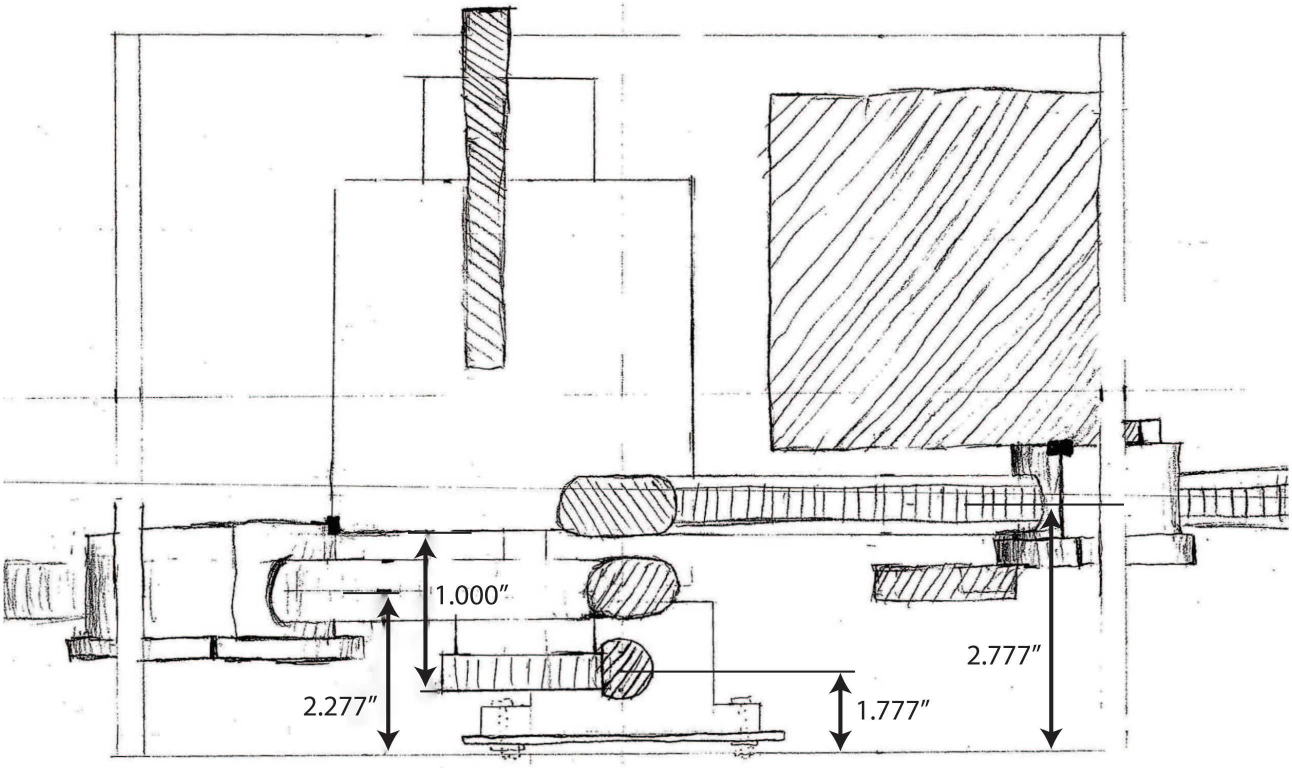

Figure 8.8: Assembly Dwg: Core - Internals Pg.2 (Section ‘AA’)

The next series of drawings are parts of the Drive Train Assembly:

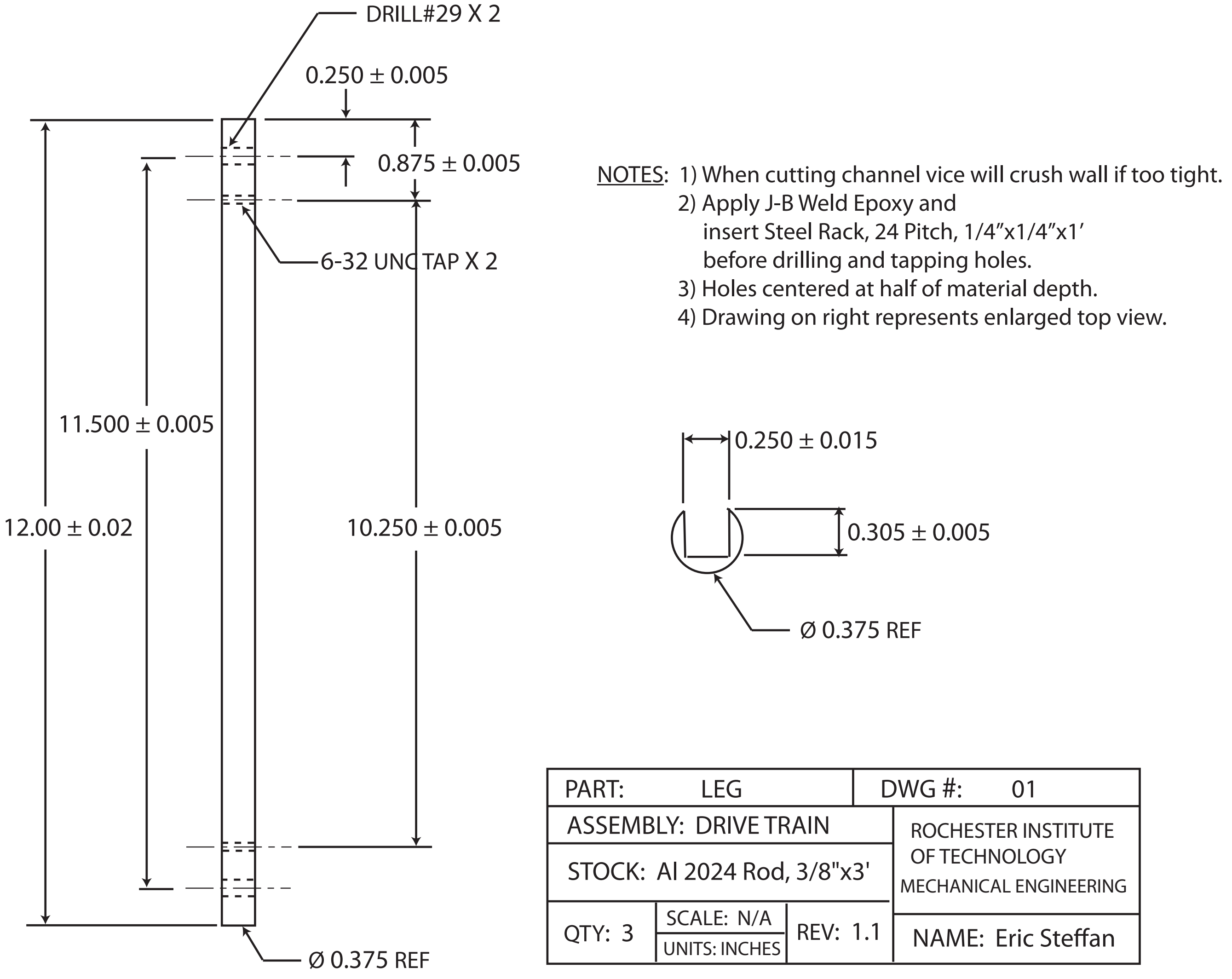

NOTES: 1) When cutting channel vice will crush wall if too tight.
2) Apply J-B Weld Epoxy and insert Steel Rack, 24 Pitch, 1/4”x1/4”x1’ before drilling and tapping holes.
3) Holes centered at half of material depth.
4) Drawing on right represents enlarged top view.

PART: LEG			DWG #: 01
ASSEMBLY: DRIVE TRAIN			ROCHESTER INSTITUTE OF TECHNOLOGY MECHANICAL ENGINEERING
STOCK: Al 2024 Rod, 3/8"x3'			
QTY: 3	SCALE: N/A UNITS: INCHES	REV: 1.1	NAME: Eric Steffan

Figure 8.9: Part Dwg: Leg

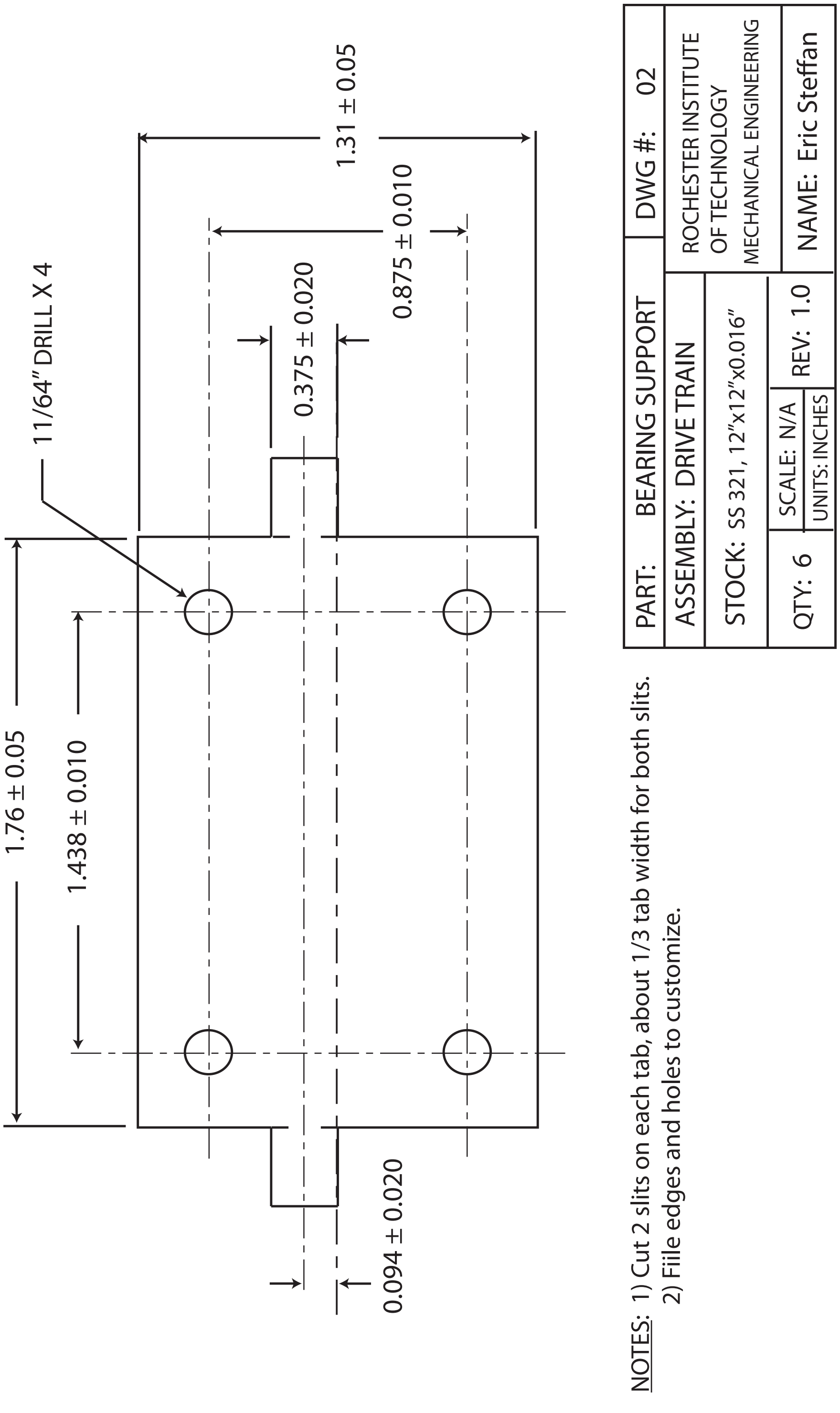

NOTES: 1) Cut 2 slits on each tab, about 1/3 tab width for both slits.
2) Fiile edges and holes to customize.

Figure 8.10: Part Dwg: Bearing Support

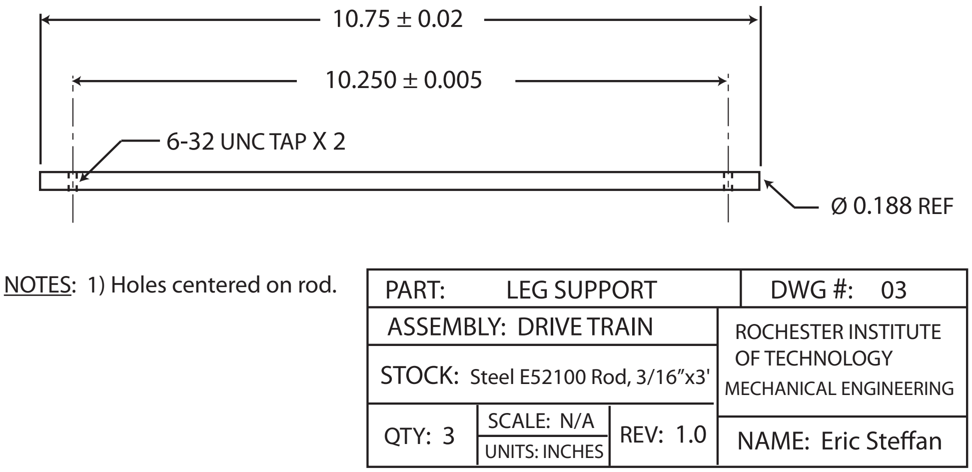

Figure 8.11: Part Dwg: Leg Support

The following drawings are parts of the Foot Assembly:

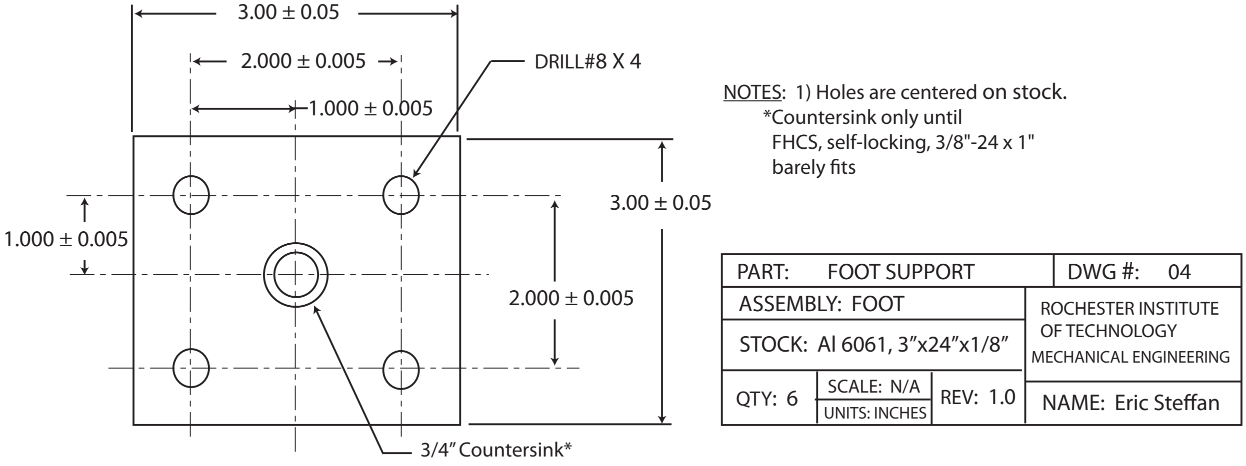

Figure 8.12: Part Dwg: Foot Support

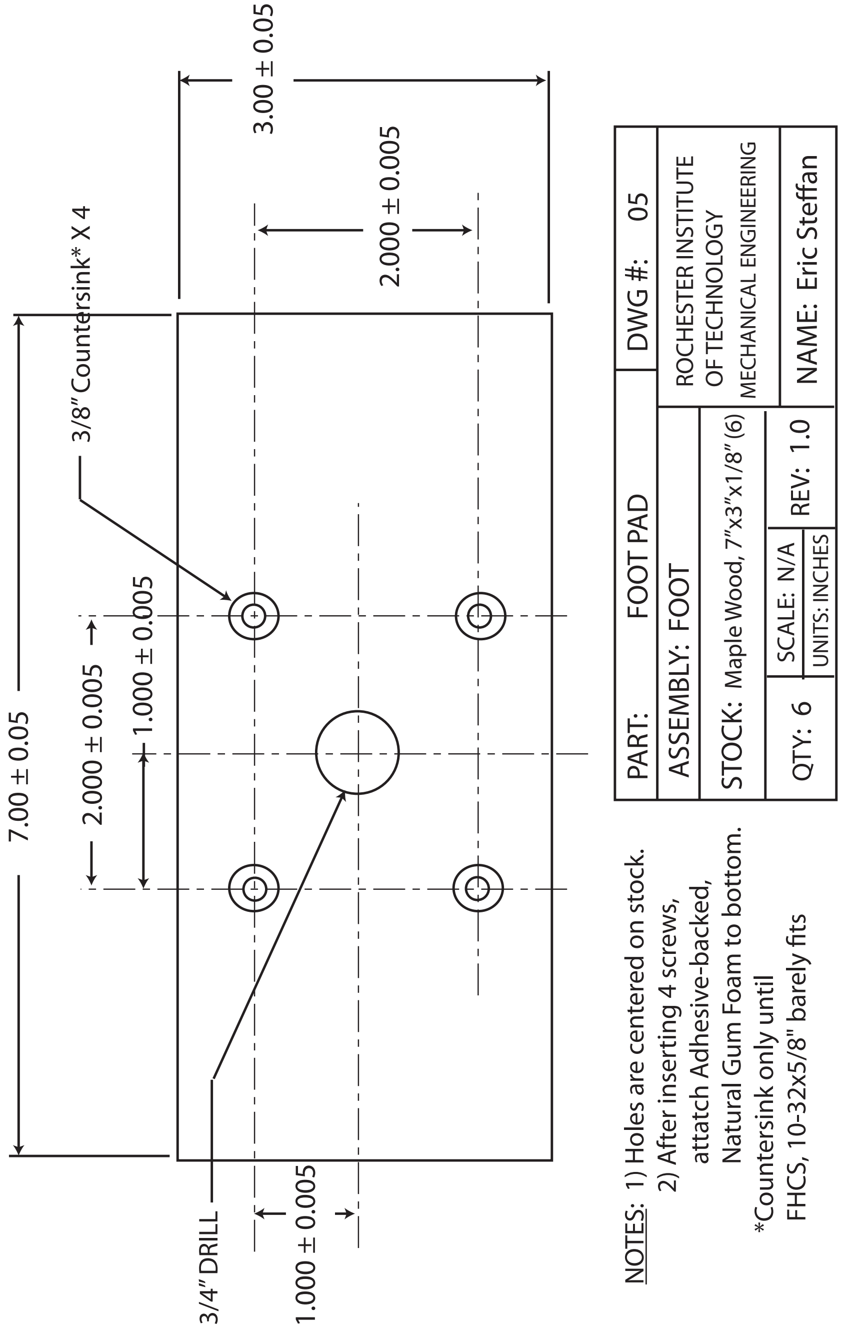

Figure 8.13: Part Dwg: Foot Pad

The following drawing is a mount for the cable-pull potentiometers:

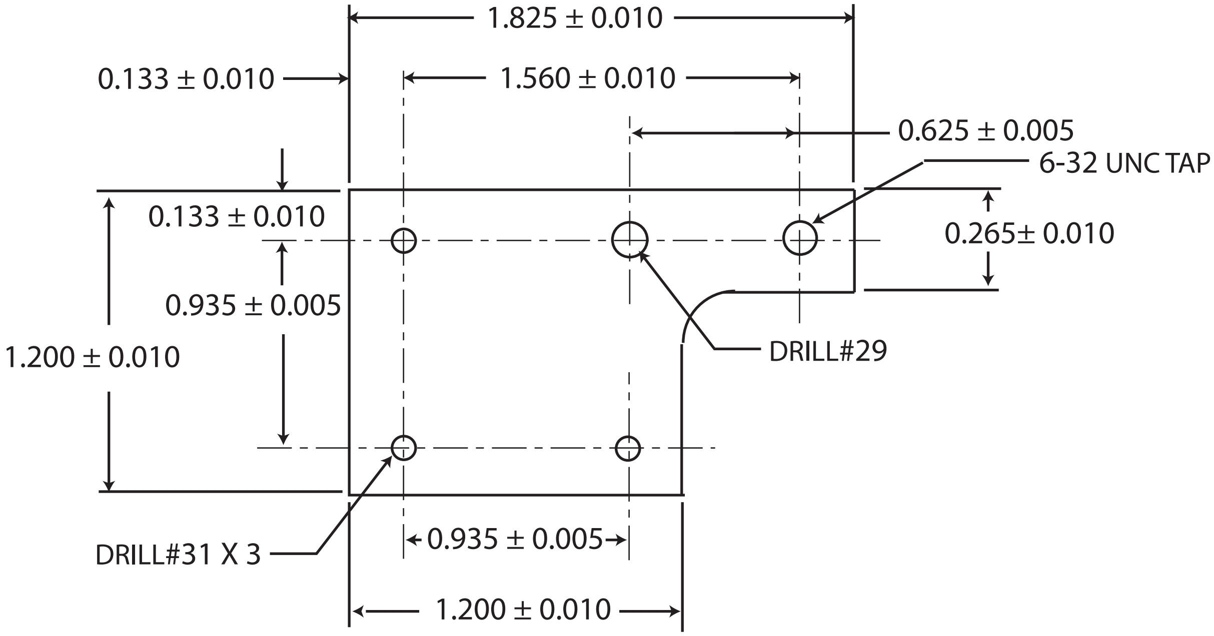

PART: POT MOUNT			DWG #: 06
ASSEMBLY: POTENTIOMETER			ROCHESTER INSTITUTE OF TECHNOLOGY MECHANICAL ENGINEERING
STOCK: Al 6061, 2″x4″x1/8″			
QTY: 3	SCALE: N/A UNITS: INCHES	REV: 1.0	NAME: Eric Steffan

Figure 8.14: Part Dwg: Potentiometer Mount

8.2.2 Components and Materials

Components and materials lists for the Actuator Assemblies, Drive Train Assemblies, Foot Assemblies, Potentiometer Assemblies, Electronics Assembly, and Core Assembly, not including tools, for the construction of the first LAD prototype are located below. The author uses ‘component’ here to mean an asset that is both essential to a particular assembly and has either high degree of complexity or is unique and uncommon by nature. ‘Material’ is used by the author as a simple element or raw stock used to construct a part or assembly. The BOM is established after an extensive technology search, then comparing and contrasting products from many vendors based on criteria with varying priority such as size, cost, amperage, resolution, etc. A streamlined method of comparing products from a wide selection of companies is found in Appendix E. Purchasing decisions for important components and materials are discussed below each table.

Table 8.1: Bill of Materials: Actuator Assemblies

Actuator Assembly X 3 Components and Materials				
Line	Component/Material	Qty	Vendor	Part No.
1	Stepper Motor	3	Portescap	23H118D20B-D
2	Stepper Driver + Startup Kit	3	Allmotion	EZHR23ENHC
3	Optical Encoder, 1250 Resolution	3	US Digital	5-1250-250-I-S-D-D-B
4	1” PD Pinion Spur Gear, 24 Pitch	3	McMaster	6325K88
5	Cable, E5-1250 Encoder	3	Digikey	102-1787-ND
6	Sleeve Bushing	3	McMaster	6391K133
7	10-32x1/2” Set Screw	3		

The Actuator Assembly components are the first four lines of the above table. Lines 1 and 4 are designed in Subsection 8.1.1. Line 2 is chosen based on its compatibility with a NEMA 23 Stepper Motor, or line 1, and its capacity for 40V and 7A, as the next model down is capable of only 2A. Line 1 has 2A per phase, and two phases; it is also capable of over drive so it can potentially use 8A, but typically will use between 1 and 4 Amps. Line 3 is chosen based on size, resolution, and cost; the encoder chosen is small enough to fit inside the core, and has a high resolution of 1250 counts per revolution relative to its cost. The pinion is press-fit to the bushing of line 6 using a vice, and the set screw of line 7 mounts it to the shaft; a flat groove is machined on the shaft and a 10-32 Tap is machined into the combined gear and bushing to provide a robust connection. The distance between the outer pinion face and the motor case is 1 in. for the two steppers closest to core front, and as small as the Core Assembly allows for the furthest stepper. Encoders are mounted on the back of the steppers using Super Glue from line 63 in Table 8.6.

Table 8.2: Bill of Materials: Drive Train Assemblies

Drive Train Assembly X 3 Components and Materials				
Line	Component/Material	Qty	Vendor	Part No.
8	Steel Rack, 24 Pitch, 1/4”x1/4”x2’	2	McMaster	6295K12
9	Linear Bearing, Pillow Block Assembly	6	Nook Ind.	XEP-06
10	Al 2024 Rod, 3/8”x3’	1	McMaster	9061K153
11	SS321 Sheet Metal, 12”x12”x0.016”	1	McMaster	1754T11
12	Steel E52100 Rod, 3/16”x6’	1	McMaster	8938K1
13	J-B Weld Epoxy, 10 oz.	1	McMaster	7605A12
14	Dupont Krytox Synthetic Grease, Std., Gpl 205, 0.5oz	1	McMaster	10195K19
15	6-32x1/2” SHCS	24		
16	6-32x2” BHCS, FT (Qty 2 = 1.25”)	3		
17	6-32x1/8” Hex Nut	33		
18	#6 Flat Washer, 3/8” OD, 0.032” Thk	27		
19	#6 D-Shape Washer, 3/8” OD, 0.06” Thick	24		
20	#6 External-Tooth Lock Washer, 0.320” OD	6		

Lines 8 and 9 are the components that make up the Drive Train Assembly. The rack is chosen to be compatible with the pinion in line 4, and has a small cross section, low weight, and high strength. Linear Bearings are needed to support the rack and pinion assembly with minimal friction in the radial direction, and line 9 provides a compact, low cost bearing for a rod; the square rack is converted to a rod with stock material from line 10, epoxy from line 13, and the part drawing in Figure 8.9. To mount the Linear Bearings to the core, stock material from line 11 is manufactured according to the drawing in Figure 8.10. The tabs are folded perpendicular in the most convenient direction, and the mounts are attached to the core using epoxy. A support for the legs is manufactured according to Figure 8.11 drawing using stock material from line 12.

Table 8.3: Bill of Materials: Foot Assemblies

Foot Assembly X 6 Component and Materials				
Line	Component/Material	Qty	Vendor	Part No.
21	Steel Clevis Rod End	6	McMaster	2447K17
22	Al 6061, 3”x24”x1/8”	1	McMaster	9041K13
23	Maple Wood, 7”x3”x1/8”	6	Pittsford Lumber	
24	Natural Gum Foam, Adhesive-backed, 10’ Length	1	McMaster	93625K283
25	3/8”-24x1” FHCS, Self-Locking	6		
26	10-32x5/8” FHCS	24		
27	6-32x1.25” BHCS, fully threaded	6		
28	10-32x1/8” Hex Nut	24		
29	6-32x1/8” Hex Nut	12		
30	#10 Flat Washer, 1/2” OD, 0.04” Thk	36		
31	#6 Flat Washer, 3/8” OD, 0.032” Thk	12		

A pivoting component for the feet is found in line 21. It provides only one DOF since this prototype is a planar version, and its rotational friction can be varied by adjusting the loading torque or pre-load of the screw in line 27. The feet are designed for quick replacement of the Food Pad to yield different COFs. This design is documented in Figures 8.12 and 8.13 drawings which use stock materials from lines 22 and 23, respectively. Additional Foot Pad Parts can be easily manufactured with varying COF’s by exchanging the rubber sole of line 24 with a different material.

Table 8.4: Bill of Materials: Potentiometer Assemblies

Potentiometer Assembly X 3 Component and Materials				
Line	Component/Material	Qty	Vendor	Part No.
32	Cable-Pull Potentiometer	3	Micro-Epsilon	WPS-150-MK30-P25
33	33kΩ Resistor	3		
34	1μF Capacitor	3		
35	Nylon Eyebolt, 6-32, 25 pack	1	McMaster	9686T71
36	6-32x2.75” BHCS, FT (Qty 2 = 1.75”)	3		
37	4-40x1” SHCS	9		
38	6-32x1/8” Hex Nut	15		
39	6-32x3/16” Nylon-Insert Hex Locknut	3		
40	4-40x3/32” Hex Nut	9		
41	#6 Flat Washer, 3/8” OD, 0.032” Thk	6		
42	#6 External-Tooth Lock Washer, 0.320” OD	6		
43	#4 Flat Washer, 5/16” OD, 0.03” Thk	9		

The component of the Potentiometer Assembly detailed in Table 8.4 below is the Cable-Pull Potentiometer from Micro Epsilon. A thorough technology search is done by comparing position sensor technology from a variety of companies such as optical, ultrasonic, LVDT, and cable-pull using the following criteria: size, resolution, error, range, and cost. Optical sensors of high precision are very costly, ultrasonic sensors are noisy near electromagnetic fields, and LVDT sensors are bulky. Micro Epsilon’s cable-pull potentiometers are compact, with relatively high precision and low cost compared to the competition. Despite their compactness they do not fit inside the 6” ID core, and thus a mount is designed in Figure 8.14 drawing, which uses stock material from line 22 in Table 8.3, to externally fix the potentiometers at one end of each leg.

Table 8.5: Bill of Materials: Electronics Assembly

Electronics Assembly Component and Materials				
Line	Component/Material	Qty	Vendor	Part No.
44	EZ Bus Station	1	Allmotion	EZBUSSTN
45	LDPE Sheet, 12”x12”x1/8”	1	McMaster	8657K112
46	22AWG Stranded Wire, 4 Colors - 100’ ea.	1		
47	CAT-5 Network Cable, 36’	1	Radioshack	
48	RCA Male Connectors, Single, Solder-Type	3	Radioshack	
49	6’ 75-Ohm BNC Cbl.	3	Radioshack	
50	GP BNC-Phono Adpt.	3	Radioshack	
51	CP BNC Coupler FM	3	Radioshack	
52	Heatshrink Pack, Multicolor	1	Radioshack	
53	Electrical Tape, Roll	2		
54	4-40x3/4” SHCS	16		
55	4-40x3/32” Hex Nut	16		
56	#4 Flat Washer, 5/16” OD, 0.03” Thk	16		

To provide a means of transmitting power and serial signals to all three steppers in an organized fashion the component in line 44 is used; to send independent commands with feedback to each stepper three drivers are needed. The material in line 49 allows the potentiometers to connect with dSPACE to send continuous information signals. Line 45 stock material is used to manufacture a mount for the stepper drivers and line 44; a drawing is not necessary and the manufacturing methodology is discussed in Subsection 8.2.3 below. The Electronics Assembly is designed to provide up to about 12ft of wires in between LAD and dSPACE.

Table 8.6: Bill of Materials: Core Assembly

Core Assembly Materials				
Line	Material	Qty	Vendor	Part No.
57	PVC Pipe 6” IDx4.5’	1	McMaster	2426K27
58	PVC End Cap, 6.25” OD	2	Alliance Plastics	K1274A
59	1018 Carbon Steel Cylinder, 6”x1/2”	1	McMaster	7786T72
60	1080-1090 Carbon Steel Wire, 0.020” Dia., 234’	1	McMaster	9666K19
61	Electric Glue Gun Kit, 120 V, 1/2” Cap	1	Grainger	1PKX1
62	Thread, Spool	1		
63	Gorilla Super Glue, 0.71oz	1		

The Core Assembly is unique in that every other assembly excluding the Foot Assemblies are directly connected to it; thus the core is thought of as the top level assembly for LAD, as depicted in the assembly drawings of Figures 8.7 and 8.8. One purpose of these drawings, along with drawing Figure 8.2, is to show feasibility of the core radius $r = 3$in with the equipment purchased; they establish the size criteria in purchasing. Since the core material of line 57 is highly interconnected it is the most difficult piece to manufacture. Thus, the material is chosen as PVC since it is easy to machine, flexible to provide give, and cheap allowing defective parts to be discarded. To contain all of the assemblies a core depth of 7.25 in. is required. A detailed drawing is not provided for the Core Part due to the bulky cylindrical shape of the stock and oddly shaped holes which make precise machining on a mill difficult and time consuming. Manufacturing techniques for the core are discussed in Subsection 8.2.3 below.

8.2.3 Methods

The Actuator and Drive Train Assemblies are constructed first, then the Core Assembly, or top level assembly, is built. The Foot Assemblies, Potentiometer Assemblies, and Electronics Assembly are constructed when desired and added to the Core Assembly. See the above Subsection 8.2.2 for short explanations of the various assemblies. This section will focus on methods used to achieve the necessary precision, reduce manufacturing time, and overcome obstacles.

Once the actuator is selected, the remaining design and manufacturing of the Actuator Assembly is simple; it is explained below Table 8.1. However, manufacturing the Leg Parts in Figure 8.9 drawing for the Drive Train Assembly is difficult (at least for a non-programmable mill) due to the effects of chattering, vice force, and the leg length. It is crucial to use a relatively new 1/4” Square, Carbide End Mill (McMaster #8745A11) to cut the channels in the aluminum rods. Note that the vice needs to be tightened the correct amount since being too loose will increase chattering, and being too tight will cause the channel walls to elastically deform and interfere with the end mill resulting in an enlarged channel width. To machine the entire leg length the vice must be loosened and the section that is unmachined is slid, with the end mill remaining in the channel, into the vice grip. After machining the channel and filing as needed, when inserting the rack with epoxy it is important to apply vice pressure along the entire top of the rack for about twenty four hours.

The design method for the Core Assembly is one of intuitive marking and roughly cutting by hand, then refining and adjusting to within tolerance. PVC is the material of choice for the core, line 57 from Table 8.6. There are three primary reasons for the choice of design method and associated material: 1) to obtain high precision cuts on a curved surface would require extensive time to detail on a CAD program then program on a mill, and any error would result in much more time spent redesigning and machining again, 2) PVC is soft and can be cut by hand easily, and 3) PVC is inexpensive so many attempts can be made at manufacturing without a large cost of time or money. The following pictures and explanations detail the author’s intuitive design and refine methods used:

To begin the Core Assembly the author uses a coping hand saw to cut rough holes along the surface of the core in the shape of the linear bearings from line 9 of Table 8.2. The locations of the centers of these holes are found in the Core Assembly drawings from Figures 8.7 and 8.8. This allows the Drive Train Assembly to be mounted as shown on the next page.

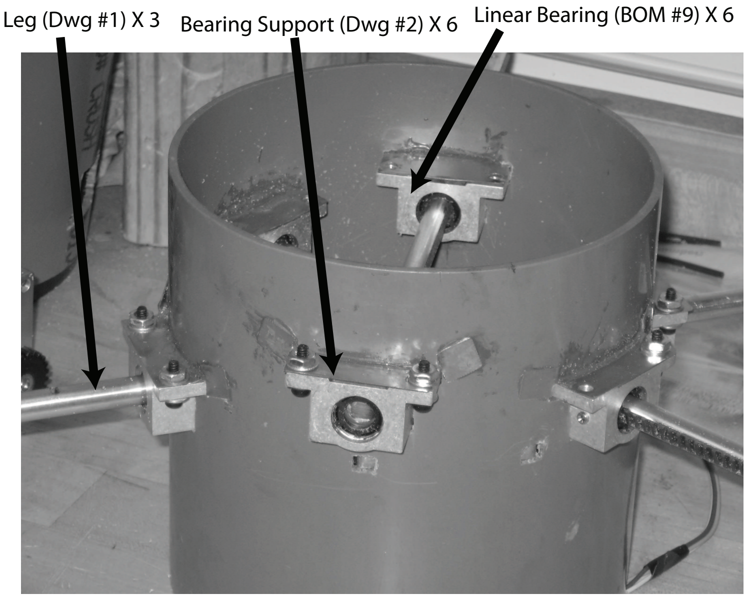

Figure 8.15: Drive Train Assembly mounted on core

To measure around the curved surface a piece of thread is used according to the length specified in the first Core Assembly drawing, and a metal marker is used to punch the hole centers. Before tracing the linear bearings with pencil all items involved are made secure and level. A power drill is used with a 7/32” drill bit to allow entrance of a coping saw. When all of the holes are made, files are used to align holes on opposite sides until a straight ruler is level to the vertical when pressed against the bottoms of both holes. The linear bearing supports are epoxied to the core after twisting their tabs in the direction allowing the resulting jagged edges to face away from the bearings. Precision files are used to make refining adjustments as needed.

The first stepper is laid in the core to mesh with the rack. A probing drill hole of 1/16” is made to identify the stepper’s location. After the location of its corners is determined a drill hole of 7/32” is made in their approximate location. A square precision file is then used to create holes which allow the motor to nestle into the core and rack. By checking the motor placement and gear meshings several times throughout the process, a sufficient mesh is made. The stepper corner holes are shown in the picture above, below the center bearing.

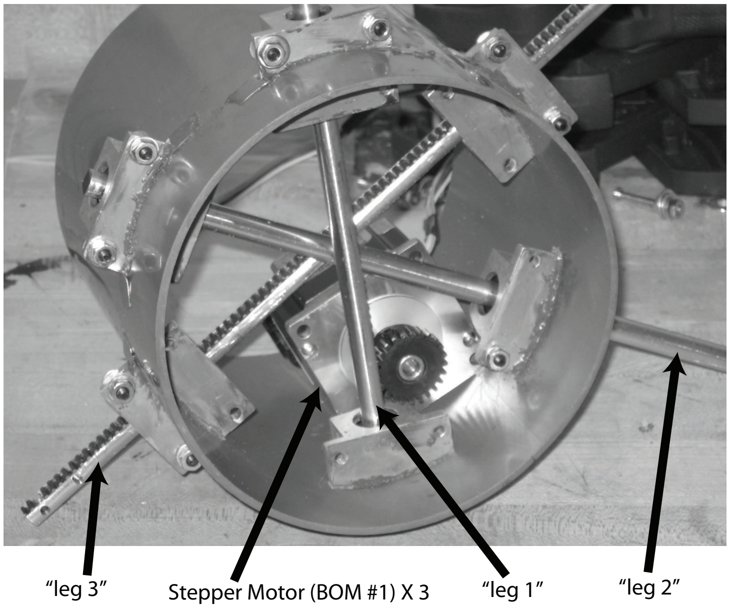

Figure 8.16: Rack and Pinion engaged on core

This photo illustrates the meshing of the rack and pinion. The intuitive design methods used rely heavily on creating the capacity for adjustments and fine tuning. Bearing placement affects both leg sliding friction and gear meshing. The bearings are adjusted with 3 DOF; two of these directions result from the bearing fasteners clearance, and to adjust the depth of the bearings washers or shims of various thicknesses are placed in between the bearings and supports. To align further and achieve the desired friction, the bolts are tightened in a certain sequence with the right amount of torque, which is determined by trial and error as needed. The gear meshing can be adjusted separately as explained below Figure 8.18.

To distinguish the legs in terms of their depth on the core, the author refers to the leg closest to the front of the mechanism, i.e. the leg with the motor in the picture above, as leg 1, the leg in between the others, i.e. counterclockwise from leg 1, as leg 2, and the leg furthest from the front, i.e. clockwise from leg 1, as leg 3. The motor meshed to leg 1 is motor 1, to leg 2 is motor 2, etc. Note that these numberings are made for referencing only, since the author has previously defined the legs and their corresponding actuators as constantly changing when the motion regimes repeat.

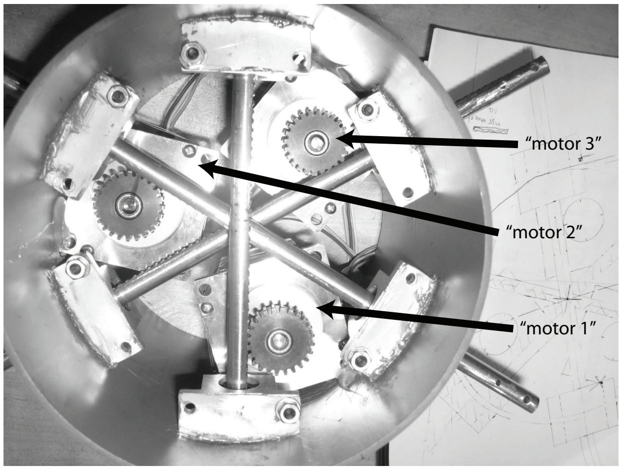

Figure 8.17: Actuator Assembly mounted on core

The pinion location of 1" as denoted in Figure 8.8 only applies for motors 1 and 2. In an effort to reduce the overall core depth, the pinion placement on motor 3 is as close as possible to the motor within reason. Pinion mounting is explained in the paragraph under Table 8.1. Note that two bearings will interfere with motors 1 and 2 if the appropriate bearing corners are not filed.

Figure 8.18: Securing and adjusting the motors

After the motors are nestled in their locations, hot glue is applied to their edges and in the holes created for the stepper corners. Then 1/16" holes are drilled, at a depth of approximately the motor centers, for a steel wire to wrap around the motors and constrict, as a twist tie, using Linesman pliers. The gear meshing can be adjusted by loosening the wire and heating the glue, repositioning the motor, allowing the glue to dry, and finally retightening the wire with the twist in a better location. Super glue can be applied to further secure the motor or any other part, but is not recommended unless the mesh is near perfect.

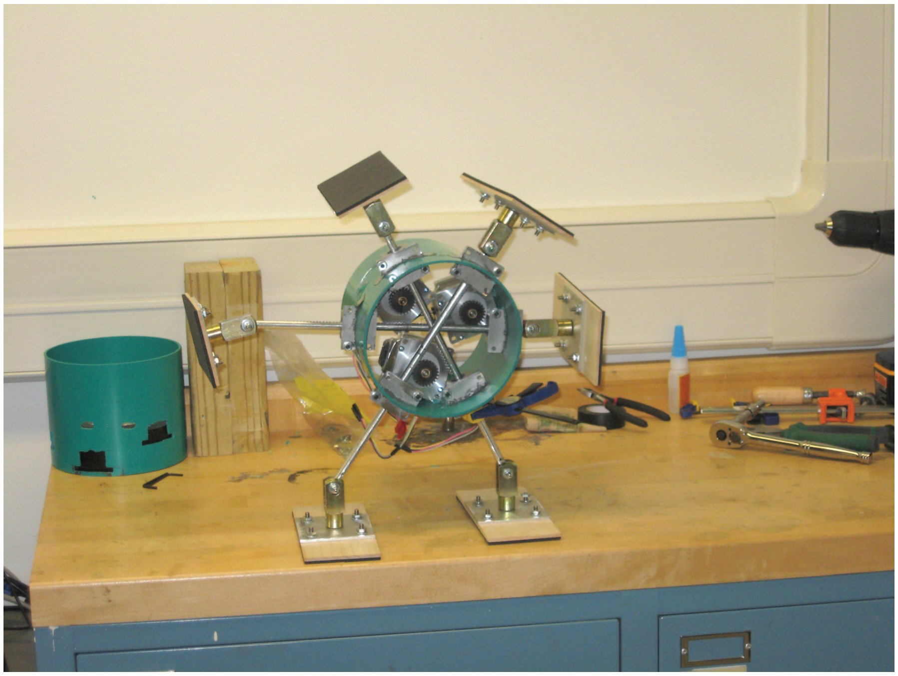

Figure 8.19: Foot Assembly mounted on Drive Train Assembly

The Foot Assemblies are attached and can be adjusted by tightening or loosening the pivoting screw. It is evident that more leg support is needed since the only thing preventing the legs from rotating are the rod's channel wall's contact with the pinions. To supply the support the author adds a steel support rod, or line 12 on Table 8.2, to the Drive Train Assembly.

The design for the supports is found in drawing Figure 8.11 but the assembly is rather intuitive. As seen in Figure 8.20a, for legs 1 and 2, the support will lie about 1/4" from the bearings. A plastic block is shaped to ensure that the same height is achieved for all four core holes for legs 1 and 2. The support is laid on the plastic block and made secure, straight, and level before the rod hole is traced in pencil on the core. The hole center is punched with a steel marker, drilled with a 1/16" bit as a center punch, then a 7/32" bit, and widened with a round precision file until the linear friction of the steel rod is negligible.

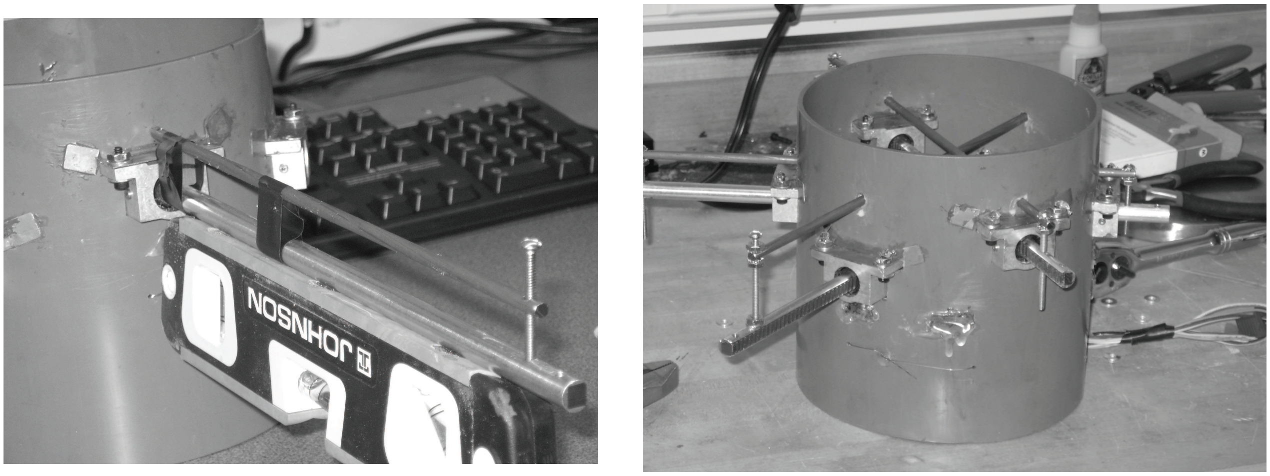

(a) Leg Support Mounting Method

(b) Leg Supports Assembled

Figure 8.20: Leg Supports mounted on core

Notice in Figure 8.20b that the leg 3 support is assembled between the leg 1 and 2 supports such that about a 1/16" clearance is in between the supports. Any interference is filed, all rods are lubricated, and the linear bearings and motor location are adjusted until the Drive Train Assembly is calibrated for negligible or minimal linear friction with optimal rack and pinion meshing. Note that the screw line 16 on Table 8.2 may be substituted with a smaller length screw for legs 1 and 2.

In Figure 8.21, offsetting is used to overcome fouling of the legs and their supports. The angle between the legs, ϵ, is manufactured with care at close to 60°. Since the angle between each pair is not exactly 60°, the author distinguishes the angles as ϵ_i, where $i = 1, 2, ..., 5, 6$, with the first angle open to the ground between legs 1 and 2 and subsequent angles counterclockwise. Error in both the mechanics and controls is compensated for by the flexibility of the plastic core, which resembles the deformable skin of an amoeba in this manner.

A counterweight of 4 lbs is used in Figure 8.22 to offset the weight of the motors in the back, which are the bulk of LAD's mass at a combined weight of 4.2 lbs. The counterweight is an Alloy 1018 Carbon Steel Cylinder, line 59 on Table 8.6. This steel has a density of

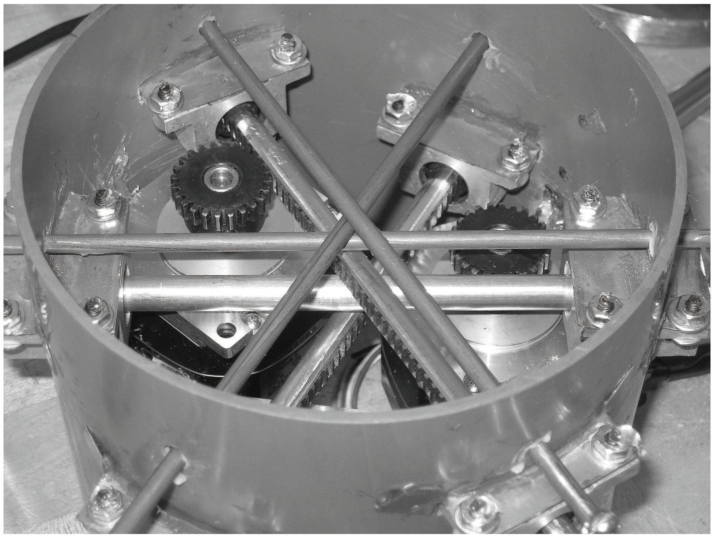

Figure 8.21: Core mechanical internals

Figure 8.22: Counterweight mounted on core

$0.283\ lb/in^3$, and it follows that $(Mass) = 0.283 \times (Volume) = 0.283(\pi(r = 3)^2)t = 4$, where t is the cylinder height. Therefore, $t = 0.5$in. As shown in Figure 8.22, the counterweight is attached with hot glue for easy removal.

For the electronics mount in Figure 8.23, the author recommends LDPE because it is easy to machine, has electrical resistance, and absorbs heat from the drivers. Manufacturing time is minimized by neglecting a drawing since high precision is not needed. A circle

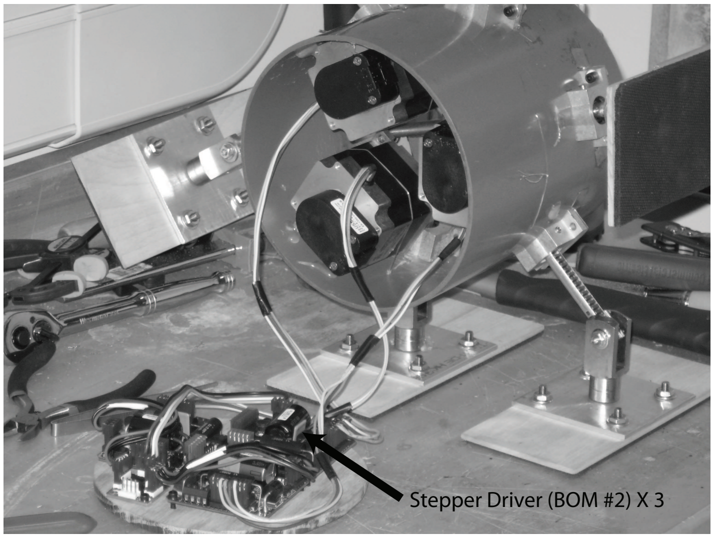

Figure 8.23: Electronic Mount design

slightly less than 6 in. is traced with a compass, then the three drivers and hub from line 44 on Table 8.5 are laid in place. The holes are traced in pencil then all machining is done by centering a 1/8” drill bit by eye, and the circle is machined roughly with a bandsaw.

Figure 8.24 below shows the electronics being assembled to the core. If needed, holes may be cut in the electronics mount for motor and encoder wires to pass through, and the mount is attached to the core with hot glue for easy removal, in a similar manner to the counterweight above. A slit is carved in the plastic end cap with a utility knife for the wires to exit.

In Figure 8.25, note that the 2.75” screw, line 36 on Table 8.4, may be replaced by a 2” screw and a 3/4” screw, or by a 2.75” threaded rod and a lock nut; also note that 2 of the 3 screws required only need to be 1.75”. The 1.25” pivoting screw, line 27 on Table 8.3, is designed to support the potentiometer mount, drawing Figure 8.14, after being inserted in the largest hole with grease from line 14 on Table 8.2. With the potentiometer cable drawn parallel to the leg, pencil the inside of the circular tab on the core. Drill a 1/8” hole in the center of the marking. Cut the eye off of the eyebolt from line 35 on Table 8.4, leaving a threaded nylon tee. Insert the tee into the circular tab, then screw into the 1/8” hole until flush. Adjust the cable by moving the position of the tab and by turning the tee until it is

Figure 8.24: Electronics Assembly mounted on core

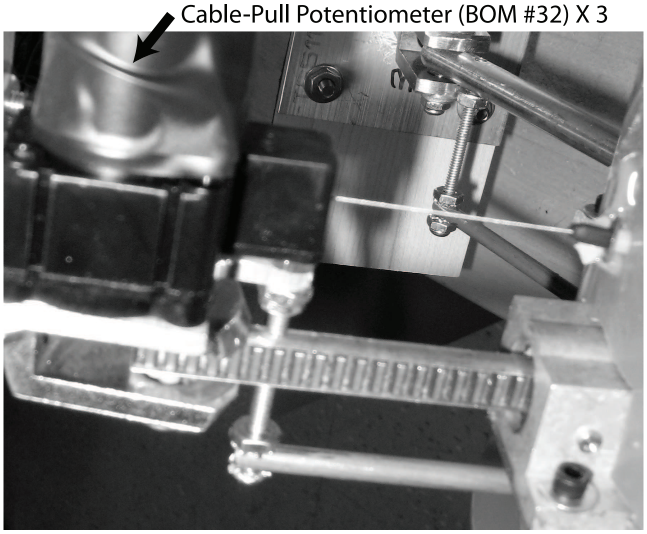

Figure 8.25: Potentiometer Assemblies mounted on core

approximately parallel with the leg, then apply hot glue to secure.

Underneath the electrical tape around the potentiometer is an RC low-pass filter to prevent aliasing of the signal. The design and implementation of this analog circuit is found in Subsection 8.3.2 above Figure 8.32.

In Figure 8.26, there is approximately 12 ft of wire between LAD and the dSPACE Interface and Power Supply. The encoder cable from line 5 of Table 8.1 is spliced, using

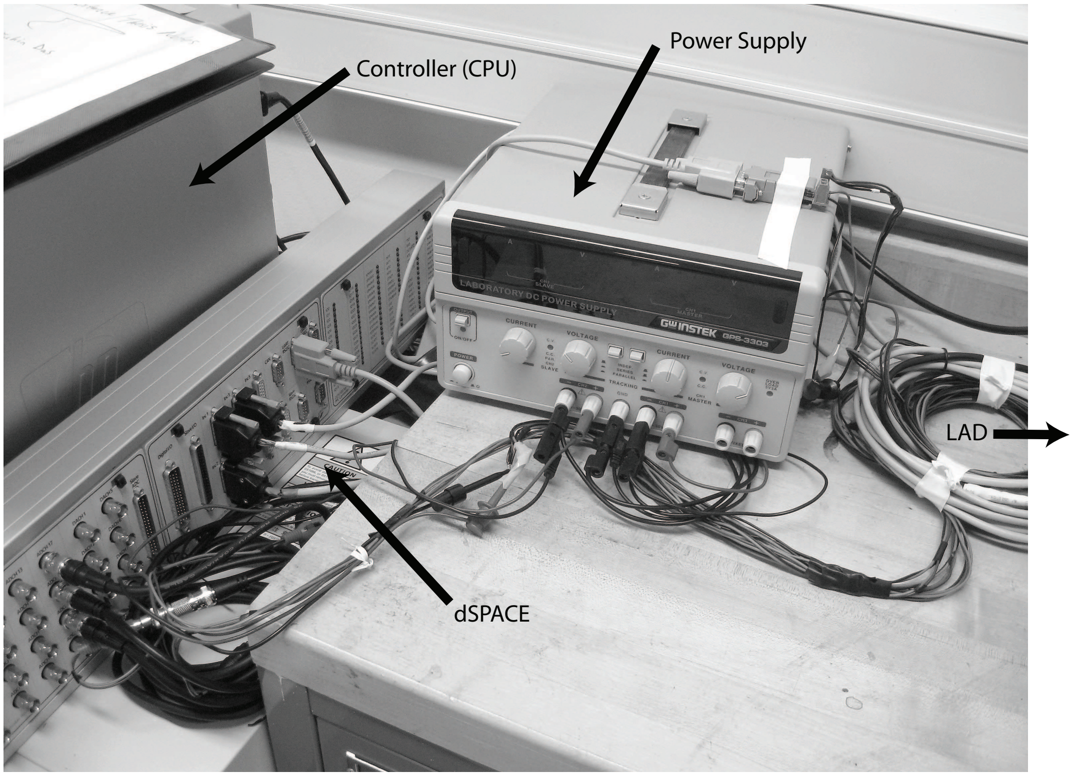

Figure 8.26: System description

solder and heat shrink, with cable from line 47 of Table 8.5, then soldered to the dSPACE Incremental Encoder connector. Two wires from the potentiometer are connected to the Power Supply, and the other two are soldered to an RCA connector, then lines 49, 50, and 51 from Table 8.5 convert to a BNC cable which connects to the analog input of the dSPACE Interface.

Power is input to LAD, depicted in Figure 8.26 from the Power Supply to the stepper drivers and potentiometers. Serial commands are generated by the CPU, converted to C programming language by dSPACE, then processed by LAD stepper drivers.

Signals are output from LAD potentiometers and encoders to the dSPACE Interface and ultimately the CPU, allowing closed loop or feedback control.

LAD, depicted in Figure 8.27, is roughly a circular shape with a 15 in. diameter, and a depth of 9 in. The robot weighs approximately 16.0 lbs, with each leg weighing about 11 oz. More parameters from the first LAD prototype are found in Appendix B.

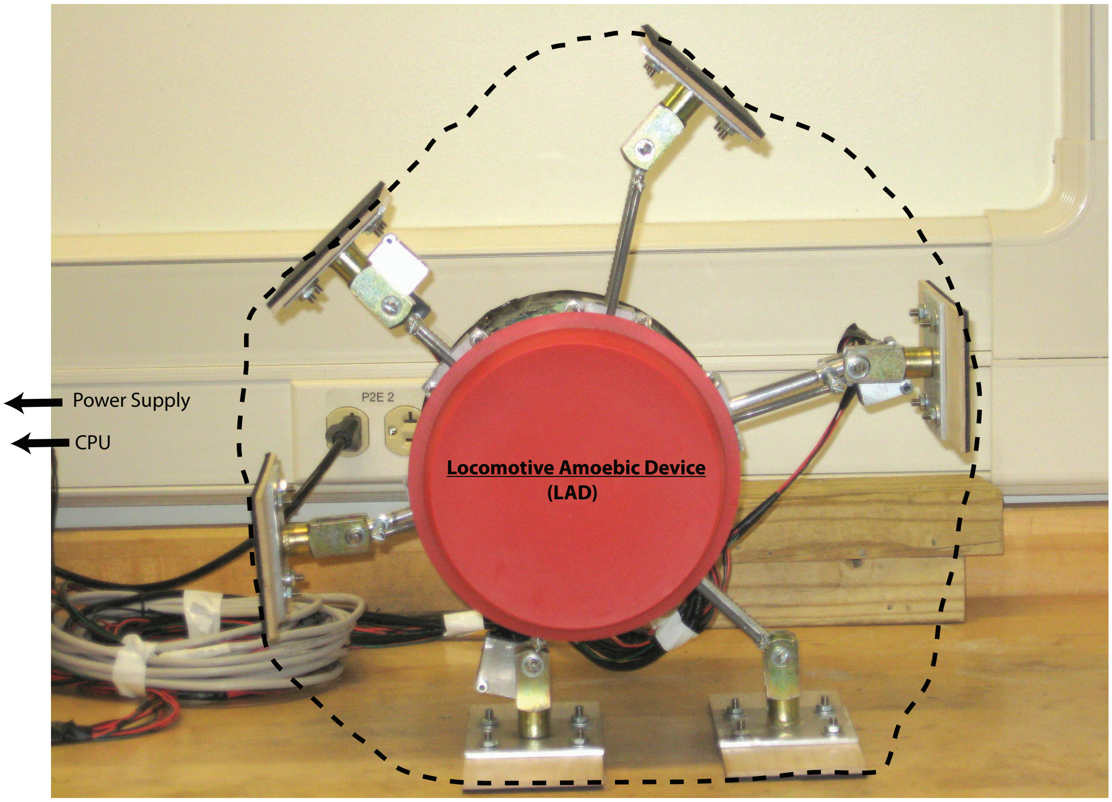

Figure 8.27: Locomotive Amoebic Device (LAD)

8.3 Controls Implementation

To implement feedback control with a stepper motor is inherently more difficult than a servo motor, as many vendors, including AllMotion, do not recommend steppers for feedback applications although they admit it is possible. This is the primary obstacle addressed in this section, and the discussion is in Subsection 8.3.3.

Using the primary actuation scheme from Figure 7.7, the geometric constraints provide an additional robustness and decrease energy costs in LAD's response to external disturbances. The mechanical constraints also function as a check of the theory and implementation, since the controls will not function if they do not abide by the mechanical path trajectory.

However, using the alternate actuation scheme from Figure 7.8, the geometric constraints provide the upper level control of the path trajectory of C. Since this scheme involves the control of a single actuator at a time, it is easier to implement and thus will be implemented first.

8.3.1 Open Loop

Stepper motors are often used in robotics because of their precise Open-Loop Control capabilities. Learning to program the steppers in open-loop is necessary for times when it is advantageous for LAD to function in an open-loop mode.

The commands for the Portescap Stepper 23H118D20B-D with AllMotion Stepper Driver EZHR23ENHC are in DT Protocol. In Appendix D there is a list of essential stepper commands in both DT Protocol and Decimal as arrays of bytes. Decimal representations of characters are used in a Simulink block diagram in Matlab to communicate with dSPACE in arrays of bytes.

Speed commands are coded in microsteps/sec. The stepper has $1.8°$ steps and is running in $1/256$th mode, which implies that there are 200×256 microsteps per revolution. Therefore convert from [microsteps/sec] to [rev/sec] by dividing by 51200 microsteps/rev. For example, 0.18 [m/sec] is multiplied by 39.370 in/m to convert to 7.09 [in/sec], divided by π in/rev since the pinion diameter is 1 in., then multiplied by 51200 to convert to 115,494 [microsteps/sec].

8.3.2 Calibration of Sensors and Filtering

Calibration of the encoder (BOM #3) is done using the knowledge that there are 1250 ticks/rev or 1 tick $= 0.288$ deg. The potentiometer (BOM #32) is calibrated by measuring the draw length to be 6.21 in. and the knowledge that 10V $= 6.21$ in. By comparing the sensor signals to the open-loop motor speed the author discerns any factors of 10^X, where X is an integer, that are needed for a complete calibration. The calibration constants used for controls implementation are found in Appendix D.

Note that the sensor outputs are quantized and also any output from dSPACE is quantized, and the sensors have uncertainty; all of these contribute to signal noise. Resolution of the potentiometer is 0.00394 in. and uncertainty is ± 0.0155in from Micro-Epsilon literature. Resolution of the encoder is $0.288°$ from US Digital literature and it is an incremental encoder with a 2 channel quadrature TTL square wave output, so an uncertainty of $\pm 0.576°$ is assumed. Resolution of dSPACE is approximately $4.8\mu V$, which will have a negligible effect on the signals relative to their inherent noise.

On the test bed from Figure 8.1 the motor is run at various speeds in open-loop to check sensor calibrations after filtering, and compare different sensor outputs based on signal quality and placement of the sensors on the system. The solid line of Figure 8.28 is the encoder sensing rotor speed and the dotted line is the potentiometer approximating rotor speed by first using a Discrete Derivative block in Simulink, then converting [in/sec] to [rev/sec] by dividing by π in/rev. The motor is run at 0 microsteps/sec and it is evident that the encoder is calibrated with minimal error and the potentiometer has error potentially as large as ± 0.005 [rev/sec] due to uncertainty and noise. It is also observed from the plot that the rack exhibits nonlinear behavior such as backlash, and is slower to both decelerate

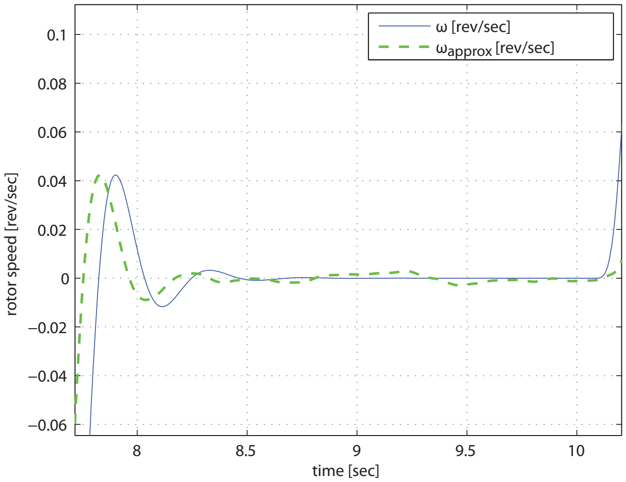

Figure 8.28: Calibration of sensors: 0 microsteps/sec

and accelerate than the pinion, which the author presumes is from the inertia of the rack and imperfect meshing.

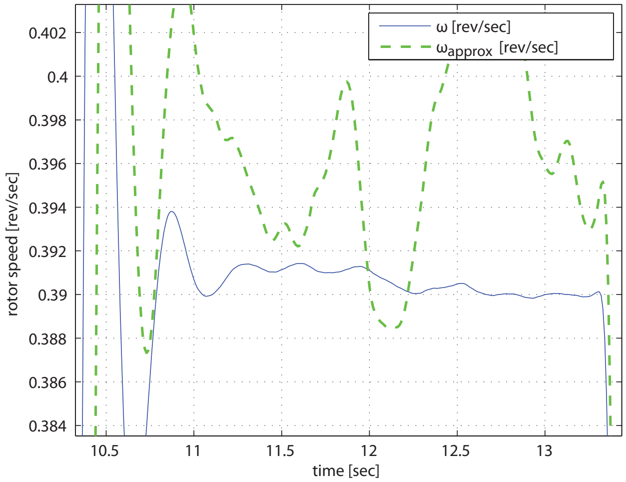

Figure 8.29: Calibration of rotor speed sensors: 20000 microsteps/sec

Motor speed, ω, is set to 20000 microsteps/sec or 0.391 rev/sec. The encoder is converging on 0.391 rev/sec until it slows down slightly, perhaps because of the inertia and nonlinearities that the rack introduces.

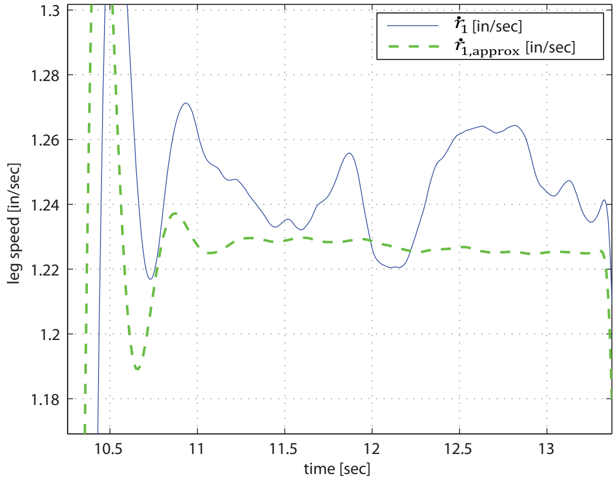

Figure 8.30: Calibration of leg speed sensors: 20000 microsteps/sec

In Figure 8.30 the solid line is the potentiometer sensing leg speed and the dotted line is the encoder approximating leg speed by multiplying by π. Motor speed is still 20000 microsteps/sec or 1.23 in/sec. The potentiometer appears to be converging to 1.24 in/sec due to some combination of nonlinearities and acceptable sensor error.

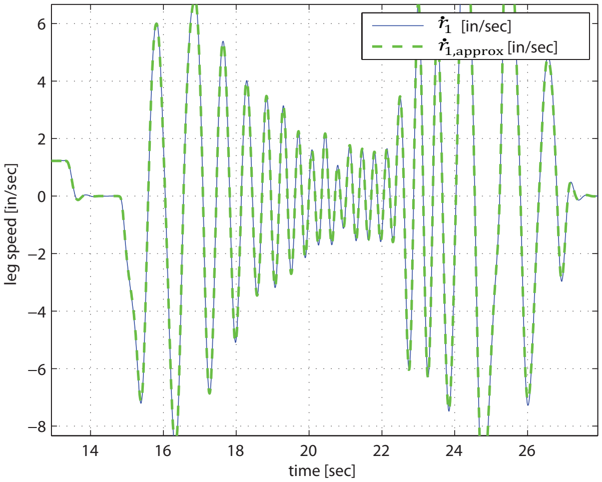

Figure 8.31: Checking calibration of leg speed sensors: 2 Hz

In Figure 8.31 the leg is moved back and forth by hand at about 2 Hz, which is equivalent to four direction changes per second which is plenty for any maneuver of LAD presently. The sensors respond appropriately even with a RC low-pass filter connected to the potentiometer, designed for a cutoff frequency of about 5 Hz to prevent aliasing.

A resistor of 33kΩ and capacitor of 1μF are used in the passive RC circuit.

$$\tau = RC = 0.033\text{sec} \tag{8.7}$$

$$f_c = \frac{1}{2\pi\tau} = 4.82\text{Hz} \tag{8.8}$$

where τ is the time constant and f_c is the cutoff frequency. Figure 8.32 on the next page is a photo of the RC circuit implemented. Note that the actual assembly of LAD uses a more compact version of this circuit, with solder holding the electrical elements in place and electrical tape protecting them.

Sampling rate, F_S, and a 4th order low-pass Butterworth digital filter are designed by trial and error using Matlab, to reduce the noise in the sensor signals.

Figure 8.32: Analog Filter for potentiometer

$F_S > F_N = 2F_{MAX}$, where F_N is the Nyquist frequency and F_{MAX} is the maximum continuous frequency outputted by the system. Assuming $F_{MAX} = 2.5$Hz implies $F_N = 5$Hz. The author chooses $F_S = 40 \times F_{MAX} = 100$Hz.

In Matlab, Wn represents the cutoff frequency for a Butterworth filter, where 0.0 <Wn <1.0, with 1.0 representing half of F_S. We choose Wn = 0.05, i.e. $0.05 \times 1/2F_S = 2.5$Hz, for both the potentiometer and encoder.

8.3.3 Closed Loop with dSPACE

Two challenges in implementing feedback control on stepper motors are providing the motor digital velocity commands, and enabling automatic, near instantaneous direction change. Note that using dSPACE to issue stepper commands initially in Decimal is not well known and no vendor was knowledgeable on stepper feedback control, especially with dSPACE.

To address the first challenge the author devises a way to convert each element of a discrete array of velocities into a vector containing the ones place, tens place, hundreds place, etc., and extract a plus or minus sign to indicate direction. The key to writing Matlab code to accomplish this task is to divide the speed number by 10^X, where X is a counting number, then round down to the nearest whole number to obtain an element of the new vector. A sample of the code is available in Appendix D.

The second challenge is to convert a plus or minus sign into a direction change command. Stepper motors, at least paired with the driver model in BOM #2 (AllMotion Stepper Driver EZHR17EN Software Version 6.9981 and later can perform ‘on-the-fly’ commands), cannot perform a direction change and a velocity change at the same time, which is necessary to accomplish maneuvers using feedback control. Furthermore, to change direction the stepper must first be given a stop command before inputting a speed in the opposite direction. We devise a way to to this by creating a Simulink block diagram with a convoluted series of If-Then blocks mixed with strategically placed Multiport Switch blocks. Even with flawless logic, the stepper only changed direction a small percentage of the time; the key to achieving robustness is to strategically place discrete time delay blocks. This became evident after monitoring in real time on the dSPACE ControlDesk the value of a Simulink block which indicates direction juxtaposed with the value of a block indicating the direction command given to the stepper. The catch was that multiple, quick direction change commands were too much to be processed by the driver and thus the time delays allow the commands to be understood. A sample of the block diagram is found in Appendix D.

A PID CLAW is implemented to control leg 1 with the alternate actuation scheme from Figure 7.8. Trial and error is used in the dSPACE ControlDesk to tune the compensator for stability, and quick, accurate response to a constant reference velocity; $K_p = 0.25,\ K_i = 0.15,\ \text{and} K_d = 0$. This allows a feedback controlled completion of Phase I with the aid of the mechanical constraints. A sine wave reference velocity is also successfully implemented and tuned by trial and error to $K_p = 0.5,\ K_i = 3,\ \text{and} K_d = 0.001$. Before optimizing gains with compensation design techniques a system model must be obtained that is justified experimentally, and criteria must be defined for a specific application; this entails testing and comparing various parameters with the completion of both phases of the Simulink model from Section 7.1, or performing an experimental FFT on measurements or other model approximation techniques to arrive at a system model.

8.4 Design Beyond First Prototype

Future LAD prototype potentials include a spherical version, a larger version designed for traversing rough terrain, and a millimeter scale version designed for getting into crevices; note that planar versions of the larger and smaller designs may be necessary before the spherical.

Components are purchased for preliminary testing of both the larger and smaller scale versions: For $r = 6$in, Electrocraft Stepper Motor TPP34-793A50-1100-X with Encoder + Driver + Cable + Board, and for the millimeter scale version, New Scale Technologies 3.4mm SQUIGGLE Motor SQL-3.4-TRK-E-15 + Driver + Tracker. Materials are purchased for larger leg lengths up to $L = 24$in, or a larger number of legs, i.e. $L = 12$in, $N = 6$: 6 ft. versions of leg and leg support stock, i.e. lines 8, 10, and 12 from Table 8.2. For the spherical version, and for implementing more advanced unconventional non-linear control techniques: Intersense Inc. Inertia Cube 3 ISC-IC300-A00U + USB Adapter.

Chapter 9

Results

9.1 Justifying and Aiding First Prototype Design

9.1.1 Simulation Results Supporting Kinematics, Geometric Optimization, and Actuator Design

There are results discussed in earlier sections for the purpose of justifying the design concept and theory before detailing construction of the first prototype, and to provide direction for prototype and actuator design. These Sections are 7.2 and 7.3, respectively.

9.1.2 Test Results Supporting Actuator Choice and Sensor Calibrations

Actuator test results and sensor calibrations, including error approximations after filtering, extracted from the test bed in Figure 8.1, are results that aided in the construction of LAD and are discussed in Subsections 8.1.2 and 8.3.2, respectively.

9.2 Theoretical, Virtual, and Experimental

9.2.1 Theoretical and Virtual Results

A theoretical foundation for both kinematics and dynamics has been laid for the design and control of circular robots with diametrically translating legs:

Regarding Phase I constraints, Eqn.(3.1) is the fundamental kinematic constraint equation of Phase I, characterizing the path trajectory of the cores center C, which is predicted by Euclid's Inscribed Angle Theorem outlined in Appendix A. Eqn.(3.5) relates the position of leg 2 to leg 1 and allows the possibility of position control using both actuators. Eqn.(6.7) similarly relates the velocity of the legs.

Regarding Phase II motion, Eqn.(5.14) is the EOM for Phase II and Eqn.(3.12) is its solution. Eqn.(3.7) provides a pseudo-check for the Phase II EOM and consequently the Newtonian Dynamic Model from Chapter 5.

Regarding phase transitions, Eqns.(3.17) and (3.16) provide the velocities during phase transitions, however, the required velocity used for design is from the simulation since it accounts for the mass of the legs.

Regarding optimization, Section 4.2 calculates optimal θ_0 for smooth travel as $71.14°$ by minimizing maximum vertical departure from h_0 and as $68.08°$ by minimizing total vertical departure from h_0.

Regarding forces, Eqns.(5.2), (5.3), and (5.4) derived from a Newtonian perspective, assuming rigid bodies, define the dynamics of Phase I and Eqn.(5.6) defines the dynamics of Phase II.

Regarding rotary motor and pinion/gearbox implementation, Eqns.(8.4), (8.5) and (8.6) calculate design parameters.

Regarding controls, Eqns.(6.14), (6.15), and (6.13) are the reference velocities for the no slip control scheme, and Eqn.(6.12) may permit a control scheme for allowing slip to be implemented.

LAD is represented virtually in a Simulink program described in Section 7.1:

As discussed in Subsection 9.1.1 above, the simulation demonstrates correctness of the kinematics and optimization theory, as well as aiding in speed and force requirements for actuator design. If the speed requirement is not met in the simulation, then, as the theory predicts, it demonstrates the physics of LAD by falling backwards before the apex of Phase II.

The motion trajectory for Phase I with $\theta_0 = 70^\circ$ and $a = 0.1524$m, the prototype parameters, was measured to be $R = 3.23$in, and from Eqn.3.2 R is calculated as $R = 3.46$in.

Regarding optimal tuning for controls, the simulation can function as a plant model if it is validated and adjusted using experimentation.

9.2.2 Experimental Results

The first prototype of LAD is an adjustable design which is essentially a test bed for future controls implementation, and a means of validating theory and simulation before expanding them to N legs, spherical, or miniature cases.

While extensive testing on LAD has not been done yet, the following are some preliminary results that have been extracted:

By demonstrating the completion of the primary motion regime, Phase I, at speeds higher than the required $\dot{r}_1 = 0.17$m/sec, which is deduced from the simulation using measured prototype parameters, the design concept is justified for Phase I. This demonstration includes visualizing the mechanical constraints aiding in the upper level control to create a circular arc of radius R motion trajectory of the cores center C, as predicted by Euclid's Inscribed Angle Theorem, found in Appendix A.

LAD demonstrates stability using a PID compensator for feedback control with both constant and sinusoidal reference velocities.

The motion trajectory for Phase I with $\theta_0 = 85°$ and $a = 0.1540$m, was discerned from a video using imaging software, and was measured to be $R = 3.26$in, and from Eqn.3.2, $R = 3.50$in.

With only 50% of the available current, i.e. about 1.62A, and 30V, LAD successfully completed Phase I for $\theta_0 = 70°$ at about $\dot{r}_1 = 7.5$in/sec, which is higher than the $\dot{r}_1 = 7.1$in/sec which it was designed for. Thus, when only actuating the hind leg, the factor of safety of 2 which was the design goal for the actuator when both legs are controlled, is slightly more than accomplished.

Without freezing the legs or fully initializing, LAD completed both phases, i.e. tumbled, at about 5.0 in/sec for $\theta_0 = 70°$. Using Eqns.(3.17), (6.14), and (3.5), and prototype parameters found in Table B.1, the required tumbling speed for leg 1 is calculated as 5.35 in/sec; note that these equations do not take leg mass into account. The simulation, which considers leg mass, predicts a tumbling speed for leg 1 to be 6.7 in/sec.

Other observations are made, such as, $\theta_0 = 70°$ appears to minimize vertical travel as expected; as θ_0 approaches 90° the required tumbling speed for leg 1 decreases significantly due to LAD's own weight providing acceleration since there is more vertical travel; and lastly, as predicted by the simulation, the friction forces are pointing outwards, i.e. the robot slips inwards due to the core weight.

Chapter 10

Conclusions

This thesis designs a method of locomotion for circular robots with radially protruding legs. The method has an analytical foundation of kinematics and dynamics, lending itself to both optimization and simulation. LAD is designed with three protruding legs, however, the motion regimes are applicable to an N legged circular robot. Motion is generated using an alternating sequence of two elementary maneuvers. The required actuation forces and friction properties are investigated through a dynamic analysis. No slip is assumed for the proposed locomotion, however, slipping is allowed under an alternative control scheme which will be investigated at a future time.

10.1 Geometry of LAD Provides Motion Planning and Allows Optimization

During the motion resulting from LAD's intrinsic geometry, the cores center describes piecewise circular arcs. The inherent flexibility of motion planning allows geometric trajectory optimization. For Phase I the path trajectory is predicted by Euclid's Inscribed Angle Theorem, and the path is analytically optimized through the lens of θ_0 using two different geometric optimization schemes for smooth motion. The resulting values for θ_0 are both about 70° and are discussed in depth at the end of Section 7.2 and the beginning of Section 7.3. It is reasoned that 70° is best for both smooth travel and minimizing energy consumption and power requirements.

The simulation of LAD supports the predicted path trajectory by plotting the motion of the cores center and verifying Phases I and II as circular arcs, which is discussed in Section 7.2. This section also attests to the accuracy of the kinematics, and the geometric optimization is justified in this section.

10.2 Actuator Design Assessment

The actuator design is capable of handling all of the forces and speeds predicted by the simulation in Section 7.3, since it passed all of the tests discussed in Section 8.1.2. A stepper motor is chosen because it works well at high torques and low speeds, has high precision, and performs well in open loop; this choice has been demonstrated to function as expected with the first prototype of LAD.

Actuator performance on the first prototype during Phase I is within about 6% of the design goal for Phase I when controlling both actuators, with the alternate control scheme as discussed in Section 9.2.2. This conclusion assumes that the friction force preventing linear motion of leg 2 is significantly less than 10N, making the alternate control scheme requirements similar to the ideal control scheme of both legs being actuated simultaneously. If the friction force actually is 10N, the design error would be about 20%. However, there is reason to believe that it is much smaller because when moving the foreleg by hand its resistance feels much less than lifting a 10N (about 2 lbs) weight. LAD actuators are designed for a factor of safety of 2 to prevent overheating and allow room for disturbances and error. This indicates that the actuator design concept, including the dynamic theory and simulation, is correct but not without error. Actuator or sensor bandwidth did not pose any issues during the trials with the first prototype.

10.3 Foundational Theory, Simulation, and Test Bed

A theoretical foundation has been laid for the design of circular robots with diametrically translating legs. Specifically regarding Phase I constraints, Phase II motion, phase transitions, path trajectory optimization, forces including friction and actuator, rotary motor and pinion/gearbox implementation, and controls.

The simulation provides justification for the Phase I constraints in Section 7.2, demonstrating how they adhere to the path trajectory predicted by Euclid's Inscribed Angle Theorem, outlined in Appendix A. The path trajectory size, R, as defined by Eqn.3.2, is measured via simulation and experimentation to with less than 7% error in both cases; the error is explained in the simulation and experimentation conclusions below, and is small enough to allow the path trajectory theory resulting from Phase I constraints to hold.

Phase II was derived with two methods, Lagrangian and Newtonian dynamics, providing assurance for its accuracy. Also, it is compared to equations for an inverted pendulum for additional justification.

Phase transition theory was used primarily to create the simulation, but also provides a means of calculating a target core velocity for completion of a full cycle of motion. Despite the good match with LAD's performance in the preliminary testing outlined in Section 9.2.2, this requires further testing with proper initialization of LAD and freezing the legs during Phase II, for validation of accuracy and may require modification such as the inclusion of leg inertia.

Path trajectory optimization is bolstered by simulation results as discussed above, and also through initial observations of LAD appears correct since setting θ_0 to $70°$ allows significantly more energy to be allocated to horizontal motion than $80°$.

Actuation forces and theory for rotary motors with pinions have been used for successful design of the stepper motors as outlined in Section 10.2. Furthermore, the experimental direction of the friction forces matches the simulation, verifying the physical accuracy of the model and dynamic theory behind it. Friction forces do not pose a serious problem in the execution of LAD's motion, however, they cannot be ignored for more precise maneuvers.

Control theory has yet to be successfully implemented, barring the low level PID compensator which has been implemented on stepper motors to produce stable step and sine wave responses with minimal steady state error. Note that this has only been used for control of the hind leg, and the foreleg is controlled by the upper level control provided by the mechanical constraints.

The simulation has been validated by its use for actuator design, and successful prediction of the physics of LAD for both kinematics and dynamics as discussed in Sections 10.2 and 9.2.1. However, the simulation will not suffice for a plant model in controls optimization until extensive testing, validation, and correction is done. This may not be worthwhile until LAD reaches its spherical form or is used for a specific application.

R is measured from the simulation, which was run with the prototype parameters, with a measurement error of 6.6% from the R value of Eqn.3.2, which is representative of the predicted path trajectory from Euclid's Inscribed Angle Theorem. This error is probably due to numerical error and human error while measuring.

To accompany the theoretical design, a noteworthy accomplishment of this thesis is construction of the first prototype of LAD. It has been demonstrated to support the theory and simulation to a fair degree as laid out in the Sections 10.2 and 9.2.2, and is shown to be a test bed useful for advancing controls implementation and conducting research for spherical, miniature, and N legged versions of LAD.

The prototype tumbles, successfully completing both phases of motion at a hind leg speed of about 5.0 in/sec for $\theta_0 = 70°$, and reaches a maximum speed of about 7.5 in/sec with 50% moving current. Setting $\theta_0 = 85°$ and with $a = 0.1540$m at 0.5 in/sec, R is measured during Phase I with a measurement error of 6.9% from the R value of Eqn.3.2, which is representative of the predicted path trajectory from Euclid's Inscribed Angle Theorem.

This error is probably due to error in the angle ϵ in between the legs, and human error while measuring.

10.4 Closing Remarks

A cylindrical core prototype has been constructed with results that support the design concept discussed above; Phase I was executed with the alternate actuation scheme outlined in Figure 7.8. The author hopes to further the control development, generalize LAD to a spherical robot, investigate the expansion to N legs, compare LAD quantitatively with similar mechanisms to justify its use in applications such as Planetary Exploration and Medical Procedures, and investigate miniaturization; future work is currently the most practical outcome of this work and is further explained in Chapter 11 below. The author's next endeavor is to achieve rectilinear motion by designing an initialization routine and programming LAD to efficiently alternate between Phases I and II repeatedly. This thesis theorized a unique mode of locomotion and provided results from both simulation and implementation to support the design; the preliminary testing supports the simulation and theory enough to justify continuing controls implementation and building a spherical LAD.

Chapter 11

Future Work

11.1 Expanding Control Theory and Implementation

The next step in controls implementation is to create a program to initialize LAD with desired initial conditions, then program the completion of both phases of motion with a desired reference velocity for Phase I using Matlab, Simulink, and dSPACE, and finally, program the simultaneous actuation of legs 1 and 2 during Phase I. Sliding Mode control, Adaptive control, or other more unconventional nonlinear control theories, which include a strategy to allow slip, will then be explored to increase the performance and robustness of LAD. Alternatively, it is also worthwhile expanding the Open Loop programming and methodology of LAD since this is a strong point of stepper motors.

There is real potential for the controls of LAD to be augmented beyond the execution of Phases I and II. For instance, during phase transitions, the controls can be programmed, provided acceleration impulses for phase transitions are derived, to add an appropriate dampening effect to reduce the impact acceleration, allowing smoother travel and decreased energy loss. Another opportunity is in creating maneuvers such as pole vaulting over obstacles, or engaging in a pure rolling mode when terrain permits. Finally, specific applications may call for different average horizontal velocities, and to produce this, $v_{C,ref}$ could be calculated by utilizing Eqns.(3.12) and (3.15).

Optimization of the control laws of LAD is beneficial after a spherical version is constructed or a specific application is found. To accomplish this, the simulation of LAD used for the plant model, which includes its underlying theory, must be verified and corrected through extensive testing; an experimental FFT or curve fitting may be done to augment the plant model.

As more prototypes are developed with new motion regimes based on those discussed in this thesis, there may develop a need to introduce more degrees of freedom, and hence more controls, for each leg. For example, the core rotates about the legs in a spherical version, the positions of the feet are controlled, or the legs have the capacity to bend at a desired number of joints. The paper [34] addresses the kinematics introduced by combining multiple links with joints.

11.2 Generalization to Spherical Robot

For the spherical extension of LAD, the author begins at a conceptual level, focusing on a single concept that utilizes the planar motion regimes, but not yet ruling out any other ideas for possible motion regimes.

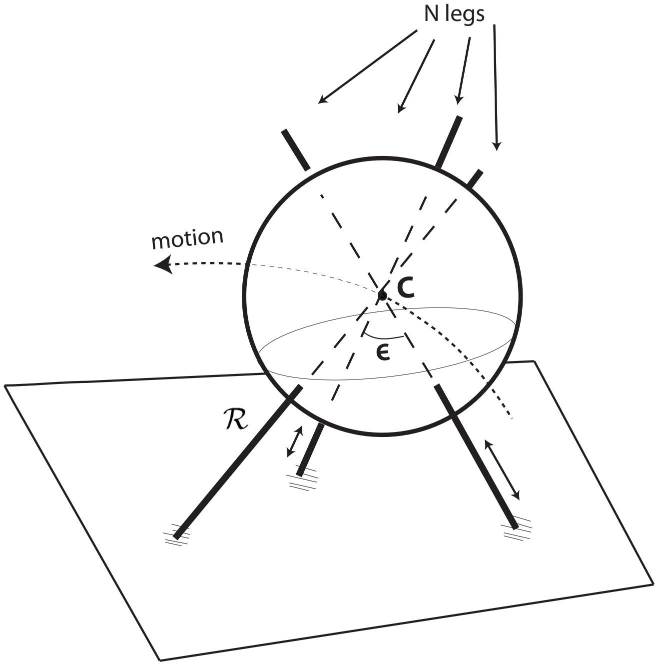

Figure 11.1: Spherical concept - projected motion trajectory of C

where $\mathcal{R}$ is the radius of the motion trajectory, or turning radius, and the motion path represents the path of C projected on a plane parallel with the ground. The driving principle in this concept is the motion of the leg in line with $\mathcal{R}$, a.k.a. the balancing leg. For a straight path this leg will move back and forth in a controlled manner to balance the robot, and for a curved path the balancing leg will rest on the ground making a pivot point as shown in Figure 11.1 above. Another concept at work is that of N legs, and this will ideally be used to its full potential, i.e. to adjust the center of mass as desired, allow abrupt direction changes by switching which legs are the driving legs 1 and 2, and allow obstacles to be climbed and negotiated with ease.

Other ideas for possible motion regimes include, but not limited to: rotating the core about the legs, or using a swirling mass along with conservation of momentum and angular momentum for turning.

11.3 Generalization to N Legs

As N gets larger, the mechanism will resemble an amoeba to a greater degree since the feet bottoms will appear as an outer skin that is morphing. For the planar version, generalizing to N legs changes the primary kinematic constraint Eqn.(3.1) to

$$r + r_1 = \left(\frac{a}{\sin\epsilon}\right)\sin(\pi - \epsilon - \theta) \tag{11.1}$$

where ϵ is the angle between legs, and $\epsilon = \pi/N$ radians. The remaining equations can be rewritten as a function of N in a similar way, but the real challenge of increasing the number of legs is in the implementation.

11.4 Quantitative Comparisons to Justify Applications

Quantitative comparisons of data with other robotic designs for specific applications is necessary to justify the use of LAD. Some comparisons might include speed, weight, size, energy consumption, power requirements, capabilities, etc. Also, quantitative comparisons should be made between different motion regimes and cycles of motion regimes to discern their strengths and weaknesses to choose appropriate regimes for a given application. Some potential applications for LAD include space exploration, and in the far future in vivo medical operations.

11.5 Miniaturization

After the spherical version is realized, miniaturization will unleash a new realm of applications. Before the miniature version is attempted some preliminary work is needed: attaining a thorough understanding of microorganisms, particularly neutrophil, and performing an extensive survey of micro technologies beginning with millimeter scale.

References

[1] T. Das and R. Mukherjee. Exponential stabilization of the rolling sphere. *Automatica*, 40:1877–1889, 2004.

[2] M. R. King, R. Sumagin, C. E. Green, and S. I. Simon. Rolling dynamics of a neutrophil with redistributed l. selectin. *Journal of Mathematical Biosciences*, 194:71–79, 2005.

[3] A. Behar, J. Matthews, F. Carsey, and J. Jones. Nasa/jpl tumbleweed polar rover. *Proceedings of the 2004 IEEE Aerospace Conference, Big Sky, Montana*, 2004.

[4] D. Reynaerts, J. Peirs, and H. V. Brussel. Shape memory microactuation for a gastrointestinal intervention system. *Journal of Sensors and Actuators*, 77:157–166, 1999.

[5] R. H. Armour and J. F. V. Vincent. Rolling in nature and robotics: A review. *Journal of Bionic Engineering*, 3:195–208, 2006.

[6] S. Kimmel. Considerations for and implementations of deliberative and reactive motion planning strategies for the novel actuated rimless spoke wheel robot impass in the two-dimensional sagittal plane. Master's thesis, Virginia Polytechnic Institute and State University, 2008.

[7] A. G. Hlynka and C. G. Hlynka. Multiple leg tumbling robot. *United States Patent No. 7327112 B1*, 2008.

[8] D. K. Pai, R. A. Barman, and S. K. Ralph. Platonic beasts: a new family of multilimbed robots. *Proceedings of the 1994 IEEE International Conference on Robotics and Automation*, 2:1019–1025, 1994.

[9] T. Das and R. Mukherjee. Dynamic analysis of rectilinear motion of a self propelling disk with unbalance masses. *Journal of Applied Mechanics*, 68:58–66, 2001.

[10] T. Mizuno, O. Kagami, T. Sakai, and K. Kawasaki. Locomotion of neutrophil fragments occurs by graded radial extension. *Journal of Cell Motility and the Cytoskeleton*, 35:289–297, 1996.

[11] R. Alon and K. Ley. Cells on the run: shear regulated integrin activation in leukocyte rolling and arrest on endothelial cells. *Journal of Current Opinion in Cell Biology*, 20:1–8, 2008.

[12] Y. BarCohen. Biomimetics: mimicking and inspired by biology. *Proceedings of SPIE, The International Society for Optical Engineering*, 5759:1–9, 2005.

[13] R. S. Fearing. Powering 3 dimensional microrobots: Power density limitations. *Tutorial on Micro Mechatronics and Micro Robotics*, 1998.

[14] K. F. Bohringer, R. S. Fearing, and K. Y. Goldberg. Microassembly. *To appear in The Handbook of Industrial Robotics, Second Edition, Editor Shimon Nof, Wiley and Sons*, 1998.

[15] M. Sitti. Microscale and nanoscale robotics systems. *Journal of IEEE Robotics and Automation Magazine*, 1070:2–9, 2007.

[16] K. Schilling and C. Jungius. Mobile robots for planetary exploration. *Journal of Control Engineering Practice*, 4(4):513–524, 1996.

[17] M. Pavone, P. Arena, and L. Patane. An innovative mechanical and control architecture for a biomimetic hexapod for planetary exploration. *Journal of Space Technology*, 26(1-2):13–24, 2006.

[18] M. E. Rentschler, J. Dumpert, S. R. Platt, K. Lagnemma, D. Oleynikov, and S. M. Farritor. Modeling, analysis, and experimental study of in vivo wheeled robotic mobility. *Journal of IEEE Transactions on Robotics*, 22(2):308–321, 2006.

[19] A. C. Lehman, M. E. Rentschler, S. M. Farritor, and D. Oleynikov. The current state of miniature in vivo laparoscopic robots. *Journal of Robotic Surgery*, 1:45–49, 2007.

[20] Z. Qiang, J. Chuan, M. Xiaohui, and Z. Yutao. Mechanism design and motion analysis of a spherical mobile robot. *Chinese Journal of Mechanical Engineering*, 18(4):542–545, 2005.

[21] J. Ostrowski and J. Burdick. The geometric mechanics of undulatory robotic locomotion. *International Journal of Robotics Research*, 17(7):683–701, 1998.

[22] K. A. McIsaac and J. P. Ostrowski. A geometric approach to gait generation for eel-like locomotion. *Proceedings of the 2000 IEEE/RSJ International Conference on Intelligent Robots and Systems*, 3:2230–2235, 2000.

[23] M. Suzuki, T. Tsuji, and H. Ohtake. A model of motor control of the nematode c. elegans with neuronal circuits. *Journal of Artificial Intelligence in Medicine*, 35:75–86, 2005.

[24] M. Ingram and D. Hong. Whole skin locomotion inspired by amoeboid motility mechanisms. *Proceedings of the ASME International Design Engineering Technical Conferences and Computers and Information in Engineering Conference*, 7B:677–682, 2005.

[25] R. D. Beer, R. D. Quinn, H. J. Chiel, and R. E. Ritzmann. Biologically inspired approaches to robotics. *Communications of the ACM*, 40(3):30–38, 1997.

[26] R. T. Schroer, M. J. Boggess, R. J. Bachmann, R. D. Quinn, and R. E. Ritzmann. Comparing cockroach and whegs robot body motion. *IEEE Conference on Robotics and Automation, New Orleans*, 2004.

[27] K. A. Daltorio, A. D. Horchler, S. Gorb, R. E. Ritzmann, and R. D. Quinn. A small wall-walking robot with compliant, adhesive feet. *IEEE/RSJ International Conference on Intelligent Robots and Systems, Edmonton, Canada*, 2005.

[28] D. Laney and D. Hong. Kinematic analysis of a novel rimless wheel with independently actuated spokes. *Proceedings of the ASME International Design Engineering Technical Conferences and Computer and Information in Engineering Conferences*, pages 609–614, 2005.

[29] D. Laney and D. Hong. Three-dimensional kinematic analysis of the actuated spoke wheel robot. *Proceedings of the ASME 2006 International Design Engineering Technical Conferences and Computers and Information in Engineering Conference*, 2006.

[30] S. K. Agrawal and J. Yan. Rimless wheel with radially expanding spokes: Dynamics, impact, and stable gait. *Proceedings of the 2004 IEEE International Conference on Robotics and Automation*, 4:3240–3244, 2004.

[31] S. K. Agrawal and J. Yan. A three-wheel vehicle with expanding wheels: Differential flatness, trajectory planning, and control. *Proceedings of the 2003 IEEE/RJS International Conference on Intelligent Robots and Systems*, 2:1450–1455, 2003.

[32] R. Potts, Euclid, and R. Simson. Euclid's elements of geometry: the first six books,... *Euclid's Elements*, 3:112–113, 1865.

[33] J. Burdick, B. Goodwine, and R. Mason. Mechanics and control of biomimetic locomotion. *Journal of Robotics Research: Eighth International Symposium*, 1:373–381, 1998.

[34] T. S. Mruthyunjaya. Kinematic structure of mechanisms revisited. *Journal of Mechanism and Machine Theory*, 38:279?320, 2003.

Appendix A

Euclid's Inscribed Angle Theorem

The Inscribed Angle Theorem is Proposition 20 in Book III of Euclid's Elements, [32]: In a circle the angle at the center is double of the angle at the circumference, when the angles have the same circumference as base. This is illustrated in the figure below.

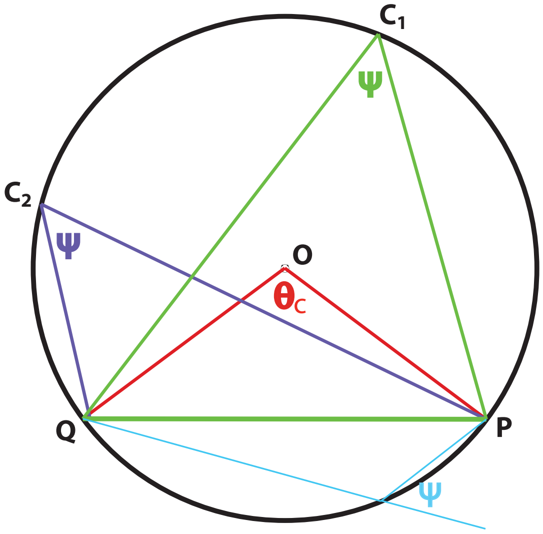

Figure A.1: Euclid's Inscribed Angle Theorem

where θ_C is a central angle and $\theta_C = 2\Psi$. Note the similarities between the above figure and Figure 3.1, which illustrates Phase I. There are several corollaries resulting from Proposition 20, such as the angle Ψ found below the line segment QP, or an inscribed triangle with its base as a circles diameter has a vertex angle of $90°$.

Appendix B

Simulation Details Explained

Parameters for the simulation which extracted results, in Subsection 7.3, used for LAD prototype design, and from the first prototype with estimated errors, are as follows:

Table B.1: Parameters used for simulation and from prototype

Symbol	Description	Value	Prototype Value	Units
$\dot{r}_{1,T}$	Target speed for leg 1 before transition to Ph.2	0.18		m/sec
$\ddot{r}_1$	Acceleration of leg 1	0		m/sec^2
T	Time step	0.001	0.01	sec
Δt_{sim}	Simulation run time	2.0		sec
θ_0	Initial angle leg 1 makes with ground	70	70.0±0.5	deg
β_0	Initial angle leg 2 makes with ground	50	50.0±1.0	deg
$r_{1,0}$	Initial distance between core and leg 1 pivot	0.076	0.0554±0.0005	m
r	Core radius	0.076	0.0794±0.0005	m
L	Leg length in between feet pivots	0.305	0.292±0.005	m
M_d	Mass of disk core	7	6.32±0.10	kg
M_r	Mass of rod legs, each	1	0.31±0.03	kg
h_0	Initial height of core	0.1428		m
$M_{eq,1}$	Equivalent core mass during Ph.1	8		kg
$M_{eq,2}$	Equivalent core mass during Ph.2	9		kg
$I_{eq,1}$	Equivalent core MOI about C during Ph.1	0.0231		kg·m^2
$I_{eq,2}$	Equivalent core MOI about C during Ph.2	0.0260		kg·m^2
$I_{r,P}$	MOI of leg 1 about P and leg 2 about Q	0.0310		kg·m^2
g	gravitational constant, earth	9.81		m/sec^2
F_{m2}	Friction of leg 2 for Alternate Actuation Scheme	10		N

Simulink block diagrams representing the simulation of LAD are found on the next two pages. Equations solved numerically are those found at the end of Section 7.1.

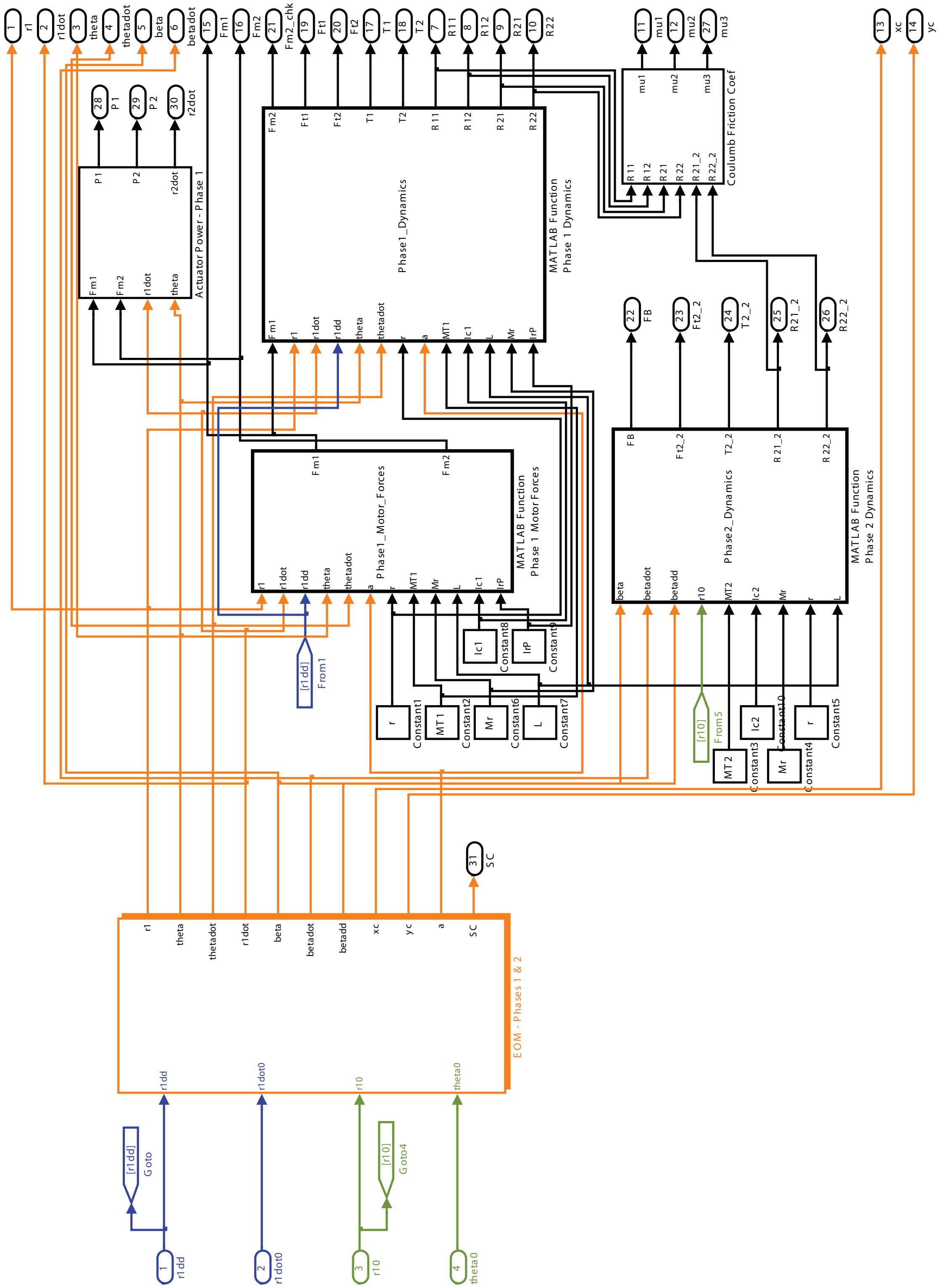

Figure B.1: Simulink block diagram: top level

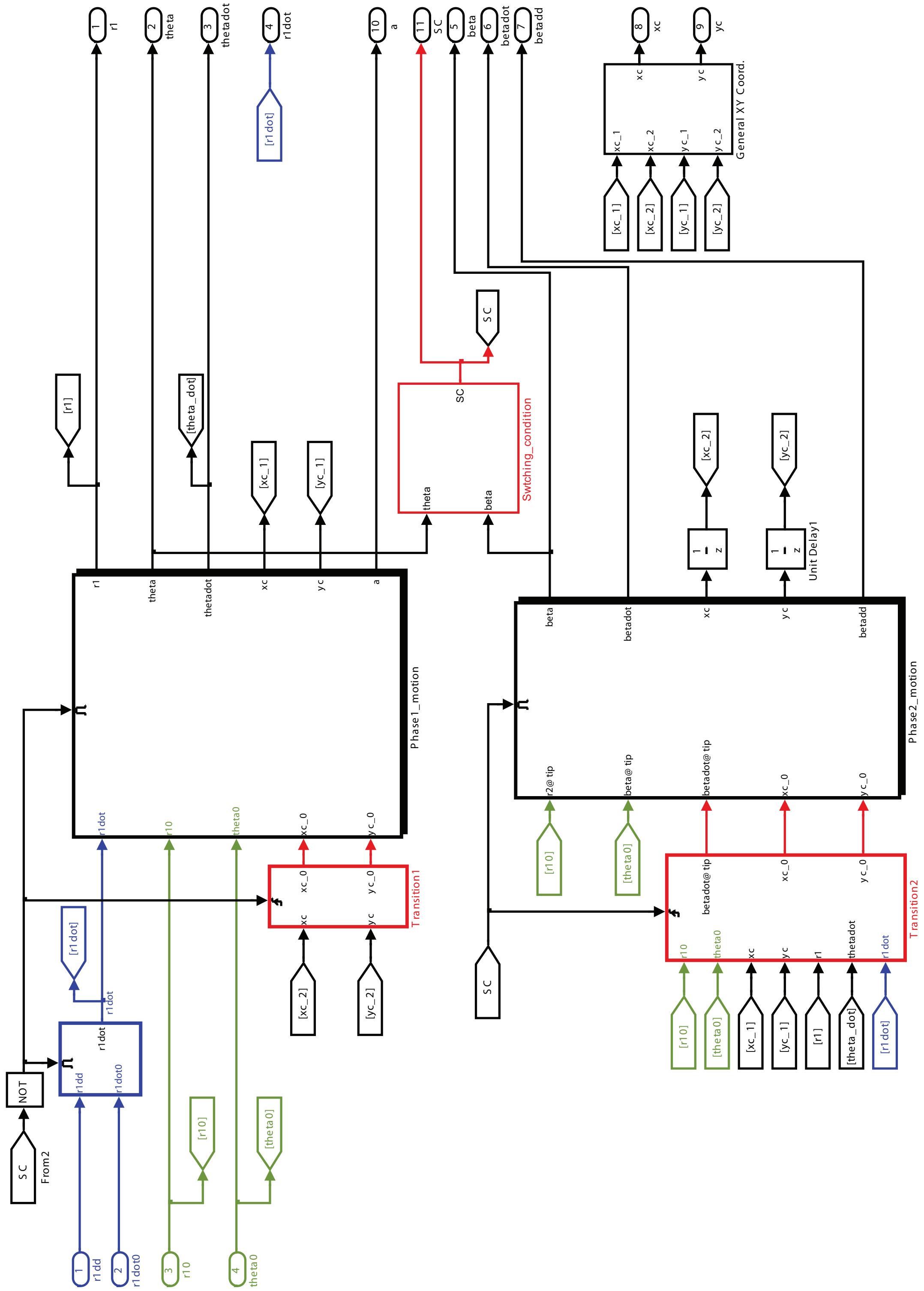

Figure B.2: Simulink block diagram of Phases I and II

Appendix C

Motor Selection Method Matlab Code

Matlab code for motor selection, which is referenced in Subsection 8.1.1, is found below:

```
%%% Motor Selection Method %%%
%
% Eric Steffan
% 3/30/09
%
% Assume robot parameters %
% r1dot0 = 0.18 % [m/sec]
% r1dd = 0; % [m/sec^2]
% theta0 = 70; % [deg]
% r10 = 0.076 % [m]
% r = 0.076 % [m]
% Md = 7 % [kg]
% Mr = 1 % [kg]
% g = 9.81; % [m/sec^2]
% delta_t = 2; % [sec]
format short, close all, clear all, clc

% Motor parameters
```

```
% given
F1 = 50; % [N]
F2 = 25; % [N]
FB = 100; % [N]
v1 = 0.18; % [m/sec]
v2 = 0.34; % [m/sec]

% assume motor and reducer efficiencies, respectively
zeta = 1;
eta = 1;

% calculate Pm, Tm, wm, T, w
% choose F & v
F = F1;
v = v1;

% choose pinion radius
rho = 0.0127; %[m]

% choose speed reducer ratio
N = 1; % [N:1]

% solve motor equations
Preq = F*v/(eta*zeta); % [W]
Tm = F*rho/(eta*N); % [N-m]
wm = v*N/rho; % [rad/sec]
T = eta*N*Tm; % [N-m]
w = wm/N; % [rad/sec]
```

```
% output solutions
X = [Preq Tm wm*60/(2*pi) T w*60/(2*pi)];
disp(’Preq [W]    Tm [N-m]    wm [RPM]         T [N-m]           w [RPM]’)
fprintf(’% .1f % 11.3f % 9.1f % 12.3f % 11.1f\n\n’,X)
disp(’rho [m]       N         zeta [%]      eta [%]’)
fprintf(’% .3f % 6.0f % 11.1f % 10.1f\n’,rho, N, zeta*100, eta*100)
```

Appendix D

dSPACE and Stepper Protocols Explained

Similar to LabView, dSPACE has a programmable, dynamic, interactive GUI capable of both ushering commands and collecting data. The top graph in the figure below illustrates the closed loop velocity response of leg 1, with an arbitrary target speed of 0.15 in/sec during Phase 1. The unexpected rise in speed is caused by an external force disturbance.

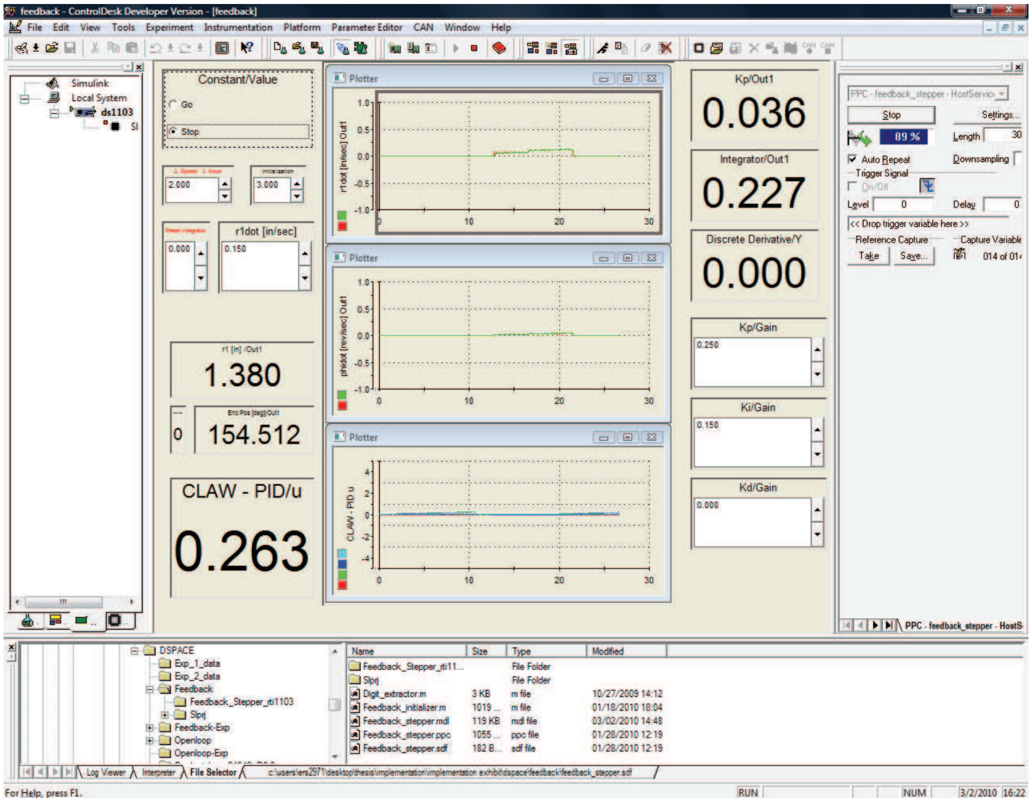

feedback - ControlDesk Developer Version - [feedback]

Constant/Value: ○ Go ● Stop

Initialization: 3.000

r1dot [in/sec]: 0.150

r1 [in] /Out1: 1.380

Enc Pos [deg]/Out1: 154.512

CLAW - PID/u: 0.263

Kp/Out1: 0.036

Integrator/Out1: 0.227

Discrete Derivative/Y: 0.000

Kp/Gain: 0.250

Ki/Gain: 0.150

Kd/Gain: 0.000

PPC - feedback_stepper - HostServic

89 %

Length: 30

☑ Auto Repeat

Trigger Signal: ☐ On/Off

Level: 0

Delay: 0

<< Drop trigger variable here >>

Capture Variable: 014 of 01

Name	Size	Type	Modified
Feedback_Stepper_rti11...		File Folder	
Slprj		File Folder	
Digit_extractor.m	3 KB	m file	10/27/2009 14:12
Feedback_initializer.m	1019 ...	m file	01/18/2010 18:04
Feedback_stepper.mdl	119 KB	mdl file	03/02/2010 14:48
Feedback_stepper.ppc	1055 ...	ppc file	01/28/2010 12:19
Feedback_stepper.sdf	182 B...	sdf file	01/28/2010 12:19

c:\users\ers2971\desktop\thesis\implementation\implementation exhibit\dspace\feedback\feedback_stepper.sdf

For Help, press F1.

Figure D.1: dSPACE ControlDesk

The underpinnings of ControlDesk consist of a Simulink block diagram with additional dSPACE commands. The controls block diagram layout is found in Figure D.1 below.

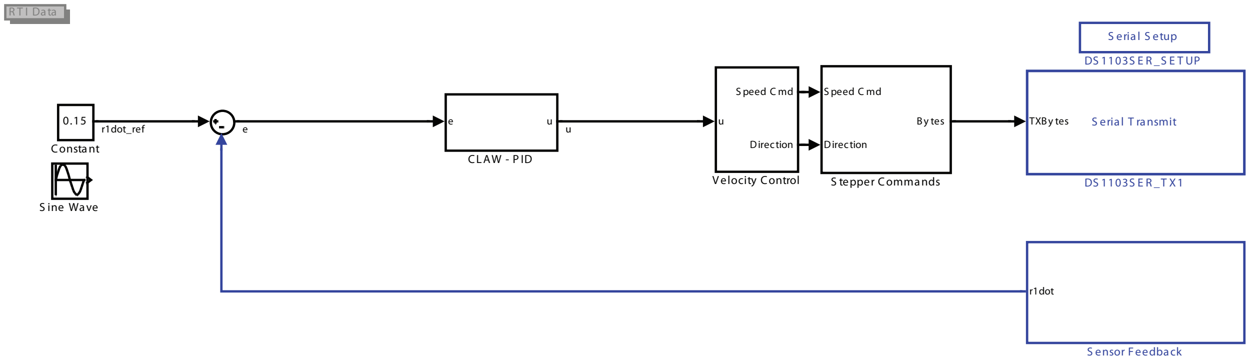

Figure D.2: dSPACE controls implementation

within the Stepper Commands block is the following:

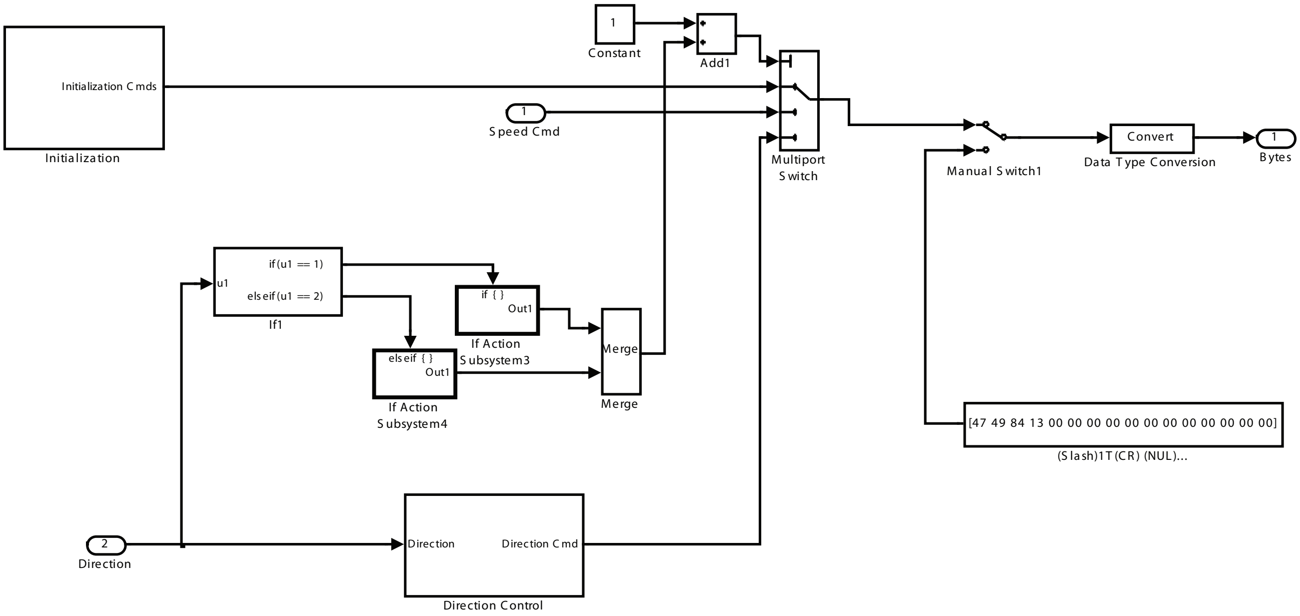

Figure D.3: dSPACE commands

and within the Direction Control block is the following on the next page.

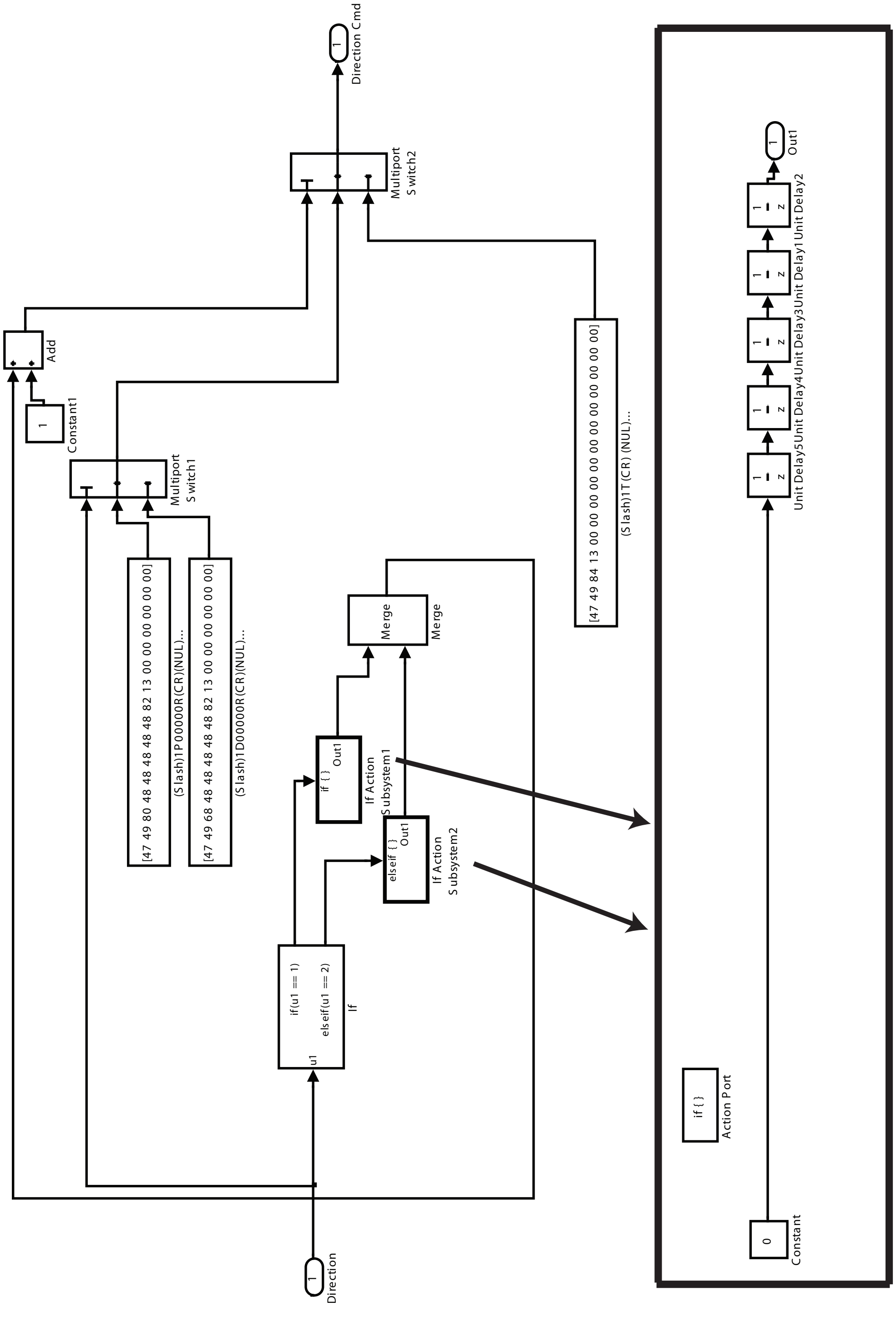

Figure D.4: dSPACE direction command block diagram

The context of Figure D.4 and its origins are found in Subsection 8.3.3; it is essentially an algorithm for robust, autonomous direction change of a stepper motor. The five discrete delay blocks within the bold bordered box are strategically placed for robustness, and this strategy is discussed briefly in Subsection 8.3.3. Another part of the direction control algorithm is found in Figure D.3; note that there are ten discrete delay blocks in each of the two If Action blocks.

Open loop commands, which are programmed in the block diagrams as bytes in Decimal, and are essential to operating stepper motors are explained in the following table:

Table D.1: Open loop stepper commands in DT Protocol

Essential Stepper Commands (16 byte form, with 2 whole num. or 1 char. per byte)		
Decimal	DT Protocol	Command
47 49 80 48 48 48 48 48 82 13 00 00 00 00 00 00	\1D00000R(CR)(NULL)...	Constant velocity counter clockwise, motor 1
47 49 68 48 48 48 48 48 82 13 00 00 00 00 00 00	\1P00000R(CR)(NULL)...	Constant velocity clockwise, motor 1
47 49 84 13 00 00 00 00 00 00 00 00 00 00 00 00	\1T(CR)(NULL)...	Stop (instantaneously), motor 1
47 49 86 XX XX XX XX XX XX 82 13 00 00 00 00 00	\1VXXXXXX(CR)(NULL)...	Sets speed to XXXXXX microsteps/sec

where X is any whole number. Note that many other commands not listed here, command sequences, and ways to execute the commands within Simulink are also important to the operation of steppers, some of which are used in the block diagrams above. The commands are found in the documentation from AllMotion for line 2 of Table 8.1.

Calibration constants are used to adjust data from the sensors into the appropriate units. Methods for finding them are in Subsection 8.3.2, and they are listed in the table below:

Table D.2: Sensor/driver calibration constants

Sensor/Driver	Constant	Converts To
Potentiometer (BOM #32)	$6.21 \ \frac{\text{in}}{\text{V} \times 10^1}$	in
Potentiometer + Discrete Derivative	$1/\pi$ rev/in	rev/sec
Encoder (BOM #3)	-360/1250 deg/tick	deg
Enc (delta position)	$-100/1250 \ \frac{\text{rev}}{\text{tick} \times 10^2}$	rev/sec
Enc (delta position)	π in/rev	in/sec
Stepper Driver (ref velocity) (BOM #2)	$51200/\pi$ microsteps/in	microsteps/sec

The following Matlab code, referenced in Subsection 8.3.3 and placed within the Velocity Control block of Figure D.2, is for parsing velocity data from the potentiometers into the DT Protocol:

```
%%% Extracts Digit Place Holders as Portescap Stepper Code %%%
%
% Eric Steffan
% 10/27/09
%
% INPUTS: Num
% PLACE HOLDER OUTPUTS: a,b,c,d,e,f,g,h,i,j,sign
%                               (( +/- 1 2 3,4 5 6.7 8 9 0 ))
% OUTPUTS: a1,b1,c1,d1,e1,f1,(g1,h1,i1,j1<-- optional),sign
%
% Num is a real number
% 'a,b,c,...' are digit place holders from largest to smallest.
% a: digit in the hundred thousands place
% j: digit in the ten thousandths place
% 'sign' is 1 for a positive, -1 for a negative, and 0 for zero.
%
% WARNING: if Num contains digit place holders >= 10^6 or <10^-4
%                 then information will be DELETED.
%
%
function [a1,b1,c1,d1,e1,f1,sign] = DIGIT_EXTRACTOR(Num)

% determine the sign of the Num
if Num == 0
```

```
    sign = 0;
elseif Num >0
    sign = 1;
else sign = 2;
    Num = abs(Num);
end

% add 10^-10 to prevent ’floor’ rounding errors
Num = Num + 10^-10;

% initialize digit place holders
a=1;b=1;c=1;d=1;e=1;f=1;g=1;h=1;i=1;j=1;

% zero out not needed place holders
if Num <10^-4
    a=0;b=0;c=0;d=0;e=0;f=0;g=0;h=0;i=0;j=0;
elseif Num <10^-3
    a=0;b=0;c=0;d=0;e=0;f=0;g=0;h=0;i=0;
elseif Num <10^-2
    a=0;b=0;c=0;d=0;e=0;f=0;g=0;h=0;
elseif Num <10^-1
    a=0;b=0;c=0;d=0;e=0;f=0;g=0;
elseif Num <10^0
    a=0;b=0;c=0;d=0;e=0;f=0;
elseif Num <10^1
    a=0;b=0;c=0;d=0;e=0;
elseif Num <10^2
    a=0;b=0;c=0;d=0;
```

```
elseif Num <10^3
    a=0;b=0;c=0;
elseif Num <10^4
    a=0;b=0;
elseif Num <10^5
    a=0;
end

% determine magnitudes of useful place holders
if a >0
    Num = Num * 10^-5;
    a = floor(Num);
    X = [a;b;c;d;e;f;g;h;i;j];
    for n = 1:8
        Num = (Num - X(n)) * 10;
        X(n+1) = floor(Num);
    end
elseif b >0
    Num = Num * 10^-4;
    b = floor(Num);
    X = [a;b;c;d;e;f;g;h;i;j];
    for n = 2:8
        Num = (Num - X(n)) * 10;
        X(n+1) = floor(Num);
    end
elseif c >0
    Num = Num * 10^-3;
    c = floor(Num);
```

```
    X = [a;b;c;d;e;f;g;h;i;j];
    for n = 3:8
        Num = (Num - X(n)) * 10;
        X(n+1) = floor(Num);
    end
elseif d >0
    Num = Num * 10^-2;
    d = floor(Num);
    X = [a;b;c;d;e;f;g;h;i;j];
    for n = 4:8
        Num = (Num - X(n)) * 10;
        X(n+1) = floor(Num);
    end
elseif e >0
    Num = Num * 10^-1;
    d = floor(Num);
    X = [a;b;c;d;e;f;g;h;i;j];
    for n = 5:8
        Num = (Num - X(n)) * 10;
        X(n+1) = floor(Num);
    end
elseif f >0
    f = floor(Num);
    X = [a;b;c;d;e;f;g;h;i;j];
    for n = 6:8
        Num = (Num - X(n)) * 10;
        X(n+1) = floor(Num);
    end
```

```
elseif g >0
    Num = Num * 10^1;
    g = floor(Num);
    X = [a;b;c;d;e;f;g;h;i;j];
    for n = 7:8
        Num = (Num - X(n)) * 10;
        X(n+1) = floor(Num);
    end
elseif h >0
    Num = Num * 10^2;
    h = floor(Num);
    X = [a;b;c;d;e;f;g;h;i;j];
    Num = (Num - X(8)) * 10;
    X(9) = floor(Num);
elseif i >0
    Num = Num * 10^3;
    i = floor(Num);
    X = [a;b;c;d;e;f;g;h;i;j];
else Num = Num * 10^3;
    X = [a;b;c;d;e;f;g;h;i;j];
    end
Num = (Num - X(9)) * 10;
j = floor(Num);
b=X(2);c=X(3);d=X(4);e=X(5);f=X(6);g=X(7);h=X(8);i=X(9);
a1=a+48;b1=b+48;c1=c+48;d1=d+48;e1=e+48;f1=f+48;g1=g+48;h1=h+48;i1=i+48;j1=j+48;
```

Appendix E

Summary of Technology Search

When searching for different technologies, specifically motors and potentiometers, a streamlined approach is used. It consists of first researching the available technologies from an informational standpoint; links to various informational web sites exist at the top of the spreadsheet Figure E.1 on the next page. Then finding the industrial leaders with the aid of tools such as the GlobalSpec search engine, and learning their technology, which is preferably similar to that which was researched, and labeling them as plausible, considering, or not plausible in the second to last column with a note as to why in the last column. By taking this approach few opportunities are missed as the author gradually narrows down the possible vendor selection by comparing products from their web sites and having in depth conversations with technical support from each company. When communicating with vendors information is readily accessible via the links at the bottom of the spreadsheet; for instance, to communicate and visualize the design concept the author refers to Figure 8.2. Supplementary programs such as the code created in Appendix C specifically for selecting motors are used when necessary to improve efficiency. Once an item is purchased the company is highlighted in yellow and since the technical support is known by name, any problems that arise are handled with the wisdom of several individuals.

The author illustrates his approach to utilizing a \$10,000 budget to demonstrate an effective, efficient method for surveying technology, and purchasing. This approach can assuage the construction of future prototypes.

Companies

#	Company	Website	Contact/Tech Supp.	Phone	Email	Product line...	Assessment	Notes
			Company Search Engines, Large Distributors, & Informational					
1	Thomasnet	http://www.thomasnet.com/				International Search Engine	n/a	
2	Global Spec	http://www.globalspec.com/				Product Info., Companies	n/a	
3	eFunda	http://www.efunda.com/home.cfm				Engr. Fund. Info., Companies	n/a	
4	Steven Engineering	http://stevenengineering.com/index.html				Choice Companies	n/a	
5	Industrial Press	http://new.industrialpress.com/				Publishers of handbooks	n/a	Machinery's Handbook, 28th Ed.
6	Grainger	http://www.grainger.com				Ind. Supply, Ind. Electronics	Plausible	ROCHESTER
7	Small Parts $	http://www.smallparts.com/				Lab Supply	Plausible	
8	McMaster Carr $ ***	http://www.mcmaster.com/		530-600-3600	chi.sales@mcmaster.com	Ind. Supply, Rack and Pinion	Plausible	Pinion - 6325K88, 4ft Rack - 6295K232
9	MSC Industrial Supply Co. $	http://www1.mscdirect.com/cgi/nnsrhm				Ind. Supply	Plausible	
10	Cole Parmer $	http://www.coleparmer.com/index.asp				Lab Supply, Ind. Supply	Plausible	
			1. Rotary Motors, Linear Motors, Controllers, Drive Trains, Micro Motors...					
1	Faulhaber %	http://www.faulhaber-group.com/				Microsystems	Not plausible	Germany
2	SDP/SI %	http://www.sdp-si.com/index.asp				Drive trains, Gearhead motors	Considering	
3	Baldor %	http://www.baldor.com				Linear, Rotary, Servo motors	Not plausible	ROCHESTER, high power, low speed
4	Electrocraft %	http://www.electrocraft.com/	Tom Ouellette	919-847-3057	touellette@electrocraft.com	Linear, Rotary, Stepper motors	Not plausible	TPP17-58430-1 (N+1C), [illegible]
5	Parker %	http://www.parker.com				Stepper motors	Not plausible	AKM Motors, Size Nema23 and up
6	Danahermotion %	http://www.danahermotion.com				Linear, Rotary, Servo, Steppers	Not plausible	CTP13ELF17 (N+1C)
7	Festo %	http://www.festo.com/cms/en-us_us/2538.htm		1-800-55-33786		Linear, Rotary motors, Pneumatics	Not plausible	Steppers/Servos, Large
8	Humphrey %	http://www.humphrey-products.com/				Pneumatics, fluids, micro systems	Not plausible	
9	Kerk Motion %	http://www.kerkmotion.com/				Leadscrew actuators	Not plausible	Rack and pinion more suitable
10	NSK Precision %	http://www.nskprecision.com/				Linear motion systems	Not plausible	Linear motors too expensive
11	Linear Motion %	http://www.linearmotion.skf.com/				Linear motion systems	Not plausible	Linear motors too expensive
12	Globe Motors %	http://www.globe-motors.com/home.html		937-228-3171	sales@globe-motors.com	Rotary motors	Not plausible	
13	Nook Ind. %	http://www.nookindustries.com/	John Touls	216-271-7900	jtoula@nookind.com	Belt-guides, Linear bearings	Plausible	See VT thesis ELSZ/QLSZ, XEP-06
14	Bishop Wisecarver %	http://www.bwc.com/	Ken Ferguson	503-697-5040		Guide-rails	Considering	
15	Rockwell Automation %	http://www.rockwellautomation.com/	Maureen Holley	585-475-1600		High-performance servos	Not plausible	Exceeds needs/expensive
16	QCI %	http://www.qcontrol.com/				Rotary servos	Not plausible	
17	RC Controls $	http://www.rcontrols.com				QCI	Not plausible	
18	Firgelli %	http://www.firgelliauto.com				Linear motion systems	Not plausible	Linear motors too expensive
19	Tusk %	http://www.tuskdirect.com/		800-447-2042		Linear bearings, miniature	Considering	
20	Danaher %	http://www.danahermotion.com/website/com/eng/index.php				Servos, Linear systems	Considering	Precision-made
21	Kaman $	http://www.kamandirect.com/				Baldor, Danaher	Not plausible	
22	Rollon %	http://www.rolloncorp.com/index.html		877-976-5565		Linear bearings	Considering	
23	Portescap % ***	http://www.portescap.com/	Dave Beckstoffer	540-731-5605		Stepper motors, DC motors	Plausible	22N11BD208-0, Dave B.: 540-330-5900 (cell)
24	Avnet $	http://www.avnet.com/		1-800-541-4105	express.west@avnet.com	Portescap	Plausible	
25	Allmotion %	http://www.allmotion.com/	Arch	408-450-1345		Controllers/Drivers	Plausible	
26	New Scale Technologies %	http://www.newscaletech.com	Joe Guarino	585-924-4450x123		Micro/SQUIGGLE Motors	Plausible	
				2. Sensors, Encoders...				
1	Physik Instrumente %	http://www.pi-usa.us/				Piezo, Nano, Positioning	Considering	
2	Micro Epsilon % ***	http://www.micro-epsilon.com/		919-787-9707		Micro Sensors, Pots	Plausible	Cable wire sensors, internationally recognized
3	Novotechnik %	http://www.novotechnik.com/	Mike McClish	734-591-7475	mcclish@novotechnik.com	Pots, LVDT, Linear guide sensors	Considering	Mike took interest in our design.
4	Analog Devices %	http://www.analog.com/en/index.html				Inertia Cube	Not plausible	
5	ASM %	http://www.asm-sensor.com/asm/homepage.php?lang=en				Pots, Angle sensors	Considering	
6	Dynapar %	http://www.dynapar.com/				Encoders	Not plausible	
7	Takex %	http://www.takex.com/america.php				Automation Optical sensors	Not plausible	
8	Turck %	http://www.turck-usa.com/				Automation	Not plausible	
9	Banner %	http://www.bannerengineering.com/en-US/				Optical sensors	Not plausible	
10	Everight Position %	http://www.everightsensors.com/index.shtml				Pots, Cable wire pots	Not plausible	Posital FRABA has cable pull pot
11	Unimeasure %	http://unimeasure.com/				Cable wire pots	Not plausible	Poor precision
12	US Digital %	http://usdigital.com/	Tanya Ivanov	360-260-2468	Tanya.I@usdigital.com	Optical encoders	Plausible	ES-1250 encoder
13	InterSense	http://www.intersense.com/	Brian Celus	585-352-5491	brian_celus@intersense.com	Precision motion tracking	Plausible	InertiaCube3
14	IMI Sensors	http://www.imi-sensors.com/				Sensors, Instruments	Considering	BUFFALO
15	MTI Instruments %	http://www.mtiinstruments.com/				Precision Non-contact sensors	Not plausible	Optical sensor $1200
				3. Electronics, Controls...				
1	Digikey $ ***	http://www.digikey.com/		1-800-344-4539		CUI, Connectors, Batteries	Plausible	Connector for ES-1250 encoder
2	dSPACE	http://www.dspace.com/ww/en/inc/home.cfm?nv=n1		1-248-295-4700		dSPACE hardware & software	Plausible	
3	Mouser Electronics $	http://www.mouser.com/					Considering	
4	Freescale Semiconductors %	http://www.freescale.com/				Microcontrollers	Not plausible	
5	Goldcrest Electronics $	http://www.goldcrestelectronics.com/		585-545-8454		Wire, Connectors, Tools, Sensors	Plausible	LOCAL: 700S Goodman St., Rochester, NY 14620
6	CUI Inc. %	http://www.cui.com/	Trevor	1-800-275-4899		Cables, Sensors	Plausible	
7	Omron %	http://www.omron247.com/				Automation, Sensors	Not plausible	
8	KOM Automation $	http://www.komautomation.com/index.cfm				Banner, Turck, Ind. Controls	Not plausible	
9	Velleman, Inc. $	http://www.vellemanusa.com/				Batteries, Connectors	Considering	
				4. Other				
1	M&P Flange & Pipe Protection %	http://www.m-p.com/	Jason Falco	713-453-6339	jason@m-p.com	Pipe products	Not plausible	TX, End caps for 6 1/4" OD, $50 minimum
2	Alliance Plastics %	http://www.allianceplastics.com/	May	814-899-7671		Plastics	Plausible	PA, free samples, P/N #1274A
3	Pittsford Lumber & Woodshop % ***	http://www.pittsfordlumber.com/Pittsford_Lumber/home.html	Steve	585-385-1877		Custom wood stock, etc.	Plausible	ROCHESTER, pickup
4	SMC %	http://www.smcusa.com/				Pneumatics	Not plausible	
5	Johnson Controls Inc.	http://www.johnsoncontrols.com/publish/us/en.html				Infrastructure projects, Auto, Energy	Not plausible	Engg. Projects, R&D
Legend		Design Information Links						
%	Manufacturer	fin robot concept						
$	Distributor	fin motor robot specs						
***	Choice company	fin motor dim						
		stepper motor basics						
		robot design drawing - 2009-05-04						

Figure E.1: Streamlined technology search and companies list